UNIVERSITY OF CALIFORNIA,
IRVINE

Nanoscale changes for macroscale results: modulation of cancer metabolism and adhesion by the substrate

DISSERTATION

submitted in partial satisfaction of the requirements
for the degree of

DOCTOR OF PHILOSOPHY

in Chemical Engineering

by

Emma Jane Mah

Dissertation Committee:
Assistant Professor Michelle Digman, Chair
Professor Albert Yee
Associate Professor Melissa Lodoen

2018

DEDICATION

To

God, my parents, family, and friends.

With their encouragement and support, I was able to believe in myself and my ability to do or become anything I want.

I also would like to give a special thanks to my newly-wed husband, Eric Fong, for giving me the courage to overcome all the hurdles that came with graduate school. You were always there to listen to my struggles and became my #1 cheerleader throughout this journey.

Special dedication to my father who is no longer with us and fought lung cancer during his last days on earth. Because of his passing, I came to realize how cancer is so prevalent and that many of us know of someone or is personally fighting this illness. Soon after, I came to the decision I can contribute to this battle by dedicating my efforts and mind to learn as much as possible about cancer in hopes of playing a part in its cure.

[38] For I am convinced that neither death nor life, neither angels nor demons, neither the present nor the future, nor any powers, [39] neither height nor depth, nor anything else in all creation, will be able to separate us from the love of God that is in Christ Jesus our Lord.
(Romans 8:38-39, NIV)

TABLE OF CONTENTS

Page

LIST OF FIGURES

Page

LIST OF TABLES

Page

ACKNOWLEDGMENTS

I want to sincerely thank Professor Albert Yee for taking mentoring me since the beginning of my journey as a graduate student. With his help, I was challenged to think critically through all my scientific discoveries and built me to be the researcher I currently am. I learned how to ask important questions and bring significance to the work that I do. Most importantly, I've learned how to be a mentor myself and motivate my students to always dig deeper for the answers they seek.

I must thank Professor Michelle Digman for also taking me under her wing and opened my eyes to the new world of fluorescent microscopy. From the point of joining her lab, I was given so many opportunities and resources to thrive in my research. As someone that had no background experience with fluorescence, it amazes me how much I have learned with her mentorship. Together with Professor Yee, we were able to build a collaborative relationship that interdisciplinary and highlights the fields of engineering, biology, and materials. The experience has provided me with a diverse background that is rare to have.

Of course, I have to thank my lab members in the AFYee lab, Digman lab, and the Laboratory for Fluorescence Dynamics, past and present for their advice and scientific discussions throughout time graduate students. Special thanks to Dr. Enrico Gratton for his help with imaging analysis and providing his expertise in fluorescence microscopy. Thanks also to Dr. Elena Liang, Gabrielle McGahey, and Jeremy Jacinto who have made important scientific contributions to the work presented in this thesis.

Lastly, I would like to thank my other committee members: Dr. Melissa Lodoen and Dr. Vasan Venugopalan for their guidance through my Ph.D. work and their scientific input.

This work was funded in part by the NSF BEST IGERT traineeship and the American Cancer Society.

CURRICULUM VITAE

Emma Jane Mah

EDUCATION

Bachelor of Science in Chemical Engineering **2012**
University of California, San Diego *San Diego, CA*

Master of Science in Chemical and Biochemical Engineering **2016**
University of California, Irvine *Irvine, CA*

Doctor of Philosophy in Chemical and Biochemical Engineering **2018**
University of California, Irvine *Irvine, CA*

RESEARCH EXPERIENCE

Research Volunteer **2011**
University of California, San Diego *San Diego, CA*

Frontier Lab Student Researcher **2011-2012**
Osaka University *Osaka Japan*

FIELD OF STUDY
Cancer cell invasion and metabolism

PUBLICATIONS

1. Liu X, Wong SS, Taype C, Kim J, Shentu T, Espinoza C, Finley C, Bradley JE, Head BP, Patel HH, **Mah EJ**, Hagood JS. Thy-1 interaction with Fas in lipid rafts regulates fibroblast apoptosis and lung injury resolution. *Lab Invest* 97: 256-267 (2017).
2. Sakai S, Liu Y, **Mah, EJ**, Taya M. Horseradish peroxidase/catalase-mediated cell-laden alginate-based hydrogel tube production in two-phase coaxial flow of

aqueous solutions for filament-like tissues fabrication. *Biofabrication* 5 (2013) 015012.

3. **Mah EJ,** Liang EI, Yee AF, Digman MA. Focal Adhesion Formation and Reorganization on Nanopatterned Surfaces. *Biophys*. (2016). J 110:p133A.
4. Liang EI, **Mah EJ**, Yee AF, Digman MA. Correlation of Focal Adhesion Assembly and Disassembly with Cell Migration on Nanotopography. *Integrative Biology* 9 (2017): 145-155.
5. **Mah EJ,** Yee AF, Digman MA. Metabolism modulation of cancer cell on varying substrate stiffnesses. *Biophys*. (2018). J 114: p19a.
6. **Mah EJ**, Yee AF, Digman MA. Collagen stiffness modulates MDA-MB231 cell metabolism through adhesion-mediated contractility. Submitted (2018). bioRxiv 272948; doi: https://doi.org/10.1101/272948

CONFERENCE PRESENTATIONS

1. "Super-resolution Imaging Analysis of Focal Adhesions at the Nanoscale". University of California Systemwide Biomedical Engineering Symposium UC Irvine, Irvine, CA, 2014.
2. "Super-resolution Imaging Analysis of Focal Adhesions at the Nanoscale". Southern California Society for Microscopy and Microanalysis, Pasadena, CA, 2015.
3. "Aggregation States of Focal Adhesions on Nanotopography". American Society for Cell Biology, San Diego, CA, 2015.
4. "Focal Adhesion Formation and Reorganization on Nanopatterned Surfaces". Biomedical Engineering Society Meeting, Tampa, FL, 2015.
5. "Focal Adhesion Formation and Reorganization on Nanopatterned Surfaces". Gordon Research Conference: Cell adhesion and signaling, Andover, NH, 2015.
6. "Super-resolution Imaging Analysis of Focal Adhesions at the Nanoscale". Southern California Systems Biology Conference, Irvine, CA, 2015.
7. "Focal Adhesion Formation and Reorganization on Nanopatterned Surfaces". Gordon Research Conference: Signaling by Adhesion Receptors, 2016.
8. "Focal Adhesion Formation and Reorganization on Nanopatterned Surfaces". Biophysical Society Meeting, Los Angeles, CA, 2016.
9. "Mitochondria Recruitment and Metabolism Modulation on Varying Substrate Stiffness". University of California Systemwide Biomedical Engineering Symposium UCLA, Los Angeles, CA, 2017.
10. "Metabolism modulation of cancer cells on varying substrate stiffness". Biophysical Society Meeting, San Francisco, CA, 2018.

ABSTRACT OF THE DISSERTATION

Nanoscale changes for macroscale results: modulation of cancer metabolism and adhesion by the substrate

By

Emma Jane Mah

Doctor of Philosophy in Chemical Engineering

University of California, Irvine, 2018

Professor Michelle Digman, Chair

Cell-to-substrate interactions are known to regulate important cellular processes such as migration, proliferation, and intercellular signaling. Cancer cells remodel the surrounding collagen matrix and promote collagen fibrillogenesis for invasion. This increases substrate density and activates the mechanosensing pathway for events such as adhesion and migration. Recent studies indicate that metabolism is able to affect cancer invasion and that mitochondria are recruited towards the invading edges of the cell. There seems to be a link between the mechanosensing and metabolism pathway in promoting invasion; however, it is unclear how these are regulated and affects

mitochondria trafficking towards the protruding edges. In this thesis, focal adhesion (FA) dynamics within NIH3T3 cells were studied using the Number and Molecular Brightness analysis and were found to adapt to the underlying nanotopography by modulating their adhesion size and turnover dynamics leading to a change in cell speed. This laid the foundational studies within cancer cells. In MDA-MB231 breast cancer cells, raster imaging correlation spectroscopy (RICS) was used to study focal adhesion dynamics in response to substrate topography and collagen density. The increase of substrate density and addition of nanolines showed a decrease in FA protein dynamics and increased tension, respectively. In addition, Fluorescent lifetime imaging microscopy (FLIM) was used to measure metabolic signatures within MDA-MB231 cells. A shift from oxidative phosphorylation (OXPHOS) to glycolysis (GLY) with increasing collagen density was observed. Since the increase of substrate density is known to upregulate focal adhesion formation, actin polymerization, migration, and invasion, a large amount of ATP is consumed. Rac1 activation was stimulated to promote membrane formation and actin polymerization to observe mitochondria recruitment. Mitochondria transport speed increased when Rac1 was activated compared to when it was inactivated, specifically in breast tumor cells. This shows that mitochondria are transported to regions of high energy consumption and sustain processes needed for invasion. In addition, metabolism of the invading protrusions was

found to shift towards a GLY metabolic signature. Results indicate that collagen density, metabolism and mitochondria trafficking all play an important role in regulating cancer cell invasion. When developing therapies, these parameters should be considered in order to effectively prevent metastasis.

Chapter 1

1. INTRODUCTION

Cells are able to adapt and change their behavior based on the properties of their surrounding microenvironment. Factors such as matrix composition, mechanical properties, and even topography can change the phenotype of the cell.[1–6] Researchers have taken advantage of these behaviors to develop platforms to promote cell adhesion and migration for biomedical implants or recreate biological systems for tissue engineering. In the same way, these biological platforms are used to study the how the microenvironment can cause whole cell changes in diseases and isolate parameters to create therapies. Within this thesis, I will present work that studies cell adhesion and migration through the manipulation of their microenvironment. I will then focus on how the surrounding extracellular matrix (ECM) can affect cancer cell behavior, more specifically, their metabolism and invasion.

Cancer is the second leading cause of death in the United States and is expected to be ranked number 1 in the next few years.[7] Most cancers have four stages of development with the final stage being metastasis, or the migration of cancer cells from

their primary site to a secondary site. Research has been dedicated to delay or prevent metastasis from occurring. These efforts of ongoing research and clinical studies have decreased the risk of dying from cancer by 22% between the years 1991 and 2011.[7] With continual research and application of current cancer knowledge, a further reduction in the percentage of deaths is possible. In order to develop therapies to decrease metastasis, we must first understand the different factors at play that affect cell migration.

1.1. Substrate-to-cell interactions

1.1.1. Integrin adhesion to the matrix

The cell forms contact points—focal adhesions (FAs)—that are composed of hundreds of different proteins and allow direct communication with the ECM.[8,9] The substrate must have certain properties to allow favorable adhesion attachment, such as chemical properties and topography.[10,11] Transmembrane proteins called integrins bind to regions on the ECM of specific binding sites. There are 18 α- and 8 β- integrin subunits identified within vertebrates which combine into 24 different heterodimers that recognize ECM binding sites (**Table 1.1**).[12] For example, fibronectin contains residues of arginine, glycine, and aspartate, also known as RGD, which certain integrin subunits bind that may not bind to collagen. On the other hand, the hexapeptide

GFOGER has been identified as the binding domain within triple helix collagen structures for α2β1 integrin.[13] This binding causes a conformational change of the integrin and further allows other adhesion adaptor proteins such as talin, paxillin, and vinculin

Table 1.1: Overview of integrin heterodimers and their ECM binding

		Integrin subunit	
		α	**β**
ECM	**Laminin**	3, 7	1
		6	1, 4
	Collagen	1, 2, 9, 10, 11	1
	RGD	5, 8	1
		V	1, 3, 5, 6, 8
		IIb	3

to bind to each other and tether to the actin cytoskeleton. This forms the mechanosensing network within the cell and is essential to stabilize the adhesion complex and allow for its maturation.[14] With FA growth, the actin filament further polymerizes and forms a branched network (**Figure 1.1**). Increased substrate stiffness has been positively correlated with FA size and actin branching due to increased traction when the cell pulls on the substrate.[15–18] On the other hand, smaller FAs are formed on softer substrates and inhibit cell spreading, which is unfavorable for migration. All these parameters signal cells through their mechanosensing pathway.

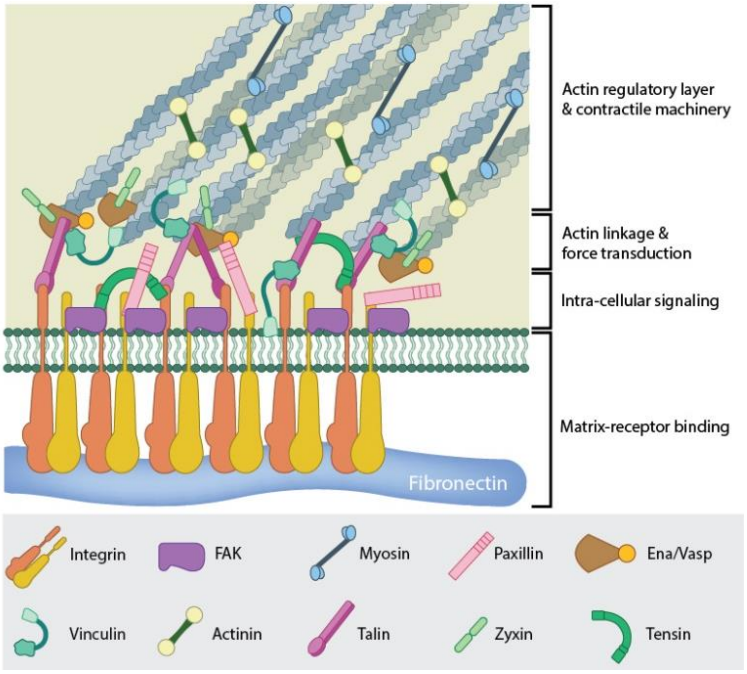

Figure 1.1 Focal adhesion complex. Figure from https://www.mechanobio.info. This work is licensed by Creative Commons Attribution-NonCommercial 4.0 International License. To view a copy of this license, visit http://creativecommons.org/licenses/by-nc/4.0/

1.1.2. Mechanosensation

Migration depends heavily upon the cell's ability to adhere to the substrate. It begins with the formation of new adhesions at the leading edge when the cell protrudes forward. Once FAs are formed and connect to actin fibers, the cell then contracts to move forward. As a result, old adhesions at the trailing end of the cell to detach. This sequence of events repeat for continual migration of the cell (**Figure 1.2**). Yet, adhesions alone are not enough to initiate migration. Connection to the actin cytoskeleton must also be established and this allows for mechanosensing proteins to be utilized. Talin and

vinculin are two FA proteins of the integrin-mediated adhesion network.[19,20] Talin bridges integrin to actin, which then allows for vinculin binding. It has been found that talin, when stretched with magnetic tweezers, opens a hidden binding site for vinculin and it defines the nanoscale architecture of the FA.[21,22] With stiffer matrices, the cell exerts more force on the matrix which exposes the binding sites for other proteins within the adhesion complex.[23] At the same time, increased branching of the cytoskeleton would occur to reinforce the growing adhesion complex.[18] Aside from the mechanical properties of the matrix, topography down to the nanoscale has also been shown to modulate FA protein clustering binding to the actin cytoskeleton.[24]

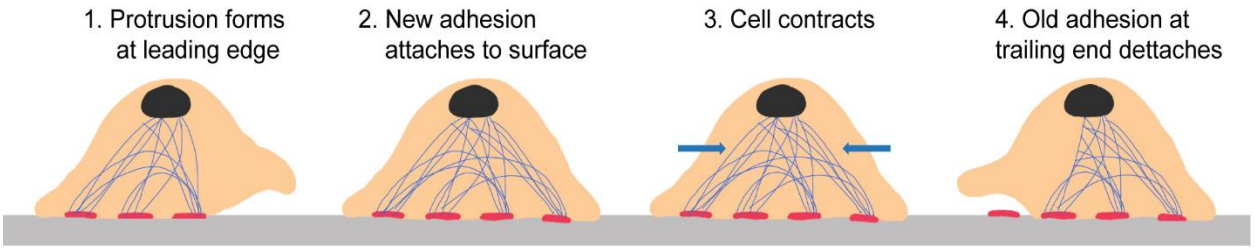

Figure 1.2: Cartoon of cell migration

Integrin proteins which are separated by more than 73 nm cannot cluster to form stable adhesion or attach to the actin cytoskeleton.[10,25–27] We have seen in our own studies that changes to topography on the nanoscale modulated the binding and unbinding dynamics of FA protein paxillin as well as its migration (**Chapter 2)**.[24] We also showed that cells on nanolined surfaces migrated uni-directionally along the line features. Similar observations have been made *in vivo*, where invading tumor cells

compact collagen fibers to further stiffen the ECM by combining multiple fibers into a larger single fiber, called "highways", to facilitate their migration.[28,29] This allowed us to use these nanoline features as a model to further understand how adhesions are affected by textured substrates, such as collagen matrices (**Chapter 4)**.

1.1.3. Substrate stiffness regulates cancer invasion

Metastasis occurs in a multi-step process (**Figure 1.3**).[30,31] First the cells migrate from the primary tumor by degrading and remodeling the ECM. Once the cells reach a blood vessel, the migrating cells intravasate into the blood circulation where they can migrate as well as proliferate to form tumor emboli. These emboli can arrest in circulation by adhesion to the inner vessel walls and extravasate into a secondary site. Here, the tumor cells can implant themselves and form a new tumor. In order to initialize the process of metastasis, cancer cells utilize specialized protrusions, invadopodia, to aid in its migration through the ECM after dissimilation from the initial tumor.

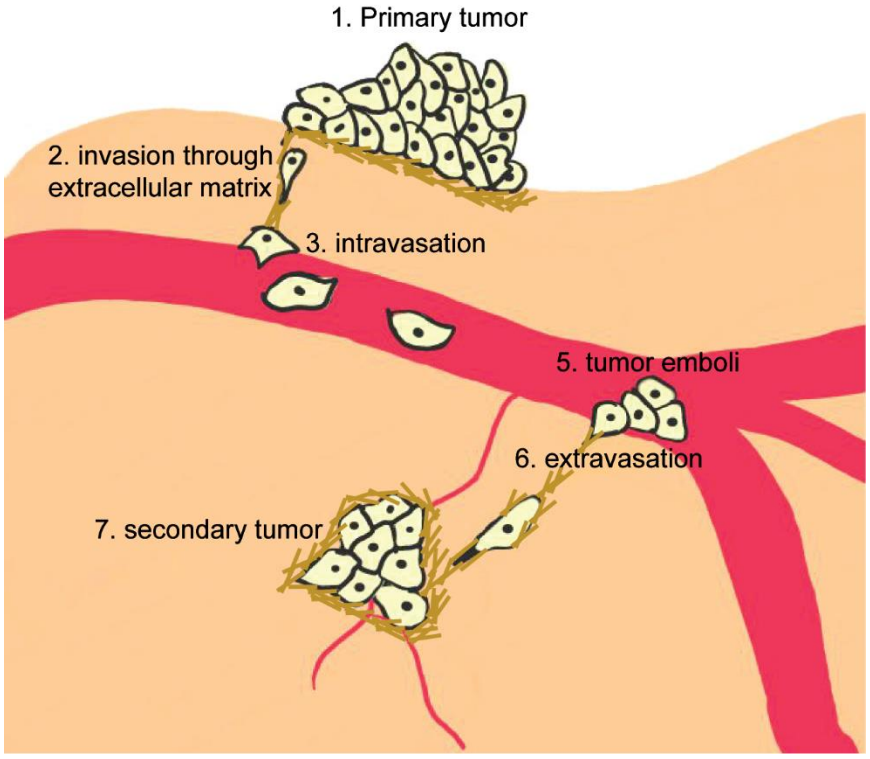

Figure 1.3: Process of cancer metastasis

Some of the key factors that allow early prognosis of cancer are tissue morphology and metabolic differences of cancerous cells compared to the surrounding healthy tissue. Numerous studies have shown that the elastic modulus of breast tumor tissues (~4 kPa) are about twenty times higher than that of normal tissue (~0.2 kPa).[32] This increase in stiffness has been shown to facilitate tumor cell invasion and extracellular matrix (ECM) degradation.[1,33,34] Additionally, observations of ECM remodeling and linearization of collagen by the tumor cells are seen, which contribute to the increase in ECM stiffness.[35,36] In order to compact or degrade the ECM for

invasion, actin-rich protrusions called invadopodia extend from the cell body and provide signals for matrix metalloproteinases.[37–42]

Invadopodia are actin-rich protrusions which are able to degrade the surrounding ECM and reorganize it.[37,41] These protrusions can extend >2 μm in length and 0.5-2 μm in diameter and facilitate the migration of the cancer cells through the basement membrane of the tumor and through the matrix. Similarly to FAs, invadopodia have integrin proteins at the tip, which interact with the ECM and facilitate invadopodia formation and matrix degradation.[12,39,43] Proteinases such as membrane-anchored type matrix metalloproteinase (MT-MMP2)[44], urokinase plasminogen activator receptor (uPAR)[12], and epidermal growth factor receptor (EGFF)[39] have been shown to co-localize with integrins and signal matrix metalloproteinases (MMP) locally[45]. As the cell degrades the ECM, it creates an opening to allow the cell body to migrate forward. Blocking the activation of integrin has been shown to decrease cell migration and invasion and expression of MMP-9.[46] Similar to how FAs form contact points to the ECM, they are also found as a rosette structure at the base of invadopodia (**Figure 1.4**).[47,48] This rosette allows stabilization of the invadopodia structure for extension through the ECM and for matrix degradation, making it a mechanosensing structure in cancer cells. It is clear that there is a strong

correlation between FA signaling and invadopodia formation to allow cancer cells to initiate metastasis.

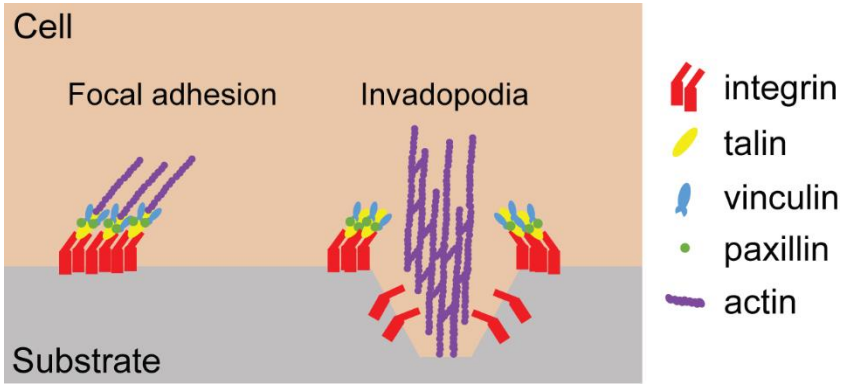

Figure 1.4: Focal adhesion and invadopodia structure

1.2. Modulation of cancer invasion by metabolism

1.2.1. Modes of metabolism within cancer

Aside from mechanical properties of the ECM, metabolism of the cancer cells has also been shown to regulate invasiveness. Metabolism within cells can undergo two processes: glycolysis (GLY), or oxidative phosphorylation (OXPHOS), to produce energy in the form of ATP. When the cell uptakes glucose, it is converted to pyruvate in the cytosol and can be transported to the mitochondria to undergo OXPHOS. Alternatively, pyruvate can be further broken down in the cytosol through GLY into lactate acid. Normal cells in the presence of oxygen prefer to produce ATP through OXPHOS due to a higher yield of ATP compared to GLY.[49] Cancer cells have altered cytosol and mitochondrial pathways where GLY will occur even in the presence of

oxygen, known as the Warburg Effect.[50–52] The current hypothesis is that GLY is the preferred mechanism for rapidly dividing cells due to its ability to produce ATP 10-100 times faster than OXPHOS.[52] Van Horssen *et al.* have shown that depletion of pyruvate or inhibition of GLY or OXPHOS through the addition of galactose or oligomycin, respectively, alters invadopodia function depending on the cell type.[50] Other studies have also shown that inhibition of acetyl-CoA carboxylase 1, an important step in the *de novo* fatty acid synthesis pathway, decreases invadopodia formation and ECM degradation.[53] Thus it is evident that both the mechanical properties and metabolism can alter the invasion phenotype of the cell. In **Chapter 3,** I will investigate if the mechanosensing and metabolism pathway within cancer cells are interconnected and if metabolism can be altered by the properties of the substrate.

1.2.2. The role of mitochondria at the leading edge

Mitochondria are known as the "powerhouse of the cell" because of its ability to produce high amounts of ATP per mole of glucose. Its transport towards the leading edge of the cell has been a new parameter of interest that can play an important role in metastasis.[54–56] Studies have shown that mitochondria transport within neuronal cells are required to distribute ATP to regions of high energy consumption, such as the nodes of Ranvier where a high density of Na^+/K^+ ATPase and Na^+ channels exist for rapid nerve impulses.[57] Inhibition of transport leads to neurodegenerative diseases such

as Alzheimer's, Huntington's, and Parkinson's.[58] Within cancer cells, a study by Desai *et al.* showed that during directed migration, mitochondria would relocate to the leading edge of the cell.[56] Similarly Cunniff *et al.* have shown that this recruitment of mitochondria is regulated by AMP-activated protein kinase (AMPK) activity and causes localized changes in metabolism within pseudopodia structures.[54] This phenomenon of recruitment has also been shown to exist within invadopodia and is possibly due to these regions being high energy efficient regions that require ATP for multiple functions such as actin polymerization, matrix degradation, and protrusion formation.[54,55] Thus, it is evident that metabolism differences within invadopodia play a role in invasion and mitochondrial recruitment to sustain their activity. **Chapter 4** will introduce some preliminary studies that further investigate if mitochondria recruitment correlates with changes in metabolism, GLY vs OXPHOS, during invasion over time.

1.3. Thesis summary and significance

Properties of the microenvironment can change the phenotype of cells and can determine if a cancer cell is benign or invasive. Current cancer therapies target metabolic pathways to prevent or delay the stages of metastasis.[59–61] There is evidence that a strong connection between mechanosensing and metabolism pathways exists in the regulation of cancer cell invasion. Thus, it is important to consider both the

metabolic state of the cell and the surrounding microenvironment when developing therapies. Furthermore, mitochondria trafficking towards the cell's leading edge has been shown to be important for migration.[54,56] It is possible that the transport of mitochondria also plays a significant role in cancer invasion. There is a lack of understanding of the specific metabolic pathways which are changed due to the microenvironment. Current methods are only able to detect bulk cell changes, but there is strong evidence that these metabolic changes can be different within subcellular compartments. In this thesis, I chronicle my studies on the role of integrin-mediated adhesion in cancer cells in mechanosensing, metabolism, and mitochondria trafficking. The following aims were addressed:

Aim 1: Characterization of focal adhesion protein dynamics on matrix topography (Chapter 2)

Aim 2: Investigate the link between matrix stiffness and metabolism within varying collagen densities (Chapter 3)

Aim 3: Quantify focal adhesion tension, mitochondrial transport, and metabolic change within invasive protrusions in 3D matrices over time (Chapter 4)

Chapter 2

2. CORRELATION OF PAXILLIN ADHESION DYNAMICS AND CELL MIGRATION ON NANOTOPOGRAPHY

2.1. Numbers and Brightness analysis for protein aggregation

The aggregation of focal adhesion (FA) proteins has been shown to be important for promoting the migration of cells[8,16]. Currently, there is a lack of techniques which allows quantification of the size and concentration aggregates within a cell in addition to mapping their location. Techniques for studying protein aggregation currently include the photon counting histogram[62,63], image correlation spectroscopy[64,65], or fluorescence resonance energy transfer (FRET) probes,[66,67] which labels their aggregation partners with the appropriate fluorescent probes. These techniques, however, still lack the ability to simultaneously quantify aggregation size and spatial location of the aggregates.

In our work, we used an imaging analysis technique, called Number and Brightness (N&B), which allows spatial mapping of aggregates of various sizes[68–70]. By looking at the fluctuations of the fluorescent molecule over time in every pixel in our image, we can calculate the average and variance of those fluctuations, which will indicate the aggregation state of the molecule in each pixel (**Figure 2.1**). The variance of the fluctuations allows differentiation of whether the calculated average is due to many small molecules (e.g. monomers), or few aggregates (e.g. dimers, trimer, etc). Equations used to calculate the N&B values are outlined in the **Materials and Methods section** of this chapter. This technique has been implemented previously in our lab for studying aggregation states of FA protein, paxillin.[70] In this thesis, we utilize this technique to quantify paxillin protein dynamics on nanotopography.

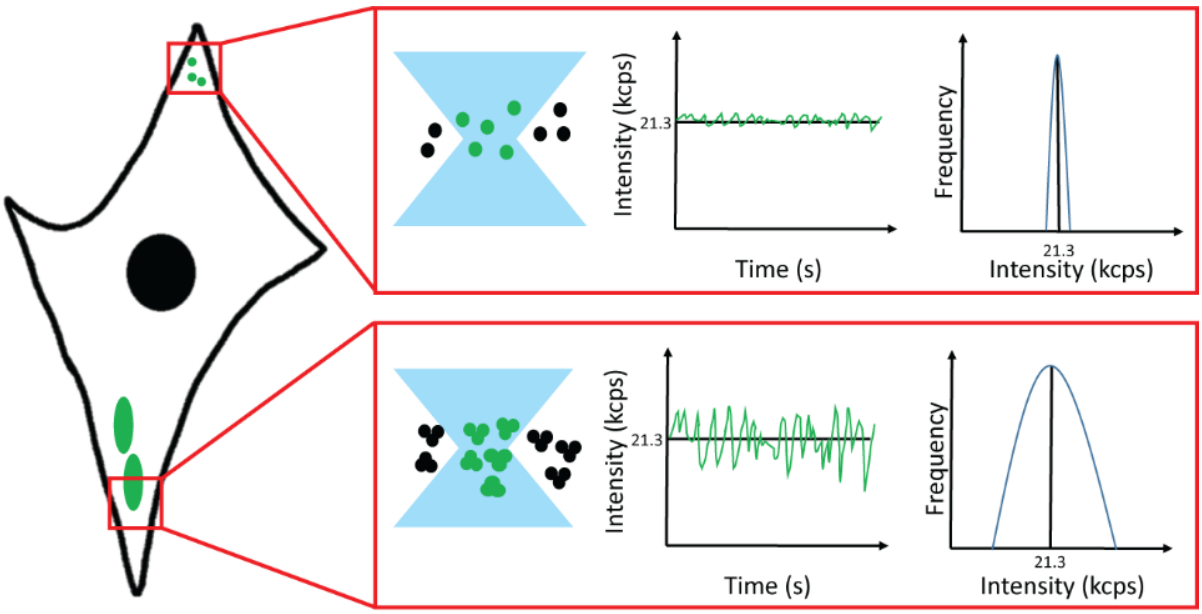

Figure 2.1: Cartoon description of Numbers and Brightness analysis. Average intensity and standard deviation of protein fluctuations (green) within the point spread function (blue) are detected to calculate the brightness and aggregation state in every pixel of the image.

2.2. Chapter 2 Abstract

The interaction of the cells-to-substrate or cells-to-extracellular matrix (ECM) regulates key biological processes such as adhesion, migration, proliferation, and differentiation. Mesenchymal cell migration is regulated through focal adhesions (FAs) and can be modulated by their microenvironment, including changes in surface topography. We are able to quantify the binding and unbinding dynamics of focal adhesion protein paxillin with an imaging analysis technique called Number and Molecular Brightness (N&B). The N&B analysis generates a map of real-time

fluctuations of protein monomers, dimers, and higher order aggregates of FA proteins, such as paxillin, from which information about adhesion assembly and disassembly can be extracted. We demonstrate how nanostructured surfaces (nanoline gratings or nanopillars) regulate single molecular dynamics. We found that the smallest nanopillars (100 nm spacing) gave rise to a low percentage population of disassembling adhesion cluster size of ~2 paxillin proteins/cluster, whereas the larger nanopillars (380 nm spacing) gave rise to a much larger population of larger disassembling clusters of ~3-5 paxillin proteins. In addition, cells were found to be more motile on the smaller nanopillars (spaced 100-130 nm apart) compared to all other surfaces studied. These results show that physical nanotopography influences cell motility, adhesion size, and adhesion assembly and disassembly. We report for the first time our study using single molecular detection and demonstrate that nanotopography influences cell motility and adhesion protein dynamics.

2.3. Introduction

Cell-to-substrate interactions play a key role in regulating processes such as migration, adhesion, proliferation, and signaling.[71,72] Trans-membrane proteins called integrins adhere to the extracellular (ECM) matrix to regions containing a tri-peptide sequence, RGD, composed of L-arginine, glycine, and L-aspartic acid.[25,73] These

integrins signal other focal adhesion (FA) proteins to be recruited and cluster to form the adhesion complex, which will bind to the actin cytoskeleton to establish the mechanosensing network in the cell.[8,19,71] As the cell experiences more traction, the FA complex grows through additional integrin clustering and actin polymerization. There has been a variety of means to study cell adhesion with the use of micro- and nano-contact printing to transfer extracellular matrix (ECM) proteins onto the substrate, which either prevents or promotes adhesions and cell spreading.[74–78] However, these methods only measure a two-dimensional (2D) surface and are not representative of the three-dimensional (3D) *in vivo* environment. By using quasi-3D nanostructured surfaces, we are able to unveil important clues to the role of FA complexes with respect to those structured surfaces.

We utilize nanoimprint lithography to produce 2.5-D nanostructures on surfaces of poly(methyl methacrylate) (PMMA) with one line pattern (L) and pillar patterns (P) of different dimensional arrays. Our nanotopography arrays are denoted as L860, P700, P600, P300, P200 where the numerical values signify the center-to-center spacing of the structures in nm. **Figure 2.2** and **Table 2.1** summarize the dimensions of the features and their spacing with respect to each other. The sizes of the nanofeatures were chosen based on findings from previous work.[79–82] L860 was used as a reference due to the fact that cell behavior has been well characterized on these types of structures.[81,83–85]

Nanostructures have been shown to modulate migration such that cells would migrate parallel to the line features and form adhesions[81,84,86,87] while those on nanopillars form smaller adhesions and migrate omnidirectionally.[10,79,88] During cell migration, new adhesions form at the leading edge while older adhesions disassemble at the trailing edge during contraction to move forward.[9] Many of these studies examine the role of FAs during cell migration by staining for focal adhesion proteins; however, this method fails to capture the dynamics of proteins at the FAs. We overcome this deficiency by looking at the single-protein scale in live cells to understand the formation of adhesions on these patterns and their role in cell migration.

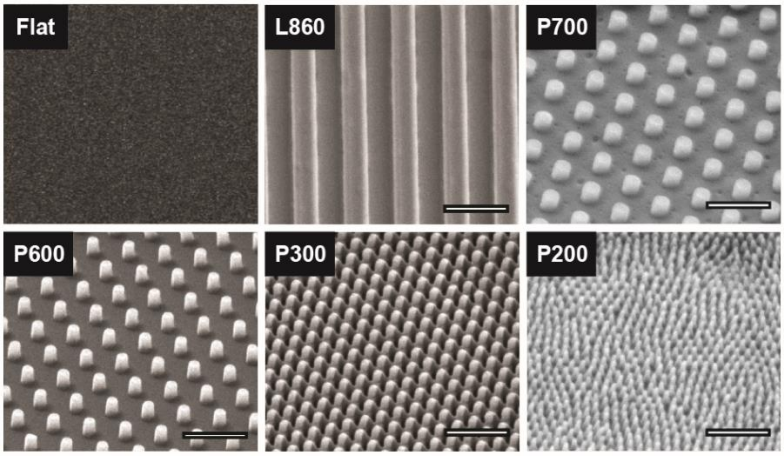

Figure 2.2 SEM images of PMMA nanostructures. Nanotopographies include one line pattern (L860, line width = 430 nm) as a reference, 4 pillar patterns (P700, P600, P300, P200; pillar widths = 267 nm, 215 nm, 190 nm, 70 nm, respectively) and a PMMA film as the flat control. SEM images were taken at 5 kV with FEI Quanta 3D (scale: 1μm) at 30° tilt.

Table 2.1: Nanostructure dimensions

Pattern	Feature Width (nm)	Feature Height (nm)	Array Periodicity (nm)
L860	430	200	860
P700	267	300	692
P600	215	300	595
P300	190	300	320
P200	70	210	170

Previous studies in our lab have shown that the focal adhesion protein, paxillin, forms adhesions as single proteins while its disassembly occurs in large clusters **(Figure 2.3)**. More recent developments in Fluorescence Correlation Spectroscopy (FCS) enable spatiotemporal detection of single molecules. We can calculate the molecular brightness of individual molecules by utilizing the photon counting histogram analysis within the diffraction-limited volume (~250 nm).[62,63,89] This can then be expanded to an image where protein aggregation states could be mapped pixel-by-pixel by using an image analysis technique, namely, Number and Molecular Brightness (N&B).[68,70]

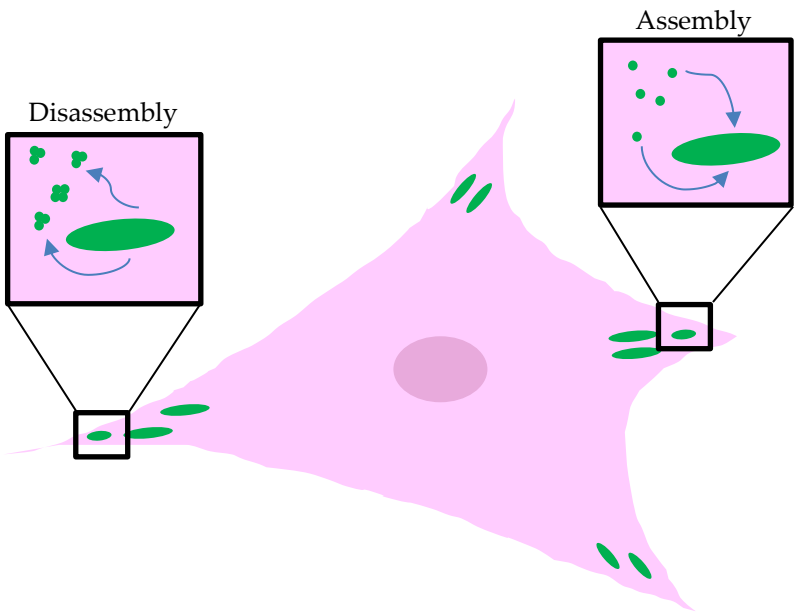

Figure 2.3 Focal adhesion dynamics. Paxillin forms at the adhesion as monomers and disassembles as aggregates during migration

With the N&B analysis, we were able to observe the assembling and disassembling dynamics of paxillin by looking at their aggregation ratios. These were then compared to the adhesion size and average migration distances within NIH3T3 fibroblasts plated on a flat surface, a nanoline pattern, and nanopillars of varying width and periodicity**.** Cells on the smallest nanopillars (P200 and P300) exhibited the highest motility but had the lowest population of disassembling clusters of protein (~2 paxillin/cluster). When grown on pillars spaced 380 nm apart (P600), they exhibited the largest population of higher order protein aggregates (~ 3-5 paxillin/cluster) and concurrently larger disassembly adhesions. The adhesion size on the nanopillars decreased with nanostructure size, while those on the nanoline surfaces were in the

middle of this range. This first report of such observations provides a deeper understanding of the dynamics of adhesion formation and disassembly on nanotopography and its role in cell migration.

2.4. Results and discussion

2.4.1. Cell Migration on nanostructured surfaces

We observed the migration of cells on the nanostructures by imaging the cells for 12 hours at a rate of 1 frame/minute. The surfaces were coated with fibronectin to allow cell attachment. We made the reasonable assumption that the glassy PMMA polymer behaved as a rigid material in comparison with the rigidity of cells. Only cells which were present in the first frame were used for the analysis until they divided, underwent apoptosis or left the frame. Cells which entered the frame later were excluded.

After tracking the cells that met our criteria described above for 12 hours, we calculated the average radius of the migration trajectory traveled by the cells on each surface by calculating the distance between the first point and the furthest point traveled. Cells on L860 **(Figure 2.4)** generally migrated along line structures within an average net radius of 150 μm, while those on flat surfaces **(Figure 2.4a)** migrated in random directions within an average net radius of 112 μm. More significantly, cells on

P300 and P200 nanopillars traveled within an average net radius of 154 and 153 μm, respectively ($p<0.01$ for P300 vs. flat surfaces, $p<0.05$ for P200 vs. flat surfaces).

We then determined the migration speed **(Figure 2.4g)** and the total migration distance traveled of each cell on the nanostructured surfaces **(Figure 2.4h)** to determine if there were any correlations to the underlying nanostructures. We defined the total migration distance as the sum of the distances traveled at each time point. Total migration distances of cells on nanostructures P700, P600, and flat surfaces were very similar: 372, 336, and 387 μm, respectively. Correspondingly, cells on flat and P700 surfaces migrated at similar average speeds of 0.55 and 0.57 μm/min, respectively, while those on P600 surfaces migrated at 0.48 μm/min. Cells on P300 and P200 nanostructures had an average total distance traveled of 472 and 483 μm, respectively, indicating that they were the most motile. When cells were grown on P200 pillars they migrated at higher average speed than on all other surfaces at 0.75 μm/min ($p<0.01$). This could be due to the fact that cells on P300 pillars had more periods of rest (i.e., no displacement) compared to cells on the P200 pillars. Over the 700-minute period of our observation, cells on P300 were immobile for on average 82% of the time, while cells on P200 were immobile for on average 71% of the time. This shows that the adhesions formed on P200 pillars were less stable than those on the P300 pillars, perhaps due to the smaller diameter of the features on P200 surfaces.[79] This would explain the

inconsistency of the results between average speed versus the total distance traveled by cells on P300 and P200 pillars.

Cells on L860 surfaces traveled the shortest total distance on average (229 μm) and had a significantly lower speed than those of cells on the other surfaces (0.36 μm/min; $p<0.01$). Similarly to the cells on P300, the cells on L860 were immobile for 89% of the time, which could explain why their speed and average distance traveled is lower. These results should be compared with findings in other studies that showed increased migration of cells on nanolines (width = 350 nm to 6 μm, spacing = 70 nm to 4 μm) compared to those on flat surfaces.[3,72,90] However, our results are similar to those of Ferrari et al., who studied cells on nanolines of similar size as L860. They also observed that the cells on their surfaces traveled a shorter distance over time compared to cells on flat surfaces.[81] This suggests that the size of the line gratings may affect the formation of the adhesions and cytoskeletal structures, which are necessary to provide the correct orientation of the cell body for optimal migration. In addition, cells on the L860 patterns initially take time to elongate along the nanostructures before motion is observed. This could be why we observe less cell motility on the nanolines within the time frame of tracking.

The preceding results demonstrate that pillar size and spacing contributed to the changes in migration speed and distance traveled. It has been found that integrin

proteins separated more than 73 nm apart are not able to dimerize and form the FA complex and the actin cytoskeleton.[10,26,91] Our nanostructures have an inter-pillar spacing greater than 73 nm for studying the effect of potentially unstable adhesions. In particular, the P700 and P600 pillars had similar diameters and spacings; the difference in spacing between the two surfaces is only 45 nm. Similarly, the P200 and P300 pillars differed in spacing by only 50 nm, which could explain why the cells traveled similarly on these respective sets of pillared surfaces.

It is important to note that three to five integrin heterodimers are necessary for the FA complex to form.[92] The diameters of the P200 and P300 pillars were 70 nm and 190 nm, respectively, which could result in small adhesions (about 15-30 integrin proteins) that would more easily disassemble during migration.[16] This supports our findings that the high motility was found in cells grown on the P300 and P200 patterns. In addition, this means that the focal adhesion protein dynamics could be modulated by the underlying surface morphology. In the next section, we describe how we utilized the N&B analysis to quantify the assembly and disassembly dynamics of the adhesion protein, paxillin, within cells on the various nanostructures.

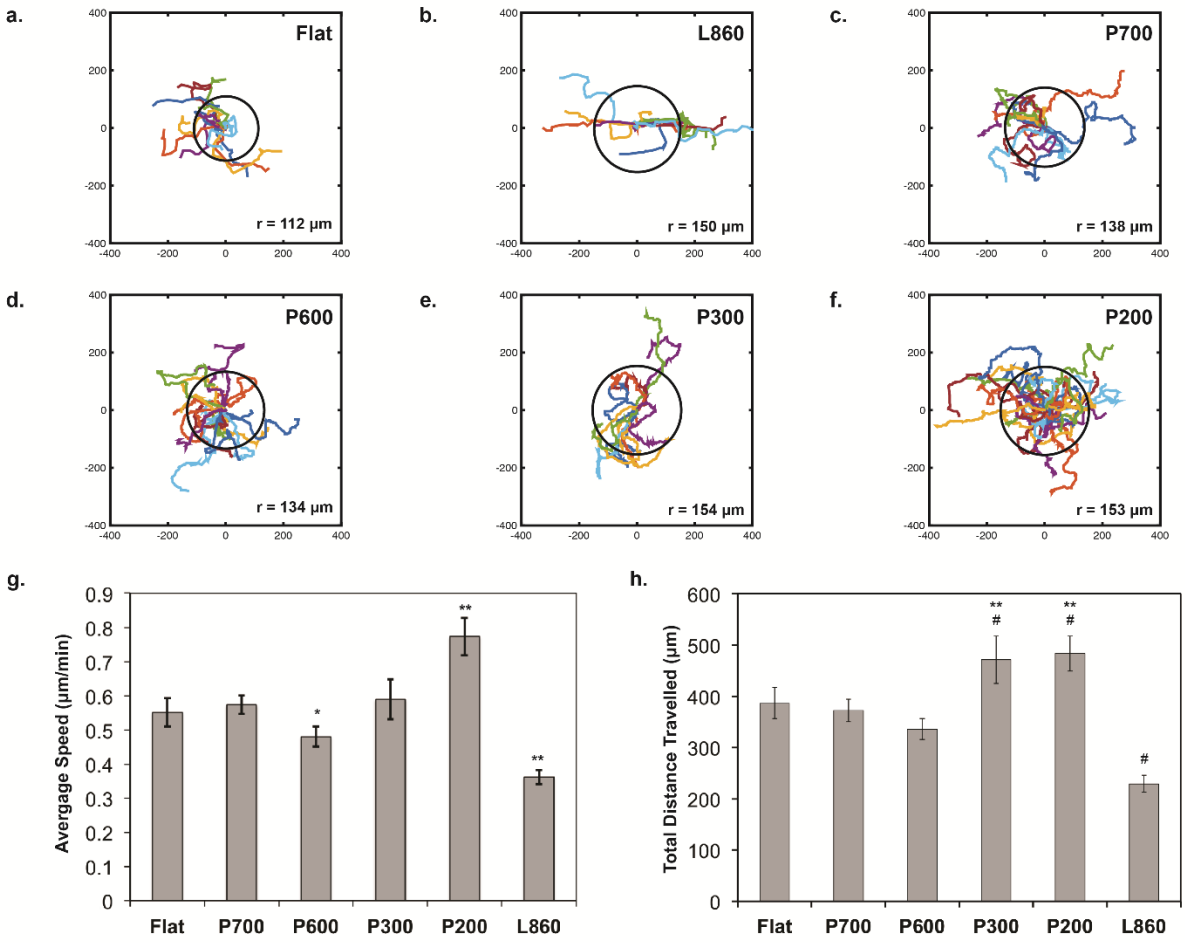

Figure 2.4 Migration behavior on nanostructured surfaces. Migration trajectories of 3T3 cells over 12 hours on (a) flat surface, n=54 cells; (b) L860 lines, n=63; (c) P700 pillars, n=70; (d) P600 pillars, n=72; (e) P300 pillars, n=32; and (f) P200 pillars, n=36. The axes display coordinate values in μm. All surfaces were coated with fibronectin (1 μg/ml). Black circles in plots represent the net radius of migration trajectories of cells on each surface. (g) Average migration speed of cells. The values below each pattern represent mean ± standard error of the mean (S.E.M.) Statistical significance was assessed using the Student's t-test: *: $p<0.05$ compared to P700; **: $p<0.01$ compared to other surfaces. (h) Total distance traveled on

nanostructured surfaces over 12 hours. Data represent mean ± S.E.M. Statistical significance was assessed using the Student's t-test. **: $p<0.01$ compared to L860; #: $p<0.01$ compared to Flat, P700, and P600.

2.4.2. Quantification of paxillin dynamics and focal adhesion size on nanotopography

The process of binding and unbinding of focal adhesion proteins is dynamic. Adaptor proteins within the adhesion complex, such as paxillin and many others, bind each other with tight affinity. This results in conformational changes of the proteins that trigger other proteins that assemble at the adhesion. We showed previously in our lab that paxillin assembly occurs as monomeric proteins and disassemble as aggregates.[70,93–95] This is necessary during processes that are highly dynamic, such as migration. We speculate that the cells utilize proteases such as calpain to cleave focal adhesion proteins, such as talin, which binds to the actin cytoskeleton.[96] When adhesions are cleaved, conformational instability results in the adhesive proteins, which begin to dissociate. These are then quickly returned to their monomeric form to be recycled or disposed of.[93] This transition process allows us to apply the Number and Brightness (N&B) analysis, a powerful tool that graphically quantifies the aggregation states of diffusing proteins within live cells, and use the results to characterize adhesion protein dynamics.

NIH3T3 cells were transfected with the paxillin-EGFP and imaged for 100 frames to observe the diffusion of paxillin over time. The N&B analysis was then used to quantify the aggregation states of paxillin at the adhesions. The average intensity of paxillin-EGFP overtime during which the variance of this intensity was recorded. This allows us to calculate the molecular brightness and translate these values to an aggregation state.[68] A brightness map that plots the brightness versus intensity of every pixel in the original image is then generated. In order to calibrate our readings, the number of cells expressing monomeric EGFP (mEGFP) was calculated to find the molecular brightness of a monomer (**Figure 2.5**). **Figure 2.5a** showed a gradient of mEGFP in the cell: a higher concentration at the center of the cell (red) and less at the edges (blue); this shows that the average intensity alone is not enough to define the aggregation state of the proteins. The brightness map of the same cell, which also accounts for the variance of the intensity, showed a uniform coloring of the cell in red, indicating pixels which have a brightness value corresponding to monomers. With such an indication of the apparent brightness of mEGFP, we are able to use it to calculate the molecular brightness of a dimer or higher order aggregates, by multiplying its value accordingly (doubling for dimers, tripling for trimers, etc.). For our results, we combined the population of trimers, tetramers, and pentamers into one tier. In **Figure 2.6**, red, green, and blue pixels was used to map out the location of monomers, dimers

(~2 paxillin proteins/cluster), and higher order aggregates (~3-5 paxillin proteins/cluster), respectively. Pixels of the original image were colored according to the corresponding cursors representing each aggregation state (**Figure 2.6a**).

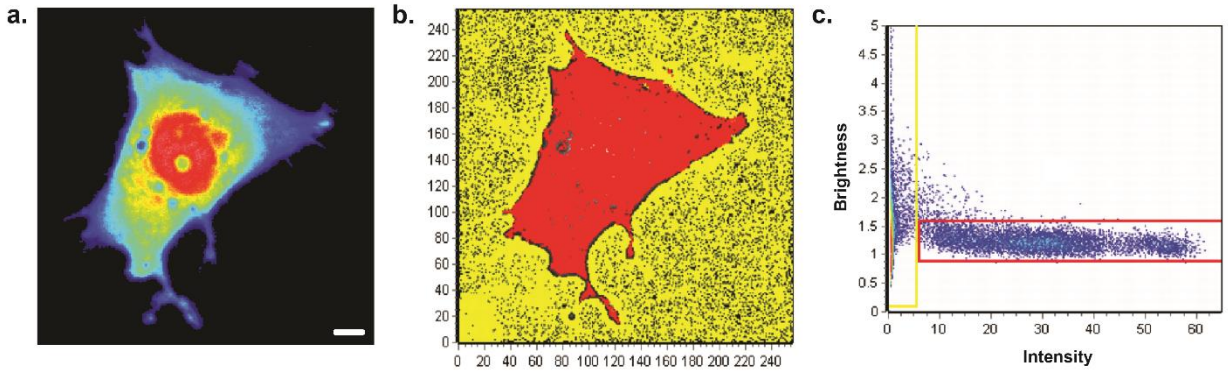

Figure 2.5 Analysis of monomeric GFP brightness. (a) The average intensity of monomeric EGFP (mEGFP) in a cell only expressing mEGFP on a flat surface. Scale = 5 μm. (b) Brightness map of the same cell. Red pixels highlight monomer EGFP, while yellow pixels highlight background. This monomeric brightness value was used to calculate the brightness of all other aggregate tiers. (c) The brightness of every pixel of image versus intensity generated from the N&B analysis. Color cursors are used to highlight the cell according to their brightness value.

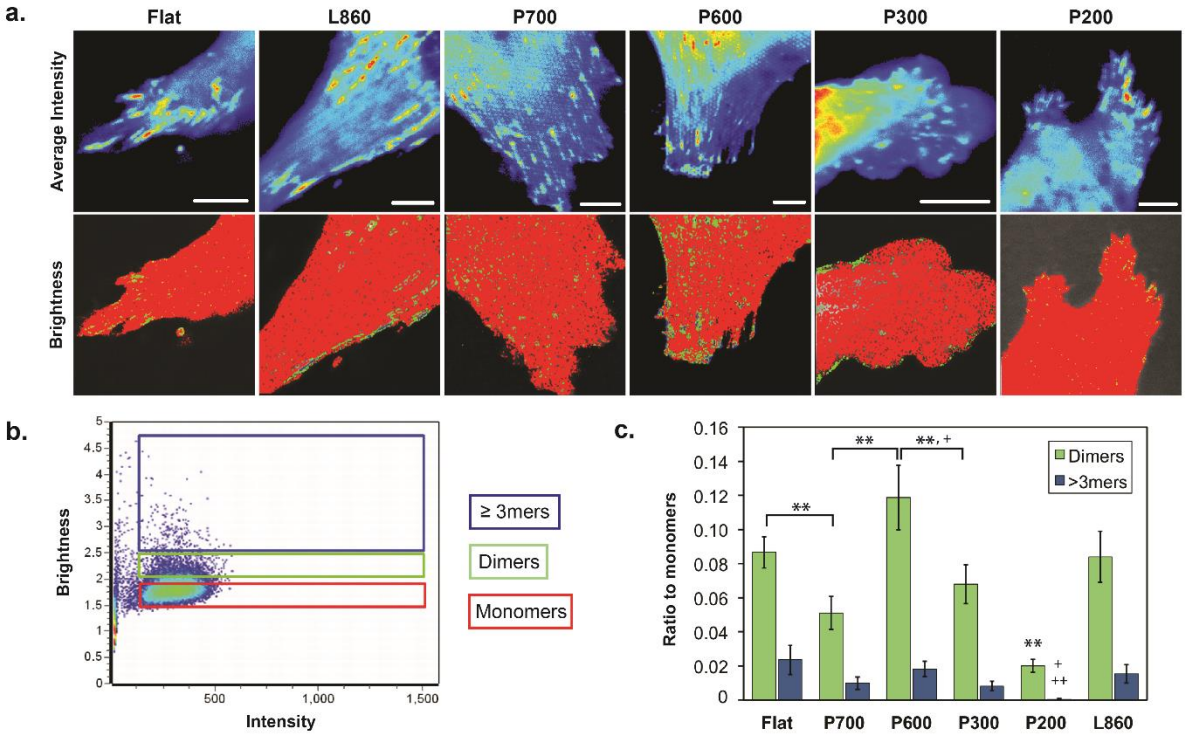

Figure 2.6: Paxillin aggregation states of adhesions in cells on nanostructured surfaces. (a) Average fluorescence intensity of the trailing edges of NIH3T3 fibroblasts (scale = 5μm) and their corresponding brightness maps. Colors correspond to pixels of monomers (red), dimers (green) and higher order aggregates (blue) of diffusing paxillin. (b) The plot of the brightness of every pixel in an image versus its intensity generated from the N&B analysis. This representative plot is of cells on P600 pillars. (c) The ratio of dimers to monomers (D:M; green) and higher order aggregates to monomers (H:M; blue) in cells on nanostructured surfaces. Cells on P600 pillars (n=16 cells) exhibited the largest D:M and H:M ratios, indicating that the adhesions in those cells have a larger population of higher order aggregates. Cells on the other pillars (P700: n = 11; P300: n = 15; P200: n = 10) had smaller ratios compared to those on flat (n=12) and L860 lines (n-16). Data represent mean ± S.E.M. Statistical significance was assessed using the Student's t-test. *: $p<0.05$ for D:M ratios; **: $p<0.01$ for D:M ratios; +: $p<0.05$ for H:M ratios; ++: $p<0.01$ for

H:M ratios. For P200: **: $p<0.01$ for D:M ratios compared to all other surfaces; +: $p<0.05$ for H:M ratios compared to flat and P700; ++: $p<0.01$ for H:M ratios compared to P600, P300, L860.

Due to the definition of molecular brightness, stably attached adhesion proteins that do not go under any diffusion will not show any fluctuations of their intensity over time. This will result in a brightness value of 1. An example of this is shown in our image of a typical cell on a flat surface in **Figure 2.6a**. The average intensity image of paxillin-GFP on the flat substrate shows that many adhesions are present. However when looking at the corresponding brightness map, the pixels containing these adhesions are highlighted red, or a brightness of 1. In order to quantify the population of aggregates, we quantified the number of pixels highlighted by each cursor in the brightness versus intensity plot and calculated the ratio of pixels of each aggregation tier to the pixel of monomers. This allowed us to normalize our images. The ratio of dimers to monomers and higher order aggregates to monomers is denoted D:M and H:M, respectively. The observed cells appeared to retract during these measurements, thus, we could quantify the disassembling adhesions with high accuracy contemporaneously. Based on reports of the behavior of paxillin during focal adhesion assembly and disassembly,[70] we hypothesize that highly motile cells will have an increased population of paxillin aggregates due to increased adhesion disassembly.

With the N&B analysis, we were able to make distinctions between cells which showed similar degrees of motility. This was done by calculating the D:M and H:M ratios in NIH3T3 cells on all surfaces, as shown in **Figure 2.6c**. We found that D:M and H:M ratios in cells on flat and L860 lines were similar to one another, although our migration data showed that the cells on the L860 patterns had a shorter distance traveled over the period of 12 hours. Out of the D:M and H:M ratios for cells on the four nanopillar patterns, cells on the P600 pillars showed the highest aggregation ratio (0.12 for D:M, 0.02 for H:M), indicating that the adhesions in these cells had a larger population of higher order aggregates. However, cells on this surface traveled the least distance over time. In fact, cells were the most motile on the P200 pillars, but contrary to our initial hypothesis, adhesions in these cells consisted mostly of monomers. It is important to note that the size of the adhesions also contributes to the rate of adhesion disassembly during cell migration.[93] Cells which have smaller adhesions will give rise to a lower population of disassembling units and larger adhesions will give a larger population of units. We speculate that the cells on P600 nanopillars which had the greatest percentage of dimers and higher order aggregates would have the largest adhesions. In addition, larger adhesions will take more time to fully disassemble and result in decreased cell motility within a specified time frame. The focal adhesion area of the images used for the N&B analysis was measured and it was found that NIH3T3

cells on P600 surfaces indeed had the largest focal adhesion area (~1.0 μm^2) while those on the P200 pillars were the smallest (~0.34 μm^2), as shown in **Figure 2.7**. These results support our hypothesis that nanotopography affects the dynamics of focal adhesion disassembly due to the size of the adhesions they are able to form on the features.

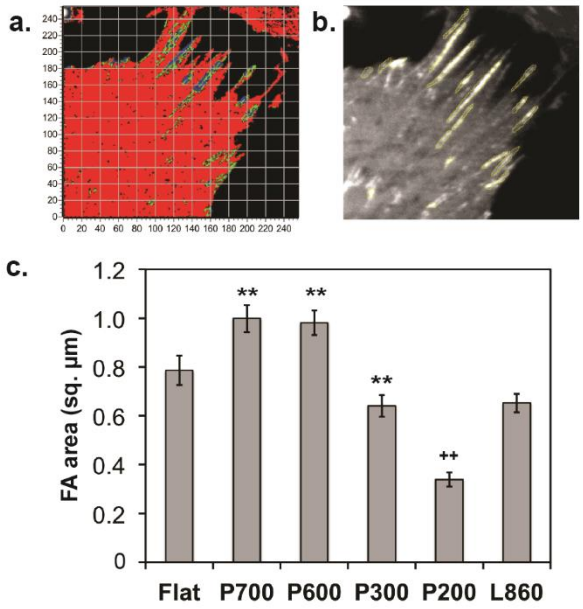

Figure 2.7: Area of disassembling adhesions on nanostructured surfaces. (a) Brightness map of trailing edge of a cell on P700 pillars. Adhesions involved in disassembly contain greater populations of dimers and higher order aggregates of paxillin. (b) Adhesion area of these adhesions was measured by using the free selection tool in ImageJ. Flat: n=152 adhesions, P700: n=258, P600: n=408, P300: n=71, P200: n=192, L860: n=299. (c) The largest adhesions were found in cells on the P700 and P600 pillared surfaces compared to flat and L860 lines. The smallest adhesions were in cells on the P200 pillars. The values below each pattern represent the mean. Error bars represent S.E.M. Statistical significance is assessed using the Student's t-test. **: $p<0.01$ for P700, P600 compared to flat and L860, and for P300 compare to P700, P600; ++: $p<0.01$ for P200 compare to all patterns.

2.5. Materials and methods

2.5.1. Cell lines and reagents

NIH 3T3 fibroblasts (ATCC, CRL-1658) were cultured in high-glucose Dulbecco's modified Eagle's Medium (Life Technologies, Rockville, MD) containing 10% (v/v) fetal bovine serum (FBS, Life Technologies, Rockville, MD), 1% (v/v) nonessential amino acids, and 1% penicillin-streptomycin (Life Technologies, Rockville, MD) and maintained at 5% CO_2 and 37°C. Cells were washed with 1X Dulbecco's Phosphate Buffer Saline (Life Technologies, Rockville, MD) and detached with 1X Trypsin in EDTA (Life Technologies, Rockville, MD) for plating. Before adding cells, all surfaces were coated with 1 μg/ml fibronectin (Sigma, Aldrich, Milwaukee, WI). Migration experiments were conducted by seeding 100,000 cells on each nanostructured and flat surfaces. NIH3T3 cells were seeded into a 6-well culture plate overnight and transfected with 1 μg monomer EGFP or paxillin-EGFP DNA plasmids (both were generous gifts from Rick Horwitz, University of Virginia) following the manufacturer's protocol for Lipofectamine 2000 (Life Technologies, Rockville, MD). Transfected cells were then transferred to the nanostructured surfaces and incubated for 1-2 hours at 37°C in 5% CO_2 before conducting imaging experiments.

2.5.2. Fabrication of Nanostructures

Nanostructures were fabricated on thin films of poly(methyl methacrylate) (PMMA) cast on glass coverslips (#1.5, 22 x 22 mm) that were treated with UV-ozone for 5 minutes and then coated with 3-aminopropyltriethoxysilane (APTES) in deionized water (1 volume %) to facilitate PMMA adhesion to the glass. PMMA (M.W. = 120 kDa, Sigma-Aldrich, Milwaukee, WI) was dissolved in toluene (5 weight %) and spin-coated on glass coverslips at 600 rpm for 45 seconds. Films were heated on a hot plate at 100°C for 5 minutes to remove residual solvent. The film had a thickness of about 500 nm (data not shown). Nanostructures were fabricated by nanoimprint lithography following protocols previously described.[80] Nanoimprinted structures included one line pattern, designated as "L860" (periodicity = 860 nm, depth = 200 nm, duty cycle = 50%) as a reference, and four types of pillars, designated as "P700," "P600," "P300," and "P200," shown in order of decreasing periodicity. Nanostructures were characterized by scanning electron microscopy (SEM; FEI Quanta 3D, 5 kV).

2.5.3. Sample Preparation

Custom-made sample dishes were prepared for all experiments by using a heated 15-mm cork borer (to ~100^0C) and then immediately pressed into the center of a 35-mm polystyrene culture dish (Corning, Midland, MI). The edges of the hole were sanded down until smooth. The PMMA-on-glass coverslips containing the printed

structures were mounted onto the bottom of the bored culture dishes with clear silicone adhesive (Corning, Midland, MI) so that the nanostructured region was placed in the center of the opening. The mounted samples were dried overnight before use. Prior to commencement cell culturing, the samples were UV-sterilized for 5 minutes. Nanostructured surfaces were coated with 1 μg/mL of fibronectin (Sigma-Aldrich, St. Louis, MO) for 1 hour at 37°C before cell seeding.

2.5.4. Imaging

A Zeiss LSM 710 Axio-Observer inverted microscope was used for migration experiments and the paxillin aggregation measurements for flat, L860, P700, P600 and P300 surfaces. Time-lapse imaging migration experiments were performed using an EC Plan-Neofluar 20X/0.5 M27 air objective with the Zeiss LSM 710 with cell incubation at 37^0C and 5% CO_2 during the entire imaging session. Images are 512 by 512 pixels at 8-bit depth. The pixel dwell time was set to 1.58 μs with one-minute intervals for 12 hours using the transmission pathway.

For aggregation experiments, cells were imaged using a C-Apochromat 40X/1.2NA Korr M27 water immersion objective. Cells were excited with a 488-nm argon laser. An excitation dichroic was used to send the laser beam to the sample and the emission pathway consisted of a diffraction grating to disperse the emitted light. Two prisms were used to select the emission band for each photomultiplier tube (PMT).

500-550 nm was used to collect the EGFP signal. Image acquisition was performed with a 12.5 μs per pixel dwell time as a continuous time series of 100 frames (size = 256x256 pixels). Images were taken at 12-bit depth. Cells were kept under incubation chamber set to 37 °C and 5% CO_2 while imaging.

Paxillin aggregation of cells on P200 was measured using the Olympus FluoView FV1000 and a 60X/1.2 NA water immersion objective (Olympus, PA). Cells were excited with a 488-nm argon laser. The emission was collected with a BA505-605 bandpass filter. Images (size = 256x256 pixels) were collected at 10 μs per pixel dwell time for 100 consecutive frames.

2.5.5. Cell Migration Analysis

Images collected for the migration experiments were analyzed using the Manual Tracking plugin in Fiji (ImageJ) software.[97] The positions of the cells were tracked for each surface in each experiment by following the nucleus of the cells. Cells included in tracking were those present at the first time point so that all cells were exposed to the same initial condition. Tracking of the cells was cut off at 700 frames (approximately 12 hours) since this was the longest time that a majority of the cells remained in the imaging frame without dividing or undergoing apoptosis. Migration experiments were performed on three separate occasions per surface. The migration path of each cell was plotted in MATLAB using coordinates collected from Manual Tracking. The first

coordinates of each path were set at the origin, and the remaining coordinates were adjusted using the first coordinates as the reference.

2.5.6. Paxillin Aggregation Analysis

The N&B analysis was performed to assess paxillin aggregation using the SimFCS program developed at the Laboratory for Fluorescent Dynamics (LFD) at UC Irvine. Cells expressing paxillin-GFP were seeded on each fibronectin-coated surface with or without the nanostructures and incubated for 2 hours under specified culture conditions before imaging the adhesions. Imaging soon after cell attachment ensures that the cells are in an active state and accurate N&B measurements can be captured. For the N&B analysis, images of adhesions of at least ten cells were de-trended using a moving Gaussian average. The molecular brightness of cells transfected with monomeric GFP was first assessed to obtain the brightness of paxillin monomers. This value was then used to calculate the brightness of paxillin dimers and higher order aggregates by multiplying by a factor of 2 for dimers, and 3 or greater for higher order aggregates. Details of the mathematics and analysis process have been previously described.[68]

A brief description of the N&B analysis is given here. 100 frames were collected over time so that each pixel in the image contains intensity fluctuations of the proteins as a function of time. The average intensity (first moment) of each pixel $< k >$ were

calculated along with its variance σ^2 (second moment). The first and second moments were calculated with **Equations 2.1 and 2.2**, respectively, where *K* is the total number of frames collected, k_i is the intensity of pixel *i* collected over time.

$$< k >= \frac{\sum_i k_i}{K} \tag{2.1}$$

$$\sigma^2 = \frac{\sum_i (k_i - <k>)^2}{K} \tag{2.2}$$

During the analysis, variance, a combination of the occupation number (σ_n^2) and additional contributions from the detector such as shot noise or count statistics (σ_d^2), were calculated. These two parameters are a function of the true molecular brightness, ε, and the average number of molecules illuminated within the focal volume, n, as shown in **Equations 2.3-2.5**.

$$\sigma_n^2 = \varepsilon^2 n \tag{2.3}$$

$$\sigma_d^2 = \varepsilon n \tag{2.4}$$

$$< k > = \varepsilon n \tag{2.5}$$

The apparent brightness (B) for each pixel was defined as the ratio of the variance and average intensity. This was also used to calculate the apparent number of particles (N) as a fraction of the total intensity. Both **Equations 2.6 and 2.7** below show the mathematical formulas for B and N. By rewriting **Equations 2.6 and 2.7**, the values of n and ε were easily calculated, as shown in **Equations 2.8 and 2.9**.

$$B = \frac{\sigma^2}{<k>} = \frac{\sigma_n^2}{<k>} + \frac{\sigma_d^2}{<k>} = \frac{\varepsilon^2 n}{\varepsilon n} + \frac{\varepsilon n}{\varepsilon n} = \varepsilon + 1 \tag{2.6}$$

$$N = \frac{<k>^2}{\sigma^2} = \frac{\varepsilon n}{\varepsilon+1} \quad (2.7)$$

$$n = \frac{<k>^2}{\sigma^2 - <k>} \quad (2.8)$$

$$\varepsilon = \frac{\sigma^2 - <k>}{<k>} \quad (2.9)$$

For images with immobile fractions, the above expressions did not hold since there would not be any temporal fluctuations. Thus, the apparent molecular brightness would equal 1 (B=1). The ratio of these two terms was used to isolate the immobile fraction of cell images, denoted as $B=\sigma^2/<k>$. If the pixel had immobile and mobile components, B would be between 1 and the value obtained from the mobile fraction.

2.5.7. Adhesion Size Measurement

The adhesions containing dimers and higher order aggregates are found by comparing the confocal images with the corresponding brightness map. The area of those adhesions was acquired using the freehand selection tool in ImageJ to trace the individual adhesions from the confocal microscopy images used in the N&B analysis. The areas of these adhesions were determined using the ImageJ measure function.

2.5.8. Statistical Analysis

Statistical significance was determined for all migration and paxillin aggregation data using the Student's t-test (two-sample, unequal variance) in Excel.

2.6. Chapter 2 summary

We have shown that physical nanotopography can modulate the size of focal adhesions formed by the cells on the structures, which in turn affect their disassembly and migration. Cells on smaller nanopillars spaced 100-130 nm apart (P200 and P300, respectively) were more motile compared to cells on larger nanopillars, the nanoline grating reference, and the flat surface. These macroscale measurements of cell migrations did not, at first glance, support our hypothesis that more motile cells will give rise to an increased population of disassembling aggregates. However, when looking at the protein level of the adhesion protein with paxillin-GFP, these dynamics were found to correlate with the focal adhesion size found in NIH3T3 cells on each surface. Cells on nanopillars spaced 380 nm apart (P600) had the largest population of higher order paxillin aggregates and largest adhesions. This relationship of adhesion size and the population of aggregates decreased with decreasing pillar size. Similarly, cells on the P200 pillars had the smallest adhesions and the lowest population of aggregates. In addition, those with larger adhesion will require more time to completely disassemble for processes such as migration. Thus, NIH3T3 cells on P600 pillars had the smallest distance traveled over 12 hours of tracking, and cells on P200 pillars showed the greatest distance traveled for the same time frame. These results demonstrate that

migration and focal adhesion dynamics can be modulated with nanosized features of the substrate.

Cell-to-substrate interaction plays a significant role in cancer cell behavior. The architecture of collagen ECM consists of many fibrils from procollagen triple helixes which eventually yields a matrix consisting of many nanosized linear structures.[98,99] Thus, the matrix can be considered to have nanotopography itself. The findings in this chapter lay the groundwork for the later studies in the following chapter.

Chapter 3

3. Collagen stiffness modulates MDA-MB231 cell metabolism through adhesion-mediated contractility

3.1. Phasor representation of fluorescence lifetime imaging microscopy (FLIM)

Fluorescence microscopy has been an important tool for visualizing biological processes for research. The process of fluorescence begins when a molecule absorbs photons upon exposure to a specific wavelength of light. This causes the electrons in the molecule to reach a higher energy state, S1, as shown in **Figure 3.1**. These electrons will lose some of the absorbed energy due to vibrations and heat, energy state S2. Eventually, the absorbed energy would be released in the form of emitted photons and the elections would return to the ground state energy, G_0. These emitted photons are collected in the form of fluorescence. Due to energy loss, the emission is shifted towards a longer wavelength (i.e., lower energy) than that which is absorbed, this is known as the Stokes shift. This process can occur under 1-photon or 2-photon excitation. With 2-

photon excitation, a longer wavelength is used and thus two photons must be absorbed by a molecule to reach the excited state. It is advantageous to use 2-photon excitation when imaging live samples for extended periods of time to avoid photobleaching and phototoxicity, as could occur with 1-photon excitation.

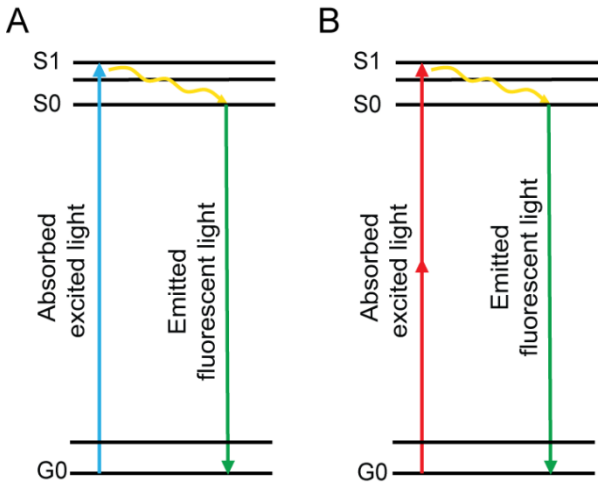

Figure 3.1: Jablonski diagram of (a) 1-photon and (b) 2-photon fluorescence

The amount of time it takes for an electron in the excited state to return to ground state energy G_0 can be measured and is termed the fluorescence lifetime. Although most calculations of the fluorescent lifetime is done by fitting the emission signal over time, the Laboratory for Fluorescence Dynamics (LFD) at UCI developed a fit-free method using a phasor representation of the data, as shown in **Figure 3.2**.[100] This is done by taking the Fourier transformation (**Equations 3.1-3.2**) of the emission signal which is shifted in phase (ϕ) and amplitude (E, excitation amplitude; F emission amplitude) from the excitation. S and G represent the in-phase and out of phase, respectively, of the

emission. Here, ω is the angular frequency of the excitation laser and M is the modulus. The transformation is done on every pixel in the image and the results are plotted on a phasor plot. The advantage of displaying the image in this manner allows pixel-level resolution in displaying the lifetimes, life-cell imaging, and isolation of subcellular compartments. In this thesis, I focus on gathering data of live-cell imaging during cancer invasion and migration to have a more accurate representation of the cell's behavior. NADH's chemical structure also gives it the capability to be used for autofluorescent imaging, thus transfection with foreign plasmids for fluorescent protein expression is not necessary. This serves as an advantage when looking at biological systems because there is no introduction of foreign proteins or agents to observe their behavior. Thus, the system that is studied is close to its endogenous form.

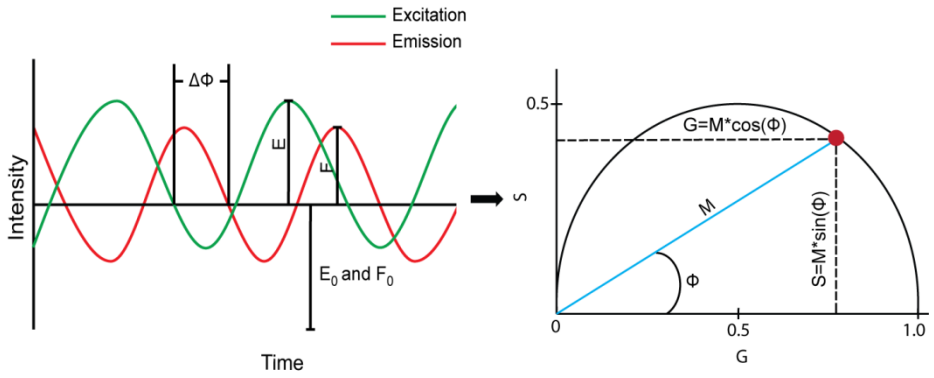

Figure 3.2: Fourier transformation in the frequency domain

$$S(\omega) = \frac{\int_0^\infty I(t)\sin(\omega t)\,dt}{\int_0^\infty I(t)dt} \qquad (3.1)$$

$$G(\omega) = \frac{\int_0^\infty I(t)\cos(\omega t)\,dt}{\int_0^\infty I(t)dt} \quad (3.2)$$

$$\phi = \tan^{-1}\left(\frac{S}{G}\right) \quad (3.3)$$

$$M = \sqrt{(G^2 + S^2)} \quad (3.4)$$

3.1.1. Applications of FLIM for metabolism and tension

Current methods of measuring metabolism changes within cells consist of biochemical assays and lack spatiotemporal resolution. FLIM has been a widely used tool to study the changes in metabolism by looking at the fluorescent lifetime of nicotinamide adenine dinucleotide, NADH.[101–105] NADH, a metabolite involved in OXPHOS and GLY, has been shown to have different lifetimes depending on when it is free in the cytosol or bound to an enzyme. When NADH is bound, it has a longer lifetime (~3.2 ns) compared to when it free (~0.4 ns).[101,106] Cells which will have an increased ratio of free:bound NADH are indicative of GLY and those with a lower ratio of free:bound NADH indicates a shift towards OXPHOS, for metabolism. Due to the nature of the phasor plot, we can draw a line between the two extremes of completely free and completely bound cases, creating a trajectory of metabolic indexes (M-trajectory), as shown in **Figure 3.3**. Within cells, there is always a mixture of free and bound NADH, thus, the phasor points of a sample will lie along this trajectory. In

addition, we are able to measure the fluorescent lifetime of live cell samples and quantify the metabolic index at every pixel.

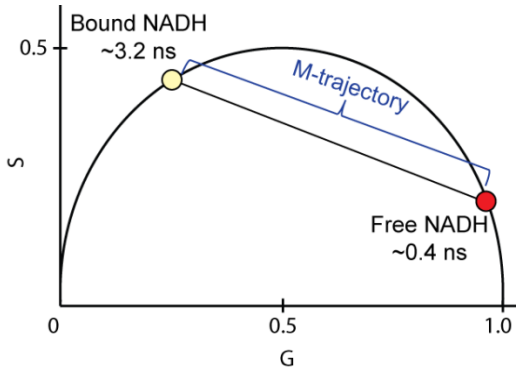

Figure 3.3 FLIM/Phasor for metabolism

3.2. Chapter 3 Abstract

Extracellular matrix (ECM) mechanical properties upregulate cancer invasion, cell contractility, and focal adhesion formation. In addition to matrix properties, alteration in energy metabolism is a known characteristic of cancer cells (i.e., Warburg effect) and modulates cell invasion. There is little evidence to show that collagen density is able to affect cancer cell metabolism. We investigated changes in energy metabolism due to collagen density in cancer and non-tumorigenic breast cell lines MDA-MB231 and MCF10A, respectively. By measuring the fluorescent lifetime of NADH, we are able to see shifts in metabolism when plated on varying collagen densities. We found that MDA-MB231 cells had an increased population of bound NADH, indicating an oxidative phosphorylation (OXPHOS) signature, as collagen

density decreased. When inhibiting ROCK and cell contractility with Y-27632 or blebbistatin, the MDA-MB231 cells on glass shifted from glycolysis (GLY) to OXPHOS, confirming the intricate relationship between mechanosensing and metabolism. MCF10A cells showed no changes in metabolism across all surfaces. In addition, OXPHOS or GLY inhibitors in MDA-MB231 cells showed dramatic shifts from OXPHOS to GLY or *vice versa*. There were slight changes detected in MCF10A cells. These results provide an important link between cellular metabolism, contractility, and collagen density in human breast cancer.

3.3. Introduction

Cancer cells can modulate their energy metabolism to meet nutritional, biosynthesis and respiration requirements for maintaining malignancy. One of these factors is the metabolic state of the cancer cell due to their tendency to undergo aerobic glycolysis, known as the Warburg Effect.[49,51,52] Although it produces less ATP per molecule of glucose, glycolysis (GLY) is a more rapid way of producing ATP and is able to meet the high demands of energy to fuel processes such as invasion, migration, and matrix degradation.[54,56,107,108] Along with high turnover of ATP production, a byproduct of lactic acid and high acidification also has been shown to benefit cancer cell survival and upregulate invasiveness.[109]

Mechanical properties of the extracellular matrix (ECM) is also a known factor that regulates cell migration and cancer invasion.[32,40,48,110,111] Cells interact with the surrounding ECM through integrin-mediated adhesions and focal adhesions (FAs), that are clusters of over 150 proteins.[8,21] These complexes tether to the cell's mechanosensing network through actin filaments and regulate processes such as adhesion, migration, and proliferation.[17,19,112,113] Recent studies have shown that integrin-mediated adhesion interact with the metabolic pathway of the cell through the PI3K/AKT/mTOR pathway and that this could be a potential method of switching the Warburg effect.[114–116] Many of these studies use biochemical assays which are invasive and often lose information which exists in live cell samples. In our approach, we used a non-invasive fluorescent imaging technique to measure ECM density, study live cell behavior, and map energy metabolism within each cell.

Fluorescent lifetime imaging microscopy (FLIM) has been shown to be a powerful technique to measure metabolic indices of live-cells.[101,102,104,105,117–119] By looking at the fluorescent lifetime of nicotinamide adenine dinucleotide (NADH), a metabolite involved in OXPHOS and GLY, we can determine the population of free and bound NADH due to their difference in lifetime decay. This will allow us to quantify the "metabolic trajectory", known as the "M trajectory", of the cell at every pixel of our image and determine if the cell is undergoing OXPHOS or GLY.[104] This trajectory has

also been shown to correlate with results found in conventional biochemical assays when OXPHOS or GLY inhibitors are used to shift metabolic towards one another.[104,119,120] The advantage of this imaging technique is that it is non-invasive and is able to image real-time changes in metabolism.

For this study, we measured free and bound populations of NADH within different cancer cell lines and a non-tumorigenic cell line when seeded on collagen substrates of different concentrations (1.2 mg/mL and 3.0 mg/mL) and on glass. The microstructural properties of this substrate, including collagen density and fiber diameter, were measured using image correlation spectroscopy.[121] The 3.0 mg/mL and 1.2 mg/mL collagen substrate had collagen fibers of similar size, but the 3.0 mg/mL collagen substrate gave rise to a denser ECM than the 1.0 mg/mL substrate by 3X. The 3.0 mg/mL collagen substrate was also determined by rheology to be one order of magnitude stiffer than the 1.2 mg/mL collagen substrate. In this paper, we will refer to the density of the collagen as our means to distinguish the difference between the two ECM substrates. We are also aware that each cell line requires different media conditions for culturing and these affect the metabolism. However, we are interested in the effects of collagen density on each cell line independently. The highly metastatic breast cancer cell line MDA-MB21 showed a shift towards a more glycolytic signature as collagen density increased. Inhibition of cell contractility with the addition of Y-27632

shifted all the cells on all substrates to a more OXPHOS signature compared to their uninhibited controls. This further shows that integrin-mediated adhesions behave as mechanosensors and these adhesions can alter metabolism.

Non-tumorigenic breast cell line MCF10A showed no significant changes in NADH free:bound ratio across all surfaces, indicating that this property only appears in MDA-MB231 cell lines. Other cancer cell types, U251MG glioma and A375MM melanoma cell lines, were evaluated under the same conditions. The U251MG cells had an opposite trend of NADH free:bound ratio signatures across the substrates compared to MDA-MB231 cells. A375MM cells did not adhere well to the collagen substrates which caused them to have no significant difference in their NADH free:bound ratio; which indicates that the mechanosensing network must be established in order to undergo metabolic reprogramming. Inhibition of OXPHOS or GLY in MDA-MB231 cells showed shifts in NADH free:bound ratio with respect to each treatment towards their metabolic counterparts across all surfaces, and further confirmed that it is indeed the metabolism that is being altered by the ECM. MCF10A cells showed a shift when OXPHOS was inhibited only on our denser collagen substrate and on glass when GLY was inhibited. The results found in our work here show that both the mechanosensing and metabolism pathways are interconnected and can be modulated through ECM

mechanical properties. This will provide further information to develop cancer therapies which target either or both of these pathways to decrease cancer cell invasion.

3.4. Results

3.4.1. Collagen characterization measurements

Tilghman *et al.* postulated that cellular metabolism can be altered when MDA-MB231 cells are cultured on soft (300 Pa) versus stiff (19200 Pa) matrices due to the fact that cells stayed in the G1 phase of the cell cycle longer.[122] Indeed, their results using cell lysates with ATPlite assay and protein synthesis assays confirmed their hypothesis. The substrates used in those experiments were limited to polyacrylamide gels that have a large rigidity/flexibility range, but it is not physiologically relevant. In our approach, we used collagen monolayers prepared at two different concentrations of 1.2 mg/mL and 3.0 mg/mL Second harmonic generation (SHG) images were taken to measure the fiber thickness, and density was measured using image correlation spectroscopy (ICS). Previously in our lab, we have shown that fiber and pore size of collagen matrices obtained through SHG and ICS correlated to those obtained by rheology or scanning electron microscopy images.[121,123] For this analysis, auto-correlation function, G(0), is calculated with **Equation 3.5** in the **Materials and Methods** for this chapter. The waist of G(0), ω_o, can also be measured based on the size of the point spread function of the

laser (~0.3 μm at the waist). A larger ω_o value represents thicker collagen fibers. 1/G(0) quantifies the density of the matrix which is the height of the auto-correlation function extrapolated from the first measured point. A smaller 1/G(0) value corresponds to denser matrices. Our substrates of 3.0 mg/mL and 1.2 mg/mL collagen showed similar average values of ω_o of 2.55 and 2.29 (**Figure 3.4c**). However, the 3.0 mg/mL collagen had a significantly larger average value of 1/G(0) of 5.54 compared to that of 1.2 mg/mL at 1.09 (**Figure 3.4d**). This confirmed that the 3.0 mg/mL collagen substrates had a denser network of collagen although their fiber thicknesses are similar. Rheology measurements were also done to quantify the modulus of the substrates. 3.0 mg/mL and 1.2 mg/mL collagen substrates were measured and have averages of 38.12 Pa and 5.66 Pa, respectively (**Figure 3.4b**), showing that the 3.0 mg/mL collagen substrates are about stiffer than the 1.2 mg/mL substrate.

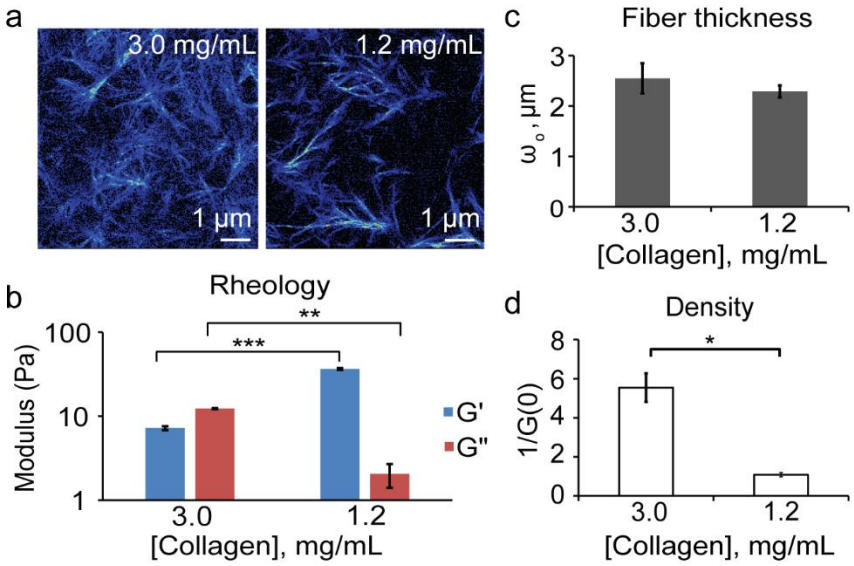

Figure 3.4 Quantification of collagen substrates. (a) Second harmonic generation images of 3.0 mg/mL and 1.2 mg/mL collagen substrates. (b) Modulus of collagen substrates at 10% strain and 1Hz (c) Quantification of fiber size (ω_o) and (d) density of collagen substrates. * p<1e-3, ** p<1e-26, *** p<1e-57. Error bars represent S.E.M.

3.4.2. MDA-MB231 cells shifts towards glycolytic signatures on stiffer collagen substrates

By measuring NADH fluorescent lifetimes with FLIM, we were able to non-invasively determine spatial shifts in the metabolism of different cell lines in response to collagen density. NADH has two different lifetimes when it is free in the cytosol, ~0.4 ns, or bound to a protein, ranging from ~1.4 ns to 9 ns.[106,124,125] Thus, we are able to distinguish the ratio of free and bound NADH at each pixel. For our studies, the lifetime of NADH bound to lactate dehydrogenase (LDH, ~3.4 ns) is used when

quantifying the population of bound NADH, although there are many other possible enzymes.[101,102] The lifetime decay measured is Fourier transformed and displays a graphical representation of fluorescence lifetime on the phasor plot where all single exponential decay lifetimes are plotted on the semi-circle (called the universal circle) and all multi-exponential lifetimes are inside the semicircle representing the sum of linear combinations of single-exponential lifetimes. **Figure 3.5a** depicts the fluorescence lifetime (0.4 ns) of free NADH and 100% bound (3.4 ns) NADH to LDH. If the binding is not complete, we can calculate the ratio of bound to free NADH from the pure free and bound linear combination of lifetimes. In our control, the population of percentage bound to NADH was 75%. This linear trajectory is indicative of GLY and OXPHOS state in live cells.[100,104]

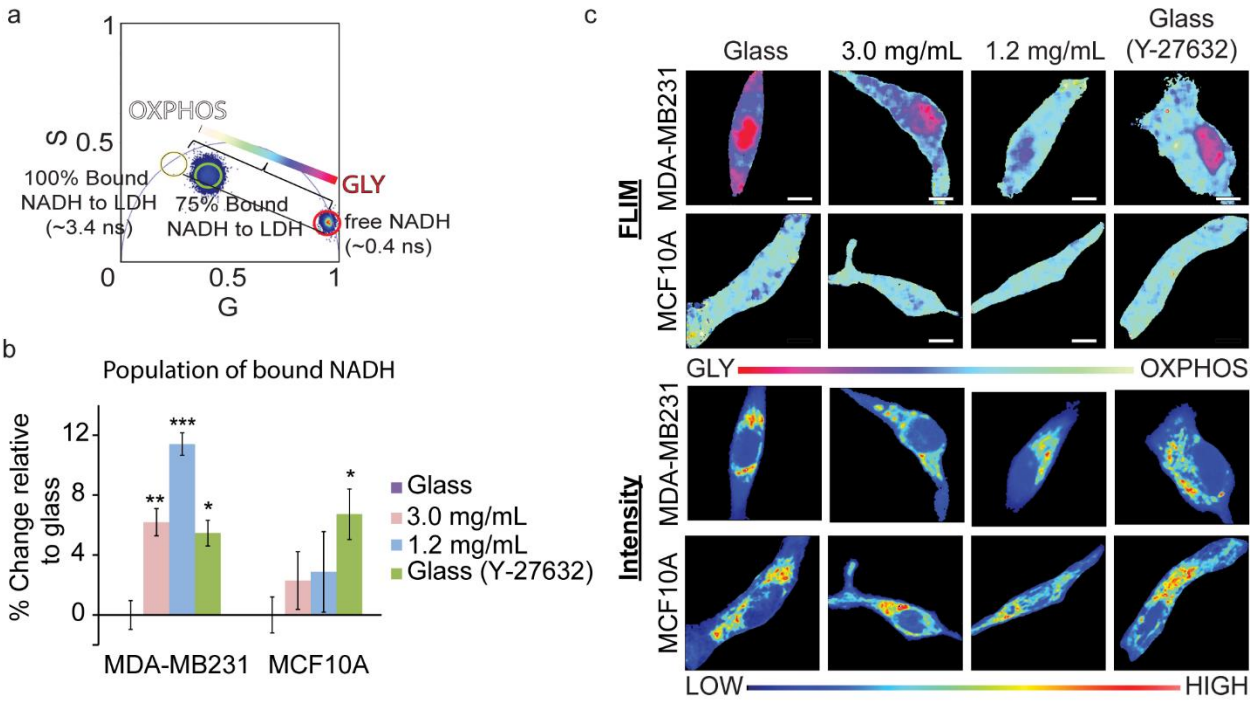

Figure 3.5: Metabolic indexes of MDA-MB231 and MCF10A cells on various collagen densities. (a) An increased population of bound NADH to LDH (long lifetime NADH, cyan) is indicative of a more OXPHOS signature while an increased population of free NADH (short lifetime NADH, red) would indicate GLY. These two extremes create a linear "M-trajectory" where a mixed population of bound and free NADH, for example 75%, will lie between these two points. (b) Percent increase of bound NADH in MDA-MB231 and MCF10A cells relative to glass. (c) Colored images of FLIM of NADH and the average intensity of NADH within MDA-MB231 and MCF10A cells. *p<0.05, **p<0.01, and ***p<1e-5 by Student's t-test. Error bars represent S.E.M. Scale bar: 5 μm

Highly invasive MDA-MB231 cells were seeded on collagen and glass substrates to observe changes in free:bound ratios of NADH. In addition, the free:bound ratio of NADH in non-tumorigenic breast cells MCF10A were used as a control for a non-tumorigenic cell line. MDA-MB231 cells showed a 6.2% and 11.4% increase of bound NADH on 3.0 mg/mL and 1.2 mg/mL substrates, respectively, relative to those on glass (**Figure 3.5b**). This indicates that as collagen density increased, the MDA-MB231 cells shifted from OXPHOS (white/cyan) to GLY (pink/red) (**Figure 3.5c**). MDA-MB231 cells on glass were then treated with 10 μM Y-27632, a ROCK inhibitor that decreases cell contractility, to assess if inhibiting the cell's mechanosensing ability would shift the metabolism towards OXPHOS. Indeed, we see a significant change in the metabolic index (5.7% increase in bound NADH) in these cells when Y-27632 was added (**Figure 3.5b**). Similar results were seen on MDA-MB231 cells on glass when treated with 3.5 μM blebbistatin, showing a 14.4% increase relative to untreated glass samples (Error!

eference source not found.). We also used both treatments on MDA-MB231 cells plated on 1.2 mg/mL and 3.0 mg/mL collagen and detected an increase in the bound NADH population as well (Error! Reference source not found.). MCF-10A cells did not show this shift in metabolism in response to collagen density but did show an increase in the population of bound NADH with the addition of Y-27632 on glass (**Figure 3.5b&c**)**.** We also examined other cancer cell lines to determine if they also had the same response to collagen density.

Melanoma, A375MM, and glioblastoma, U251MG, cell lines showed different results than that of the MDA-MB231 cells. A375MM cells showed no significant change in the free:bound ratio of NADH when on the 1.2 mg/mL or 3.0 mg/mL collagen substrates or glass (**Figure 3.6a&b**). We noticed that these cells did not adhere as well on the collagen substrates due to their round morphology (**Figure 3.6c**) which could be the reason why there was no change in metabolism as seen in the MDA-MB231 cells. This further supports our hypothesis that the mechanosensing pathway plays an important role in cancer cell metabolism. On the other hand, the U251MG cells showed opposite changes to that of MDA-MB231 cells with 3.4% and 1.6% decrease in bound NADH relative to glass for those on 3.0 mg/mL and 1.2 mg/mL collagen, respectively (**Figure 3.6b**). Thus, they showed increased glycolytic signatures as collagen density decreased, although the changes were not significant. Previous studies have also shown

that MDA-MB231 and U251MG have opposite trends of matrix degradation and invadopodia formation when they are cultured in different media supplemented with GLY or OXPHOS inhibitors.[50] This may explain our results, but further studies will need to be conducted to confirm them.

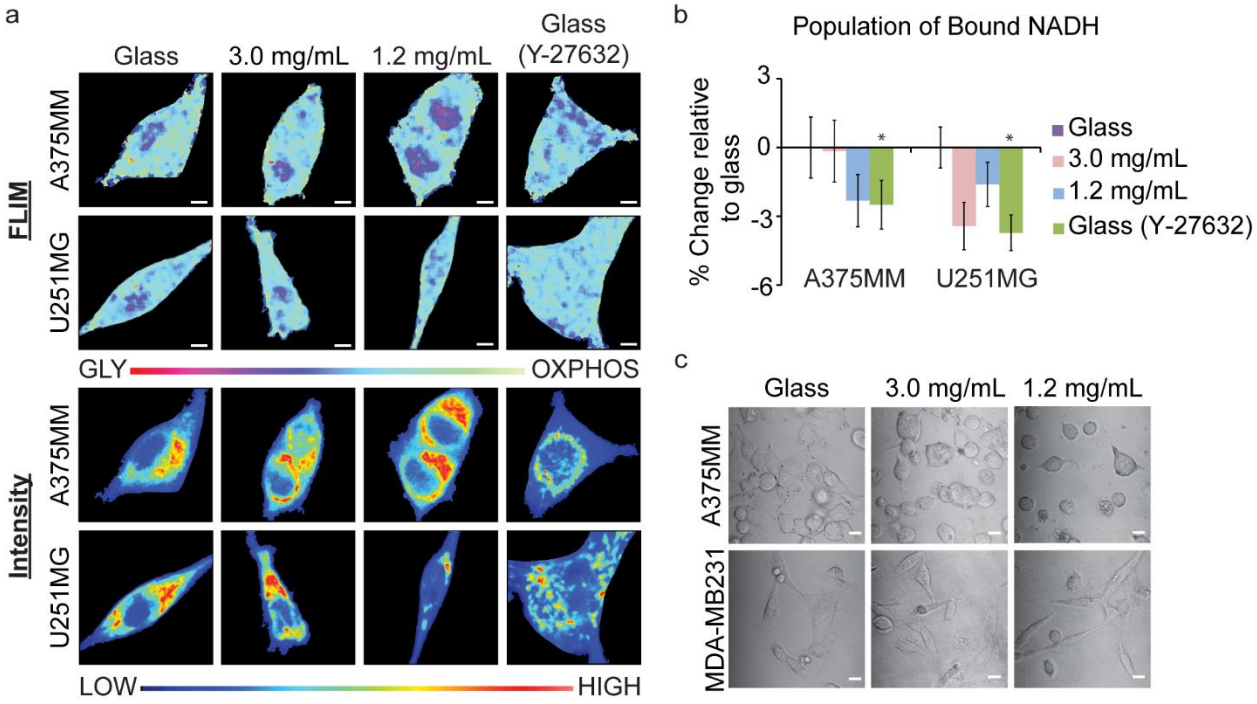

Figure 3.6: Metabolic indexes of A375MM and U251MG cells on various collage densities. (A) FLIM and average intensity images of NADH within A375MM melanoma and U251MG glioma cell lines. (B) Quantification of the percent change of NADH within A375MM and U251MG cell lines on various substrates relative to those on glass. (C) Transmitted optical images of A375MM and MDA-MB231 cells on different substrates. *p<0.05, by Student's t-test. Error bars represent S.E.M. Scale bar: 5 μm

We isolated the metabolic phasor signature of the nucleus and the cytoplasm and compare them here across all surfaces in each cell line (Error! Reference source not

ound.). Generally, the nucleus of the cell lines has a more GLY signature than the cytoplasm, but this did not significantly affect the results we found when looking at the entire cell within MDA-MB231 and MCF10A cells. However, within A375MM cells seeded on 3.0 mg/mL or 1.2 mg/mL collagen substrates, their populations of bound NADH were similar; but when looking at their nuclei and cytoplasmic, we began to see a separation between the two conditions, especially in the nuclei alone. The nuclei in A375MM cells on 3.0 mg/mL collagen substrates show a shift towards GLY where their population of bound NADH decreased by 24.5% compared to those on glass. U251MG cell nuclei metabolic indices were similar on all surfaces except for those on glass and treated with blebbistatin, which showed a 10.6 decrease in the population of bound NADH.

The rest of this report will focus mainly on the MDA-MB231 and MCF10A cells to compare results of cancerous and non-tumorigenic cell lines. In order to confirm that the fraction of free:bound ratio of NADH is modulated through collagen density, we conducted metabolism inhibition studies of each cell line when seeded on both collagen and glass substrates.

3.4.3. Metabolism inhibition studies confirm that GLY and OXPHOS are modulated by substrate stiffness

In order to ensure that the collagen density alters metabolism in MDA-MB231 and MCF10A cells and that these changes correlate with lifetime positions along the M trajectory, we treated these cell lines with oxidative phosphorylation and glycolysis inhibitors. We treated MDA-MB231 cells with 50 mM 2-deoxyglucose and 100 mM dichloroacetate (2DG&DCA) for GLY inhibition and 50 nM rotenone and 50 nM antimycin A (R&A) for OXPHOS (**Figure 3.7**). These inhibitors are known used to shift the metabolic signatures towards OXPHOS or GLY.[119,120,126,127]

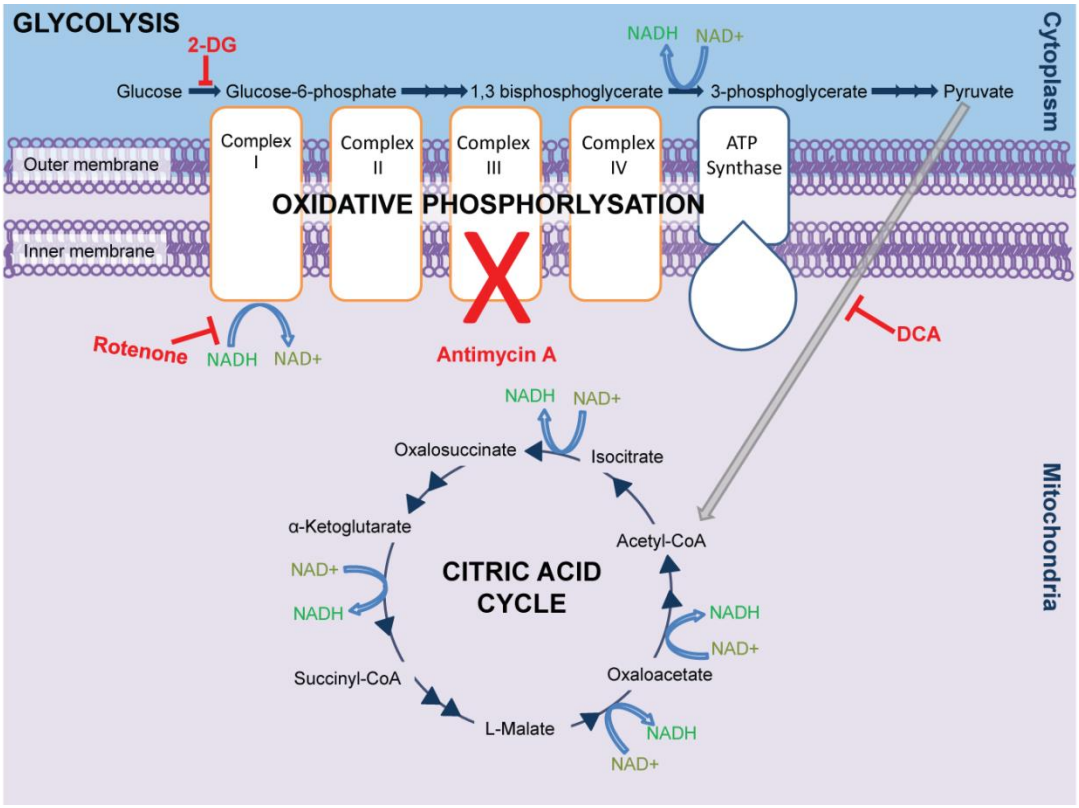

Figure 3.7: Metabolism inhibition for OXPHOS and GLY

2DG&DCA treatment showed an increased population of bound NADH of 25.43%, 16.01% and 12.98% for cells plated on glass, 3.0 mg/mL collagen, and 1.2 mg/mL collagen surfaces, respectively, relative to untreated cells (**Figure 3.8c**). When MDA-MB231 cells were treated with R&A on 3.0 mg/mL and 1.2 mg/mL collagen substrates, they showed significant decreases in the population of bound NADH, $p<0.05$, of 11.5% and 11.35%, respectively, relative to untreated cells. However, there was no change when these cells plated on glass were inhibited with R&A. These treatments were also applied to MCF10A cells where we observed a significant decrease in the population of

bound NADH only on 3.0 mg/mL collagen substrates, 5.52%, and glass, 5.93%, when treated with R&A (**Figure 3.8d**). No changes were seen on the 1.2 mg/mL collagen substrates. However, there was a significant increase of 3.32% on these cells when plated on 1.2 mg/mL collagen and treated with 2DG and DCA.

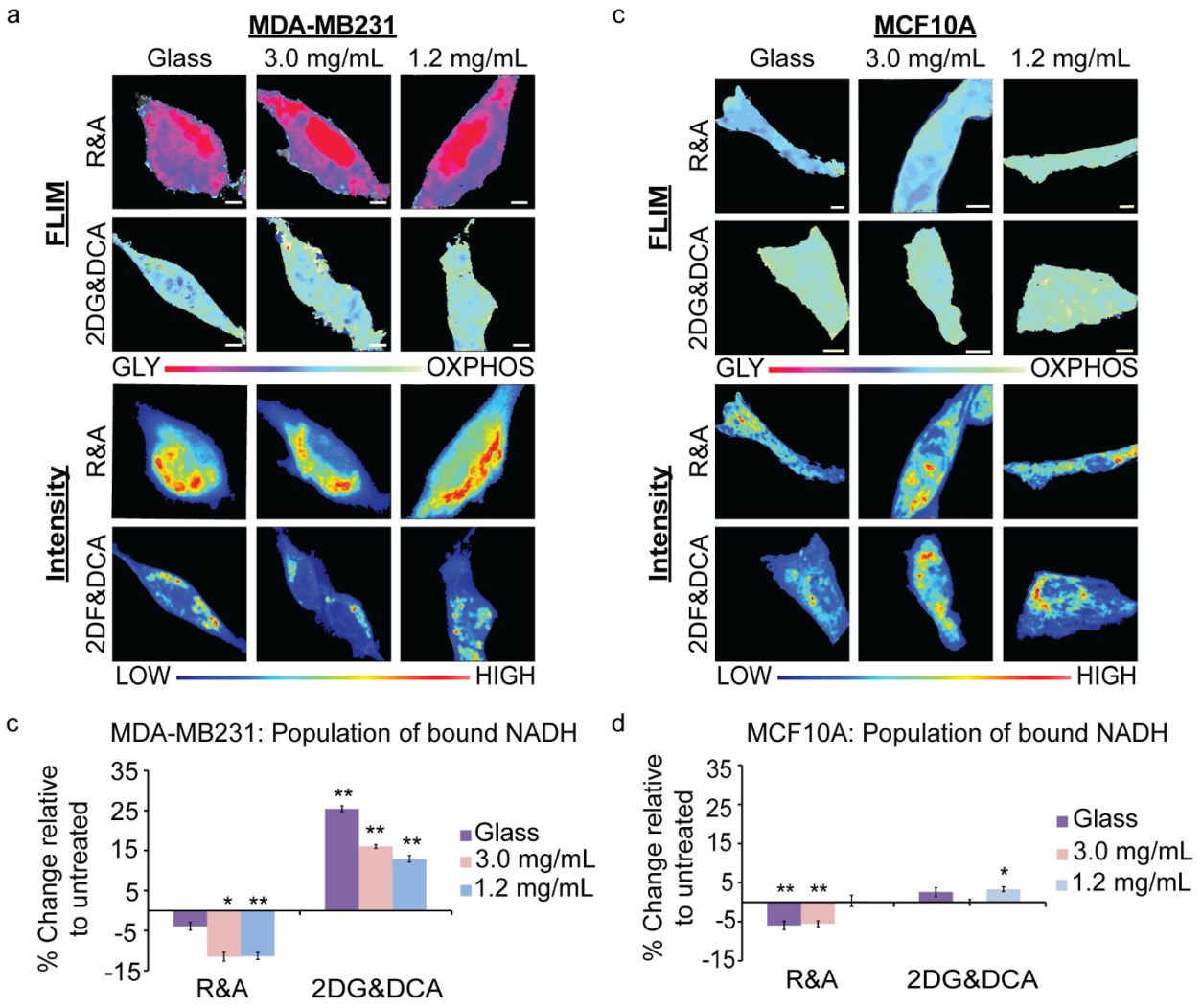

Figure 3.8: MDA-MB231 and MCF10A metabolic indexes when treated with metabolic inhibitors. (a) MDA-MB231 and (b) MCF10A cells treated with rotenone and antimycin A (R&A) or 2-deoxyglucose and dichloroacetate (2DG&DCA) for OXPHOS or GLY inhibition, respectively. FLIM images show the shifts

of metabolic indexes with respective intensity images below. (c) Quantification of the change of bound NADH in MDA-MB231 and (d) MCF10A cells relative to untreated cells. *p<1e-3, **p<1e-4 or less by Student's t-test. Error bars represent S.E.M. Scale bar: 5 μm

3.5. Discussion

The Warburg effect is the hallmark of cancer cell metabolism, described as an oncogene-directed glycolytic state even when oxygen is present.[49,52,128] This could be due to the high turnover of ATP production through glycolysis for energy production with glucose, although the alternative process of oxidative phosphorylation creates more product of energy per glucose molecule. Cancer cell invasion has also been shown to be modulated by changes in metabolism through changing cell media additives for energy consumption[50,53] or the ECM stiffness and density.[32,36,41,110,129] However, the link between ECM stiffness or density and cell metabolic state (OXPHOS or GLY) is not clear. Recent studies that look at alterations of metabolism use invasive biochemical assays that do not report the spatial heterogeneous changes of metabolic response within cellular compartments, nor their cellular metabolic state. Our study used FLIM of NADH to measure real-time metabolic indexes of different cancer cell types in response to collagen density. This allows us to characterize which metabolic process occurs with pixel resolution in live cells. It is important to note that since different additives change cellular metabolism, our culture conditions for our cells remained the same through the

study. Each cell line required different culturing conditions independently, but their media used was the same when measurements were taken. Thus, we are able to observe their respective metabolism changes in response to collagen density.

We have found that MDA-MB231 cells on substrates on two different collagen densities have an increasing population of free NADH, showing a more glycolytic signature of metabolism. This correlates with previous studies in that breast cancer cells have increased migration and aggressiveness within denser collagen matrices.[32,42,116] In addition, cancer cells undergo aerobic glycolysis for energy production, thus increased collagen density could be a contributor to the metabolic shift towards glycolysis.[52,126] The ECM plays a key role in the cancer cell's mechanosensing pathway through integrin signaling, and there is increasing evidence that this regulates cell migration and matrix degradation.[40,43,50,123] Increased ECM stiffness and density signals actin polymerization, increased integrin signaling, and stabilization of the focal adhesion complexes.[17,19,130] This increase of integrin signaling has been shown to also upregulate the PI3K/AKT/mTOR pathways and possible metabolism switching in cancer cells.[107,114,115,131] In addition, stimulating the actin-contractility of cells through external forces by shear flow or pulling of the cell membrane increases glucose uptake.[132,133] Bays *et al.* has shown that this increased glucose uptake was also shown to increase ATP production for actin polymerization and stabilize E-cadherin contacts.[132] Our results

expanded on these studies by looking at the specific metabolic indexes of cancer cells when introduced to various collagen density. We speculate that these same pathways are being activated in the MDA-MB231 cells and are stimulated passively through focal adhesion-mediated interactions with the ECM.

When cells grown on glass substrates were treated with Y-27632 or blebbistatin, we inhibited their ability to undergo contraction through myosin-II and caused focal adhesion detachment from the substrate.[134] This, in turn, showed shifts in metabolic indexes from GLY to OXPHOS in MDA-MB231 and MCF10A cells. This confirms that it is through actin-mediated cell contractility that modulated these shifts in metabolism. Interestingly, the MDA-MB231 cells treated with Y-27632 had a similar NADH free: bound ratio as those grown on 3.0 mg/mL, which could mean that their degrees of contractility were similar to each the respective conditions. Those treated with blebbistatin had a much larger shift towards OXPHOS, surpassing the population of bound NADH of cells grown on 1.2 mg/mL collagen. Since blebbistatin directly affects myosin-II and is more potent than Y-27632, this was as expected. Previous studies have shown that stable adhesions have a developed mechanosensing network of actin, and these adhesions can grow in response to forces or increasing substrates stiffness.[16,18,71,111] Thus, cells on the denser substrates should have the most stable adhesions. In turn, they

would also have increased FAK which promotes glucose consumption and plays a key role in the OXPHOS and GLY balance within cancer cells.[135]

The human melanoma cell lines, A375MM, in this study attached to 1.2 mg/mL and 3.0 mg/mL collagen substrates but did not spread as well as all other cells. This was an indication that their adhesions are not stable or favorable on these substrates [136–138] and their mechanosensing ability could have been compromised, resulting in reduced mitochondria activity.[139] Consequently, this would fail to change the metabolic indexes of these cells as shown in our results, where the NADH free: bound of A375MM on 1.2 mg/mL or 3.0 mg/mL have no significant difference. This phenotype showed that there is a confirmed link between focal adhesion-mediated mechanosensing and cellular metabolism

We also measured the NADH free:bound ratio in glioblastoma cells, U251MG, to see if these trends existed in other cancer cell lines. It was found that they had an opposite trend than that of the MDA-MB231 cells. Although these findings were not significant, we can see a gradual shift towards an OXPHOS metabolic index, or an increase in bound NADH, as collagen density decreased. Studies done by Van Horssen *et. al* also showed that MDA-MB231 and U251MG cells had opposite trends in matrix degradation and invadopodia formation when their metabolism is altered either by galactose containing media to inhibit GLY or addition of oligomycin to inhibit

OXPHOS.[50] It is important to note that there are many other possible uses for pyruvate aside from OXPHOS in the mitochondria. Downstream of GLY are intermediates of the tricarboxylic acid cycle, such as citrate, which allows for the synthesis of lipids, proteins and nucleic acids, a demand for highly proliferating cells.[140] There is also fatty acid synthesis through citrate which is shown to correlate with the formation of invadopodia, which are actin-rich protrusions used for matrix invasion.[53,126,129] In addition, the pentose phosphate pathway could further increase the GLY and fraction of free NADH. All of the pathways mentioned could be elevated within MDA-MB231 cells, which could contribute to their difference in metabolic trends from the U251MG cells when collagen density is varied.

The MB231 cells have a significant decrease in the fraction of bound NADH when plated on glass, 3.0 mg/mL and 1.2 mg/mL collagen, respectively. We confirmed that the changes in metabolic trajectory were reflective in cellular metabolism using the OXPHOS and GLY inhibitors. When these inhibitors were added, cells shifted their metabolism accordingly to their inhibitors but there were no significant metabolic differences across collagen densities within these changes (Error! Reference source not ound.**a**). However, the MCF10A cell lines did not show any changes in metabolic indexes across substrate densities in their untreated conditions. They did show substrate sensitivity only when OXPHOS was inhibited. When R&A was added to

inhibit OXPHOS to the 3.0 mg/mL and glass substrates in MCF10A cells, there was a maximum decrease to around 64% of the population of bound NADH; however, those on 1.2 mg/mL collagen showed no significant change (Error! Reference source not ound.**b**). This could mean that on denser collagen substrates, these cells were more susceptible to metabolic changes when introduced to inhibitors. Additionally, this could also indicate that the metabolism of the MCF10A cells was behaving more like the MDA-MB231 cells on the denser matrices. When 2DG&DCA was added to inhibit GLY in MCF10A cells, we see a significant increase in the population of bound NADH to around 71.2% when grown on 1.2 mg/mL collagen substrate. Since OXPHOS and an environment with less collagen is preferable to the MCF10A cells, this could mean that this ECM provides an extra boost towards OXPHOS pathway when GLY is inhibited.

The phasor approach to FLIM of NADH allows isolation of the metabolic signature within sub-cellular compartments of the cells. Here, we focused on comparing the nuclei and cytoplasm of MDA-MB231, MCF10A, A375MM, and U251MG cell lines (Error! Reference source not found.). We were able to see that the metabolic shifts ithin the nuclei and cytoplasm of MDA-MB231 and MCF10A cells are similar to their whole cell signature. However, within A375MM cells we were able to make distinctions of the population of bound NADH between surfaces, which were not detected when averaging over the entire cell. The nuclei of A375MM cells on 3.0 mg/mL collagen

substrates has a significant decrease in the population of bound NADH with respect to those on glass. Thus, looking at the nuclear metabolic indexes can separate subtle changes that are hidden in whole cell readings. These distinctions seen could be due to nuclear processes, such as transcription or DNA repair, which has also been shown to affect the ratio of bound and free NADH.[103,141]

3.6. Materials and Methods

3.6.1. Cell culturing and transfections

MDA-MB231 and A375MM cells were cultured in Dulbecco's Modified Eagle's Medium (DMEM) with high glucose, L-glutamate, and sodium pyruvate (Genesee Scientific, San Diego, CA) supplemented with 10% heat-inactivated Fetal Bovine Serum (Thermofisher Scientific, USA) and 1% Penicillin-Streptomycin 100X Solution (Genesee Scientific, San Diego, CA). U251MG cells were cultured in DMEM/F12 with also with high glucose, sodium pyruvate and L-glutamine (Thermofisher Scientific, USA) supplemented with 10% heat-inactivated Fetal Bovine Serum (Thermofisher Scientific, USA) and 1% Penicillin-Streptomycin 100X Solution (Genesee Scientific, San Diego, CA). MCF10A cells were also cultured in DMEM/F12 with high glucose, sodium pyruvate and L-glutamine (Thermofisher Scientific, USA) supplemented with 5% horse serum (Thermofisher Scientific, USA), 20 ng/mL epidermal growth factor, 0.5 mg/mL

Hydrocortisone (Sigma-Aldrich, St. Louis, MO), 100 ng/mL cholera toxin (Sigma-Aldrich, St. Louis, MO), 10 μg/mL insulin (Sigma-Aldrich, St. Louis, MO), and 1% Penicillin-Streptomycin 100X Solution (Genesee Scientific, San Diego, CA). All cell lines were incubated at 37°C, 5% CO_2.

When cell lines which required transfections of talin-GFP (Addgene, Cambridge, MA) were seeded in a 6-well plate at $0.25x10^6$ cells/well overnight at 37°C, 5% CO_2. Lipofectamine 3000 (Thermofisher Scientific, USA) was used for transfections following manufacturer protocol. Briefly, 100 μL of Opti-mem (Thermofisher Scientific, USA) and 5 μL of Lipofectamine 3000 were mixed in a microcentrifuge tube. In a second microcentrifuge tube, 100 μL of Opti-mem, 1 μg of DNA plasmid, and 2 μL/μg of P3000 reagent were mixed together. Both tubes were allowed to sit for 5 minutes at room temperature and then combined. After the transfection mixture was allowed to sit for 25 minutes at room temperature, it was added dropwise to the cells.

3.6.2. Collagen substrate monolayers

Substrates were made on 35 mm glass bottom imaging dishes which were treated for 5 minutes with UV-ozone. 1% v/v of 3-aminopropyltriethoxysilane (APTES) in deionized water were added and allowed to sit for 25 minutes at room temperature. The dishes were washed thoroughly with deionized water and brought to the biosafety

hood for sterile handling. 1 mL of sterilized MilliQ water used to rinse the dish before collagen was added.

For collagen preparation, microcentrifuge tubes and reagents used were kept on ice for as long as possible while handling. Collagen I from rat tail (Corning, Corning, NY) was diluted with deionized water such that the final concentration was either 1.2 mg/mL or 3.0 mg/mL. 100 μL of 10X phosphate buffer saline (Thermofisher Scientific, USA) containing phenol red was added dropwise while vortexing as a pH indicator. 0.5 N NaOH was then added dropwise to the mixture with periodic vortexing until the solution became a slight pink (pH~7). The collagen was then added to the treated imaging dish (total volume of 1 mL) and incubated at 20°C for 1 hour and then at 37°C, 5% CO_2 overnight. $0.25x10^6$ cells were then added to each dish the next day and then allowed to incubate at 37°C, 5% CO_2 overnight again before imaging took place.

3.6.3. Inhibition studies

Contractility inhibition was done with Y-27632 (Selleckchem, US) or blebbistatin (Sigma-Aldrich, St. Louis, MO) at a working concentration of 10 μM and 3.5 μM, respectively. Each inhibitor was incubated for 10 minutes at room temperature before conducting FLIM/NADH imaging. MDA-MB231 or MCF10A cells were treated with sodium dichloroacetate (Sigma-Aldrich, St. Louis, MO) and 2-deoxyglucose (Sigma-Aldrich, St. Louis, MO) at a working concentration of 100 mM and 50 mM, respectively,

for 6 hours at 37°C, 5% CO_2 to inhibit glycolysis.[119] Similarly, cells were treated for 10 minutes with 50 nM rotenone and 50 nM antimycin A at 37°C, for oxidative phosphorylation inhibition studies before NADH lifetimes were measured.

3.6.4. Characterization of collagen substrates

Rheology measurements of collagen substrates were conducted to obtain the storage (G') and loss (G") moduli. The collagen substrates were pre-made on 15 mm glass slides that were treated with UVO and APTES as described above. Collagen solutions of 1.2 mg/mL or 3.0 mg/mL were carefully pipetted onto the round glass slides and allowed to incubate at 20°C for 1 hour and then at 37°C overnight for 2 nights to mimic culturing conditions for imaging. The glass slides were placed on the stage of the AR-G2 rheometer (TA Instruments, New Castle, DE) that was kept at a constant temperature of 37°C. A sand-blasted parallel plate geometry with a diameter of 25 mm was lowered to a gap distance of 0.3 mm so that it was in close contact with the surface of the collagen. Rheology measurements were conducted at a constant sinusoidal frequency of 1 Hz and 10% peak-to-peak strain and outputs of G' and G" were recorded for a total of 10 minutes. A data point was taken every 60 seconds.

Second harmonic generation imaging of collagen substrates was conducted to characterize substrate density as previously.[123,142] Briefly, 2-photon excitation at 900 nm was used to generate second harmonics of collagen and collected with a bandpass filter

at 460/80 nm with external photon-multiplier tubes (H7422P-40, Hamamatsu, Japan) and FastFLIM FLIMBox (ISS, Champaign, IL). 100 frames were collected and analyzed using image correlation spectroscopy on SimFCS (LFD, UCI). Spatial correlations were applied to each pixel at coordinate (x, y) of the complied SHG images with **Equation 3.5**:

$$G_s(\xi, \varphi) = \frac{<I(x,y)I(x+\xi,y+\varphi>_{x,y}}{<I(x,y)>^2_{x,y}} - 1, \quad (3.5)$$

where I is the intensity. ξ and φ are the spatial shifts in the x and y directions, respectively.

3.6.5. Confocal and fluorescent lifetime imaging acquisition and analysis

FLIM images for MDA-MB231, U251MG, and A375MM cells were imaged on the Zeiss LSM 710 (Carl Zeiss, Jena, Germany), LSM 880 (Carl Zeiss, Jena, Germany), and Olympus Fluoview respectively. MCF10A cells were also imaged on the LSM710. Metabolism inhibition studies of MDA-MB231 and MCF10A cells were imaged on the Olympus Fluoview. Images (256x256 pixel size) were taken at a pixel dwell time of 25.21 μs, 16.38 μs, and 20 μs for the LSM710, LSM880, and Fluoview, respectively. All microscope systems were coupled to with a two-photon Ti: Sapphire laser (Spectra-Physics MaiTai, Mountain View, CA) for NADH excitation at 740 nm with an Olympus

40X/0.8 NA water objective. The emission was separated at 690 nm in all systems followed by two bandpass filter at 460/80 nm and 540/50 nm with a with a dichroic mirror 495 nm long-pass filter. The signal was collected with an external photomultiplier tube (H7422P-40, Hamamatsu, Japan). A320 FastFLIM FLIMbox (ISS, Champaign, IL) was used to acquire the frequency domain of the lifetime of NADH until enough statistics were obtained. Images of coumarin-6 in ethanol were also taken as reference and calibration for FLIM measures across all microscopes.

SimFCS (LFD, UCI) was used to analyze the fluorescent lifetime of NADH at every pixel. The lifetime decay at each pixel was Fourier transformed and plotted on a phasor plot as previously described where each point on the phasor represents one pixel.[100] Each cell's cluster of phasor points were averaged to obtain their S, G, and fraction bound value. Calculations for S and G for the in-phase and out-of-phase signals are shown in **Equations 3.6** and **3.7** respectively. I is the intensity of the pixel at point (x,y) and ω is the angular frequency of the light modulation. Average phasor plots of the data are shown in **Error! Reference source not found.**.

$$S_{x,y} = \frac{\int_0^\infty I_{x,y}(t)\sin(\omega t)dt}{\int_0^\infty I_{x,y}(z)\,dt} \tag{3.6}$$

$$G_{x,y} = \frac{\int_0^\infty I_{x,y}(t)\cos(\omega t)dt}{\int_0^\infty I_{x,y}(t)\,dt} \tag{3.7}$$

The fraction of bound NADH is calculated based on the fact that any two points on the phasor plot (e.g. 100% free NADH and 100% bound NADH to LDH) can be connected by a line and any points along that line will be a linear representation of the two extremes. Thus, the experimental data will exist between 100% free NADH and 100% bound NADH, signifying samples that have a mixture of free and bound NADH. Those points that are closer to the phasor of bound NADH to LDH will have a higher population of bound NADH.

3.6.6. Statistical analysis

Statistical significance was determined for experiments with the Student's t-test (two-sample, unequal variance) in Microsoft Excel

3.7. Chapter 3 Summary

We have shown that focal adhesion-mediated contractility modulates cell metabolism in MDA-MB231 cancer cells. With the use of FLIM of NADH, we were able to non-invasively measure metabolic changes of cancer cell lines MDA-MB231, A375M and U251MG and within non- tumorigenic line MCF10A. Particularly in breast cancer MDA-MB231 cell lines, we saw that stiffer substrates shifted cells to have a more glycolytic metabolic signature due to their increased population of free NADH. However in non- tumorigenic breast cells MCF10A, we did not see any changes in

metabolism across all substrates. Further studies by inhibiting myosin-II contractility increased the population of bound NADH MDA-MB231 cells across all surfaces and confirmed our hypothesis. This further supports that ECM mediated adhesions are upregulated due to substrate stiffness and modulates metabolic signatures.

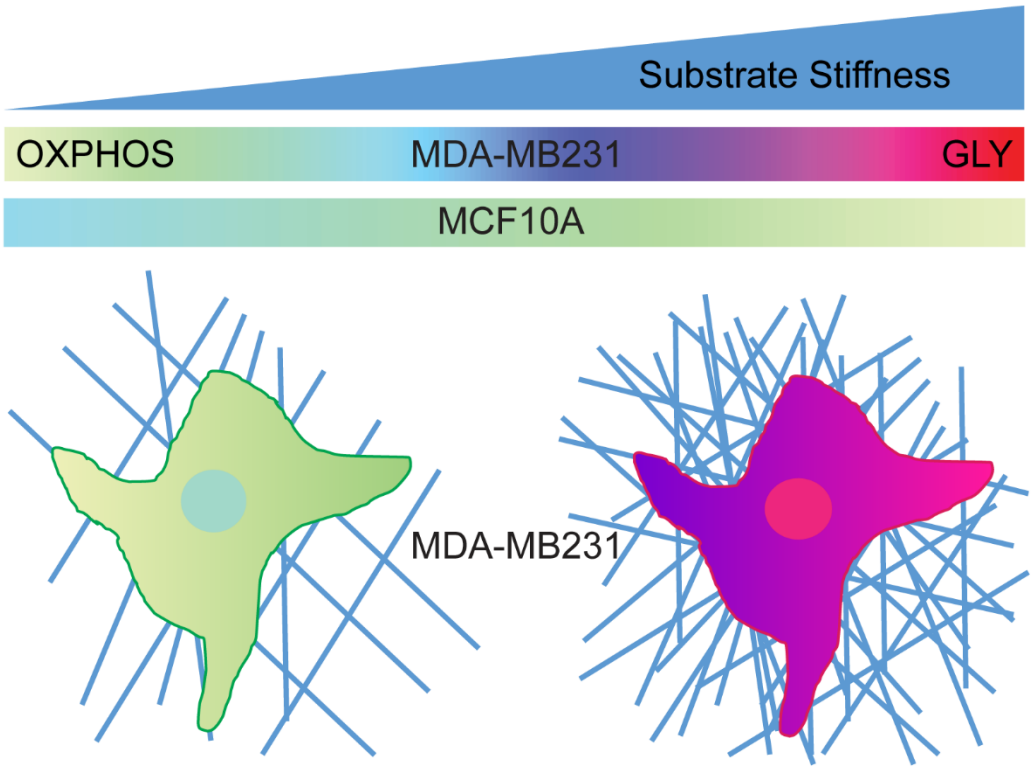

Figure 3.9: Modulation of cell metabolism by substrate stiffness. Increasing collagen stiffness causes a shift in highly invasive MDA-MB231 cancer cells from glycolysis to oxidative phosphorylation. MCF10A non-tumorigenic cells have little change in metabolism signatures in response to substrates stiffness.

We also confirmed that the changes in NADH free: bound in MDA-MB231 and MCF10A cells were due to GLY or OXPHOS by inhibiting these pathways with dichloroacetate and 2-deoxyglucose or rotenone and antimycin A, respectively. With

our results combined with what is known in the literature, there is a relationship between the mechanosensing and metabolism pathway in cancer cells and both play a critical role in regulating cancer invasiveness. This provides insight to develop therapies which target mechanosensing abilities of cancer cells to revert their metabolism similar to a more non- tumorigenic cell type or decrease their invasiveness.

In the next chapter, I will look more closely at the cell-to-substrate interactions of MDA-MB231 cell on the collagen substrates when grown in 3D matrices. As mentioned at the end of Chapter 2, collagen ECM forms nanosized structures in the form of fibrils. We hypothesize that these can change the organization of the integrin-mediated adhesions and used advanced imaging analysis method, z-phasors, to observe these changes. I will also measure the tension experienced at the focal adhesions due to nanotopography on a 2D model surface and 3D collagen matrices. Lastly, I will measure mitochondria trafficking and metabolism of MDA-MB231 cells during matrix invasion. These findings will allow us to draw conclusions on the roles of collagen density, integrin-mediated adhesions, and mitochondria trafficking in modulating metabolism and invasion within cancer cells.

Chapter 4

4. The role of collagen density in mechanosensing and mitochondria trafficking for cancer cell invasion

4.1. Phasor representation of proteins for Förster resonance energy transfer

In **Chapter 2**, the phasor plot was used to represent the FLIM signature of NADH. Another application of the phasor plot is in the study of protein-protein interactions. Current assays that study such interactions are done biochemically through co-immunoprecipitation, bimolecular fluorescence complementation, affinity electrophoresis, among many others. These processes typically require lysing the cell and isolating cellular components to observed expression levels, losing spatiotemporal information that can be obtained in live samples. The development of fluorescent protein biosensors coupled with live-cell imaging has enabled the visualization and measurement of intracellular molecular dynamics with high spatiotemporal resolution. Förster resonance energy transfer (FRET) is where the energy is transferred from the

excited protein (donor) to a secondary protein (acceptor). **Figure 4.1** displays the Jablonski diagram of FRET. The probability for this to happen depends on the distance between the donor and acceptor, the spectral overlap of the emission of the donor and the absorption of the acceptor, and the orientation of the electron dipole orbitals of the donor and acceptor with respect to one another. Similarly to conventional fluorescence, the amount of time it takes for the excited protein to return to the ground state is the lifetime. Some of the factors that can change the lifetime of a fluorescent probe include pH, solvent, binding to other molecules, and temperature,[143] thus making FLIM a powerful tool to measure processes in live cells due to its sensitivity.

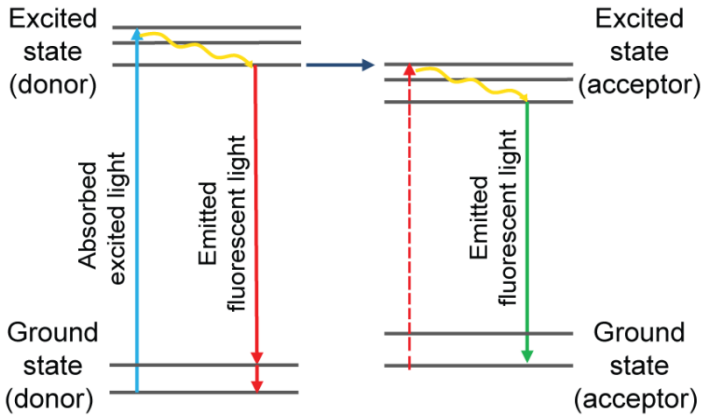

Figure 4.1 Jablonski diagram of FRET

The phasor representation can also be used to display the FRET efficiency of the sample by applying a Fourier transformation once again.[144] In this case, the lifetime of the donor is measured in the presence (τ) and absence (τ_D) of the acceptor (**Equation 4.1**). When the donor and acceptor undergo FRET, the lifetime of the donor is decreased

due to quenching. Thus, a FRET trajectory is observed and the efficiency increases along the trajectory (**Figure 4.2**).

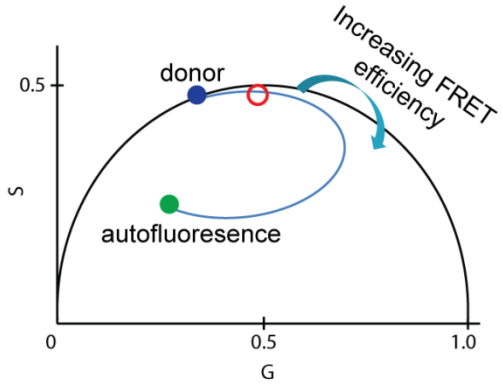

Figure 4.2: FRET/phasor representation. The curved trajectory (blue curve) corresponds to the FRET efficiency (0-100%). As the red cursor traces the trajectory from the donor (blue spot) to the autofluorescent background (green cursor), the FRET efficiency is calculated.

$$E = 1 - \frac{\tau}{\tau_D} \tag{4.1}$$

4.2. Chapter 4 Abstract

Cancer metastasis involves a combination of cellular processes such as actin polymerization, cell contractility, membrane formation, and matrix degradation. These processes require ATP consumption in order to sustain the migration of the cell. Cancer cells migrate through collagen matrices by pulling and remodeling the collagen fibers to promote collagen fibrillogenesis and density. In addition, recent studies have shown that mitochondria are recruited towards the leading edge in migrating cells to sustain

all these events. Here, we studied cell-to-matrix interactions by looking at focal adhesion organization and tension on nanolined surfaces (L860) as our model of collagen fibers. Increased tension was found in the focal adhesions of MDA-MB231 cells when grown on L860 surfaces and resulted in an increase in z-difference between integrin and paxillin proteins. We then measured the tension of these adhesions in 3D collagen matrices and observed mitochondria trafficking towards protruding edges. We also measured the metabolic index of these protrusions before and after extension. Our results show that MDA-MB231 cells within 3.0 mg/mL collagen matrices had more tension at the adhesions and exhibited a change in metabolic signatures from OXPHOS to GLY after extension of the protrusion. When these cells were grown in 1.2 mg/mL matrices, no change in metabolism was seen. These results show for the first time that increase of collagen density yields increased tension at the focal adhesions and results in metabolism signatures shift towards GLY when cancer cell invade within denser collagen matrices.

4.3. Introduction

Metastasis occurs when cancer cells lead the primary tumor site and invade into a secondary part of the body. This process uses multiple cellular processes in order to coordinate the forward motion of migration, matrix degradation, and survival. These

complex events require a large amount of energy in the form of ATP to fuel the changing network of the actin cytoskeleton.[145] The mechanical properties and substrate topography also affect the cell's ability to form adhesions and initiate migration.[24,33,87,111,146,147] Topography containing micro- or nanostructures have been shown to affect migration directions, focal adhesion dynamics, and cellular tension.[24,81,88,148] Our lab has introduced an imaging analysis technique, z-phasors, to gain super-resolution information about protein organization.[149] We applied this technique to look at the architecture of focal adhesion proteins, integrin, and paxillin when MDA-MB231 breast carcinoma cells are grown on flat and nanoline structures. This allowed us to model the effects of the nanotopography that exists in collagen ECMs and draw conclusions about cell behavior at the protein level.

Focal adhesion complexes also have been found to form a rosette at the base of the protrusion in order to support the extension of the invadopodia and recruitment of matrix metalloproteinases (MMP).[44,47,150] Invadopodia are actin-rich protrusions that are utilized for degradation of the extracellular matrix (ECM).[37,41,151] The process of cancer cell invasion occurs has been described as a multi-stage process which begins with the formation of focal adhesion through integrin-ECM interactions.[39,151,152] Once these adhesions are formed, actin polymerization and branching occur which signals cortactin, N-WASP, and Src activation which promotes the production of MMP for

matrix degradation.[153,154] These protrusions can further extend with the aid of microtubules to facilitate invasion by remodeling the surrounding ECM.[35,155,156] It is hypothesized that mitochondria are transported to the leading edge and protrusions of cancer cells to locally supply an abundance of ATP to sustain processes involved in invasion.[54,107,108]

Mitochondria are key players in producing ATP within the cell. Cells which have a directional migration show evidence of mitochondria recruitment to the leading edge.[56,108] It has also been found that changes in the architecture and density of the ECM can also regulate the ATP levels within invading cells in 3D collagen matrices.[157] In addition, ATP usage is increased when migration is promoted and decreased when cell contractility is inhibited. Thus, there is evidence that mitochondria are important for sustaining processes such as invasion where there could be frequent events of contraction and extension. However, there is still a lack of understanding of the role of mitochondria trafficking and metabolic indexes in response to collagen density.

Advances in fluorescent imaging, biosensors, and photo-activatable probes have made it possible to measure and stimulate specific proteins that interact with cell adhesion and migration. In particular, we used a vinculin tension sensor that measures the forces at the focal adhesions. This sensor is coupled with a pair of fluorescent proteins, mTFP, and venus, that undergo Förster resonance energy transfer (FRET)

when tension is not applied across vinculin.[158] Vinculin is a protein within the focal adhesion complex that is recruited when cell contraction and focal adhesion contraction is stimulated.[19,21,159,160] We also stimulated cell migration through the activation of Rac1 photoactivation of PA-Rac1.[161,162] Rac1 is known to be upregulated within invadopodia[48] and promote actin polymerization and lamellipodia formation at the leading edge during migration.[163–165] With these two probes, we are able to measure tension measurements within breast cancer cells, MDA-MB231 within 3D collagen matrices of different densities, and stimulate actin polymerization to observe mitochondria recruitment to regions of Rac1 activation.

Using nanolines as our model of collagen topography, we were able to show that the stacking of integrin and paxillin is changed. Integrin and paxillin proteins were found to double in separation when MDA-MB231 cells were grown on nanoline surfaces compared to flat surfaces. An explanation of this could be due to tension applied at the focal adhesion complex. This was confirmed by our findings using the VinTS FRET biosensor. MDA-MB231 cells were found to be under more tension when grown on L860 nanoline patterns compared to those on flat surfaces. When translated to 3D collagen matrices, cells grown on denser collagen 3D matrices also had increased tension at the adhesions. The increase of tension causes actin polymerization which requires ATP usage. This leads us to hypothesize that mitochondria recruitment could

be stimulated through actin polymerization. By activating PA-Rac1 locally, we were able to see mitochondria recruited to the site of activation. Mitochondria transport speed was shown to increase compared to when PA-Rac1 is unstimulated or absent in MDA-MB231 cells. In addition, the recruitment was shown to be directionally linear. We further tested if these denser matrices also alter the metabolism of the cells in 3D due to this recruitment. The denser collagen matrices had a slight shift in their metabolic signature from oxidative phosphorylation (OXPHOS) to glycolysis (GLY). Mitochondria recruitment was seen during protrusion extension which could play a role in the changes in metabolic signatures.

4.4. Results and discussion

4.4.1. Focal adhesions within MDA-MB231 are reorganized when grown on nanotopography

During cancer invasion, the collagen matrix is remodeled and compacted by the cancer cells.[123,166,167] This facilitates increased migration by promoting collagen fibrillogenesis and provides a linear trajectory along the fibers. For some preliminary work, we used a nanoline surface made from poly(methyl methacrylate) (PMMA) to model the similar linear organization as the collagen fibers during invasion. With this

surface, we can see changes in focal adhesion (FA) organization and tension experienced at the adhesions.

The L860 patterns were fabricated with a periodicity of 860 nm periodicity, 430 nm feature size, and 200 nm height using a hydraulic press. After fabrication of these features, cell studies were conducted to observe FA organization. A z-stack of the adhesions were taken and the z-phasor was calculated as previously described.[149] Z-positions were recorded of each pixel by calculating the center of mass of the fluorescent signal along the z-axis. This allows us to locate the z-position of each fluorophore in the Z-stack. MDA-MB-231 cells transfected with integrin-YFP (integYFP) and paxillin-CFP (paxCFP) were seeded on flat and L860 substrates coated with fibronectin tagged rhodamine (FNRho). The FNRho necessary to correct tilting of the surface. Once the z-phasor is generated from each image, colored cursors are used to highlight the points that correspond to areas of the FAs in the original image to record the average z-position of these pixels (**Figure 4.3a**). It was found that cells on flat and L860 substrates had an average difference of 8.1 ± 1.0 nm and 14.8 ± 0.8 nm, respectively, between integrin and paxillin (**Figure 4.3b**). This difference in z-position of these proteins on flat surfaces were similar to those found by Kanchanawong *et al.*[8] We also treated the cells with ROCK inhibitor, Y-27632, which inhibits cell contractility within the cells. There was no significant difference in the separation between integrin

and paxillin in these cells. However, the distance of separation was calculated to be much more than expected. A possible explanation for this could be that paxillin is transiently binding to the adhesion complex which could result in a higher z-position on average. We hypothesized that increased separation in z-position could be due to increased tension when the cells are seeded on the L860 surfaces. This then leads us to measure the tension at the focal adhesions.

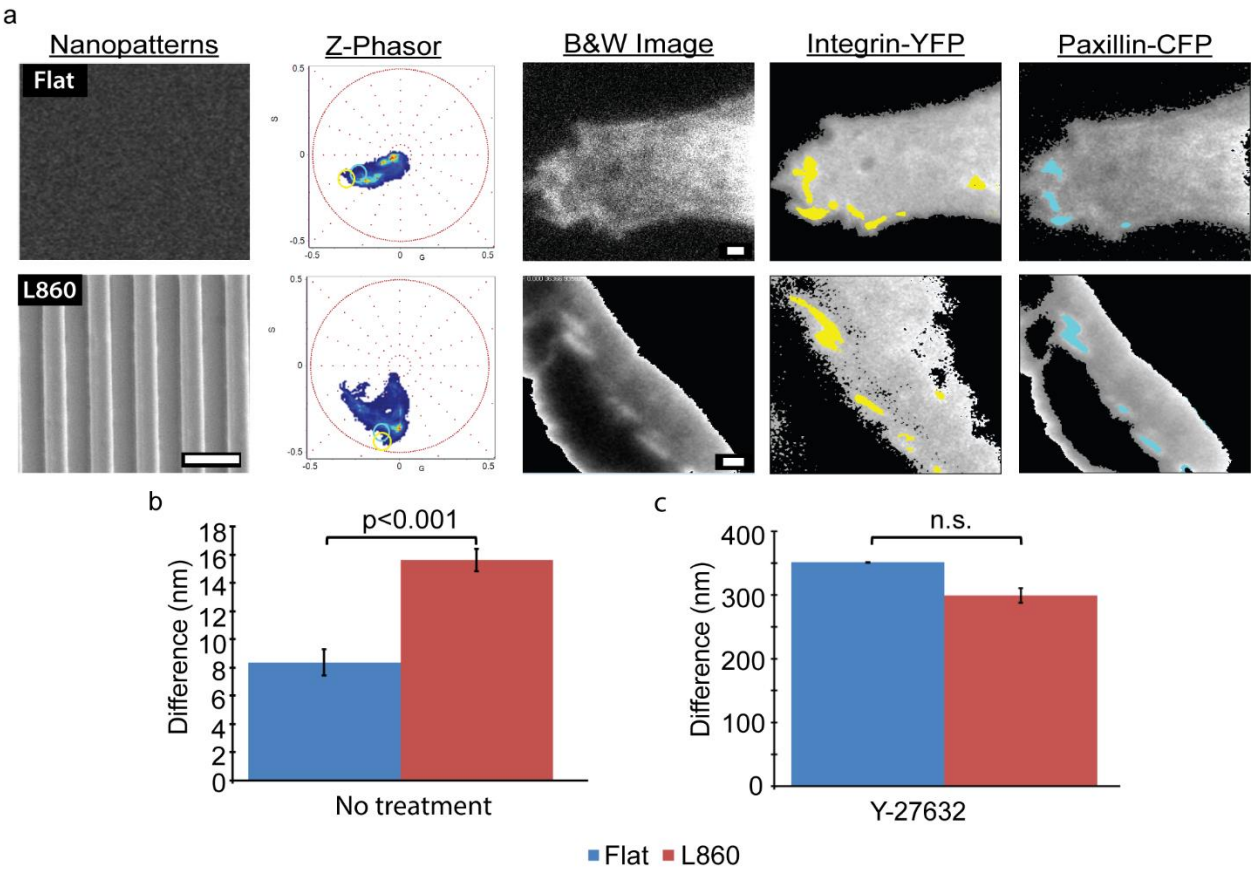

Figure 4.3: Z-phasors of integrin and paxillin on flat and L860 surfaces. (a) SEM images of nanopatterns and z-phasors representative images of z-phasors for MDA-MB231 cells on each surface. Yellow and cyan cursors within the z-phasor plot highlight corresponding pixels in the original B&W image where

integrin and paxillin aggregation form FAs. (b) Quantified data of the difference in z-position of integrin and paxillin on each surface. (c) The difference in z-position of integrin and paxillin on each surface after treatment with Y-27632. Error bars are S.E.M. Scale bar: 1μm

4.4.2. MDA-MB231 cells on nanotopography have increased tension at the focal adhesions

In order to examine how nanotopography affects tension experienced at the focal adhesions, we used a FRET vinculin biosensor. MDA-MB231 cells were cultured on flat PMMA and nanolined L860 surfaces fabricated from PMMA. We collected data from these cells transfected with a Vinculin tension sensor (VinTS) which would decrease in FRET efficiency when tension is applied across vinculin (**Figure 4.4**).[158] It has been shown that focal adhesions adhere to the edges of topographical structures.[148,168] This is hypothesized to allow stabilization of the adhesions and could exert more force across the adhesions when grown on patterned surfaces. As a positive control, cells were transfected with a vinculin tailless sensor (VinTL). This biosensor does not have the tail residue of vinculin and would undergo high FRET regardless of tension. Images of MDA-MB231 cells transfected with mTFP were collected to quantify the lifetime of the donor without the presence of an acceptor and served as our reference.

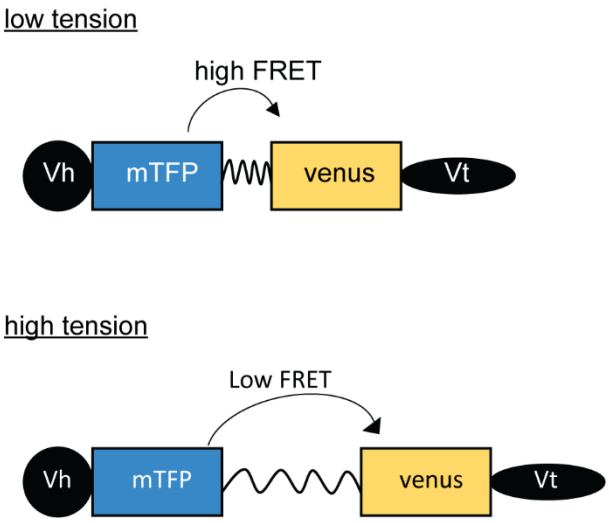

Figure 4.4: Cartoon of vinculin tension senor. When force is applied across vinculin, fluorescent probes mTFP and venus are pulled apart and yield low FRET. Vh and Vt signify the head and tail domains of vinculin, respectively.

We expect that the FRET efficiency for MDA-MB231 VinTS cells on the L860 surface to decrease due to increased tension. This was confirmed in our results with a FRET efficiency of 0.18 compared to those on flat surfaces with a FRET efficiency of 0.23, as shown in **Figure 4.5.** This showed that the cells experienced increased tension when grown on nanotopography. When MDA-MB231 cells expressed VinTL and seeded on flat or L860 surfaced, there was no significant difference in their FRET efficiencies with values of 0.35 and 0.37, respectively. This was expected as VinTL does not contain the tail part of vinculin, preventing it from attaching to actin and being pulled apart. The donor and acceptor within VinTL would be closer together spatially and yield a higher FRET efficiency, regardless of the surface they were on. Since the

MDA-MB231 VinTS cells on L860 surfaces experienced increased tension as shown from our FRET data, this could be an explanation for their change in focal adhesion architecture that we observed. The actin fibers could have more of an upward pull on the focal adhesion complex which would cause the integrin and paxillin proteins to change in their organization in the z-axis.

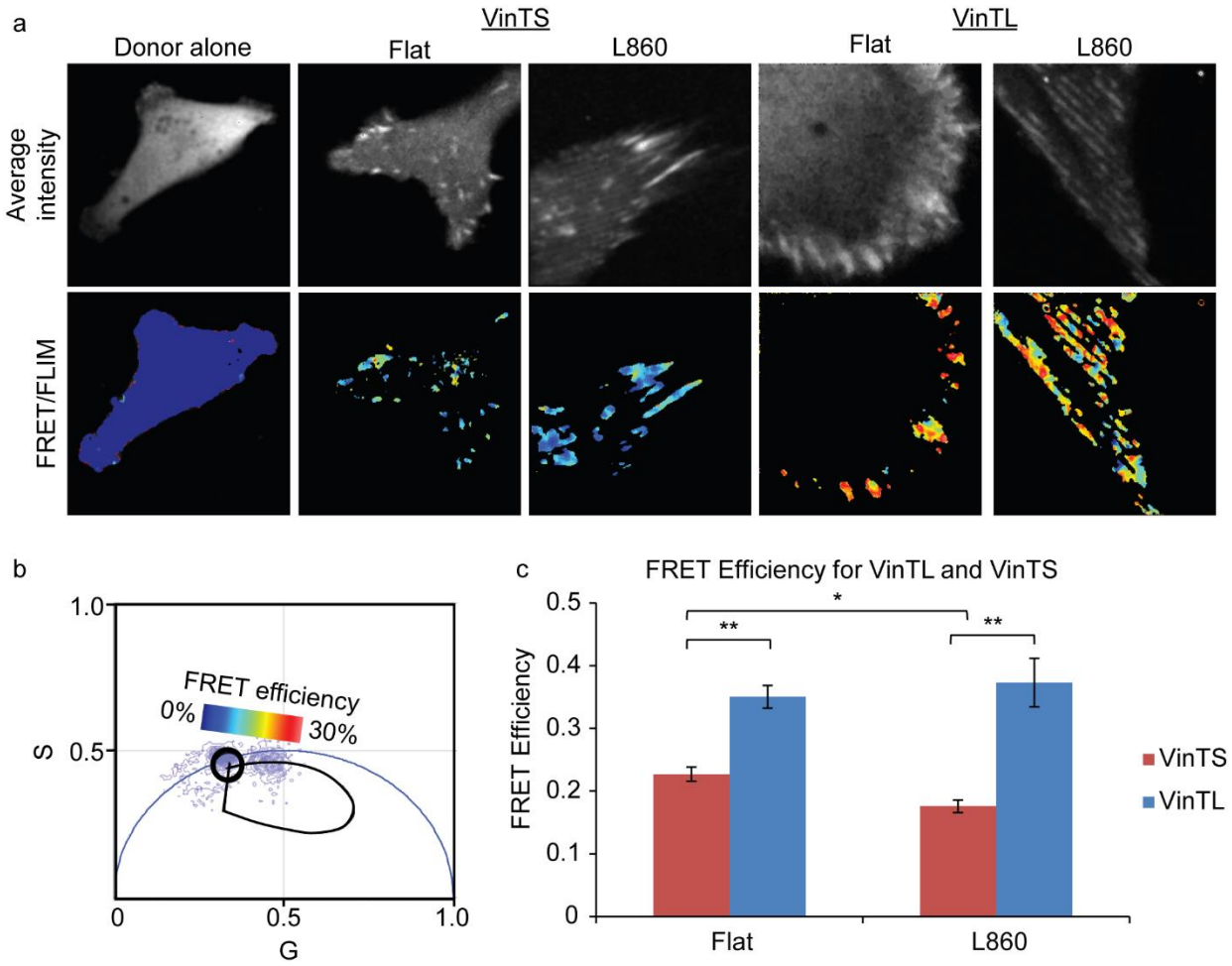

Figure 4.5: FRET measurements on flat and L860 surfaces (a) Average intensity and FLIM measurements of MDA-MB231 cells expressing VinTS and VinTL. FLIM images are colored based on the FRET efficiency color scale in (b). (b) Calculated FRET phasor where FRET efficiency increases along the black outlined

trajectory is traced clockwise. The color scale shows FRET efficiency from 0-30% (blue to red). (c) Quantified FRET efficiencies for MDA-MB231 cells expressing VinTS and VinTL on flat and L860 surfaces. * p<1e-2, ** p<1e-4 from Student t-test. Error bars are S.E.M.

4.4.3. Rac activation induces mitochondria recruitment

Actin branching, cell migration, and invasion are known to be simulated by Rac1 activity and require ATP.[48,157,163,169] Invasive protrusions within cancer cells are known to be actin-rich and require membrane formation.[170,171] In addition, collagen stiffness and nanotopography are known to increase actin branching.[172,173] Thus we aimed to stimulate actin polymerization and membrane formation through Rac1. Previous studies have shown that mitochondria are recruited to protrusions in 3D collagen matrices,[54] but it has yet been connected to actin polymerization or Rac1 activation. These processes require ATP and it is possible that mitochondria are trafficked to these regions to meet the local energy demands.[174–176] MDA-MD231 and MCF10A cells were transfected with PA-Rac1 and Cox8-GFP and grown on glass substrates. Cox8-GFP tags the Cytochrome C oxidase subunit VIII within the mitochondria and served as our mitochondria fluorescent tag.[177] Rac1 was then activated locally at the leading edge with a 458 nm laser which allowed a conformational change in PA-Rac1 to open and bind to its effectors for activation.[162]

We tested 3 different conditions of each cell line where PA-Rac1 and xPA-Rac1 indicate cells that expressed the photoactivatable Rac1, whether activated or not activated, respectively. The Cox8 condition indicates cells which did not express the PA-Rac1 protein (i.e. only expressed Cox8-GFP). MCF10A cells did not show any recruitment of mitochondria upon activation but still showed signs of membrane ruffling, as shown in **Figure 4.6**. As a second control, we also looked into NIH3T3 fibroblast cells expressing PA-Rac1 and Cox8-GFP but this cell line also did not show any recruitment of mitochondria.

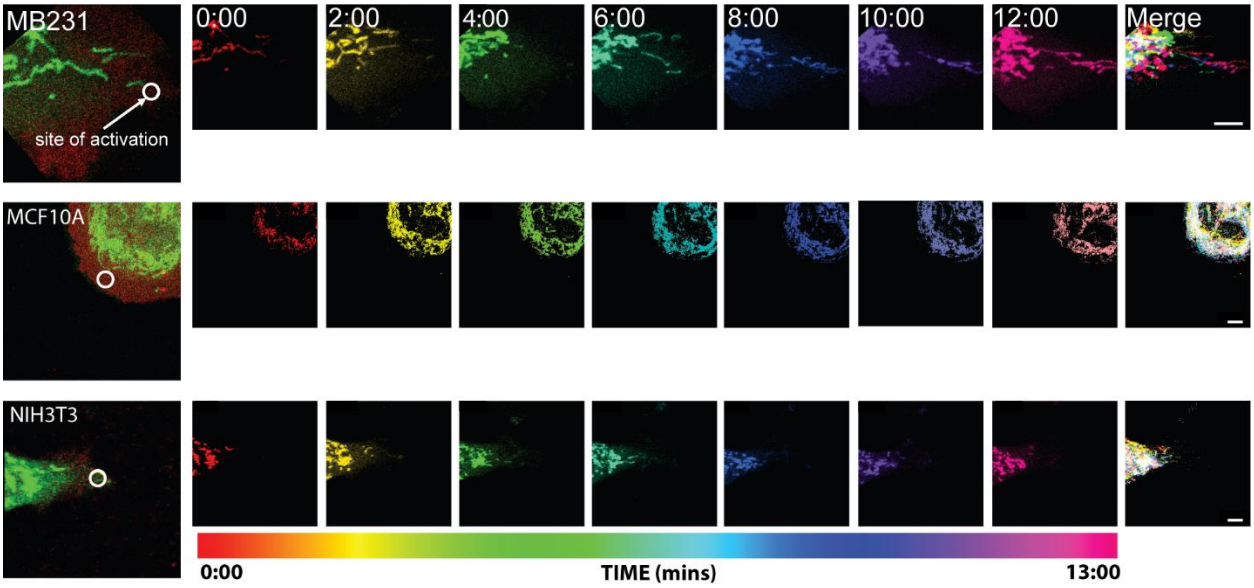

Figure 4.6 Rac1 activation and mitochondria trafficking. Rac1 was activated near the leading edge (open circle) and mitochondria trafficking was observed in MDA-MB231, MCF10A, and NIH 3T3 cells. Scale bar: 5 μm

We then compared the speed and directionality ratio, DR, of transported mitochondria in MDA-MB231 cells using a previously published excel macros for the analysis.[178] An increased directionality ratio of DR=0.50 was seen in PA-Rac1 cells compared to xPA-Rac1 (DR=0.41) and Cox8 alone (DR=0.31) cells, as shown in **Figure 4.7a**. Cells in which PA-Rac1 was activated showed increased average speed of mitochondria transport (3.07 μm/s) compared to those that only expressed Cox8-GFP (1.50 μm/s). xPA-Rac1 (e.g. cells which expressed PA-Rac1 but were not activated) also showed a slight increase (2.47 μm/s) in recruitment compared to Cox8 alone cells. This could be due to extraneous effect, viz., ambient room light that activated the protein. Our results show that when PA-Rac1 is activated, mitochondria are transported with increasing speed and along a linear trajectory towards the slight of activation compared to the other conditions. In particular, the recruitment only happens within our tumorigenic cell line.

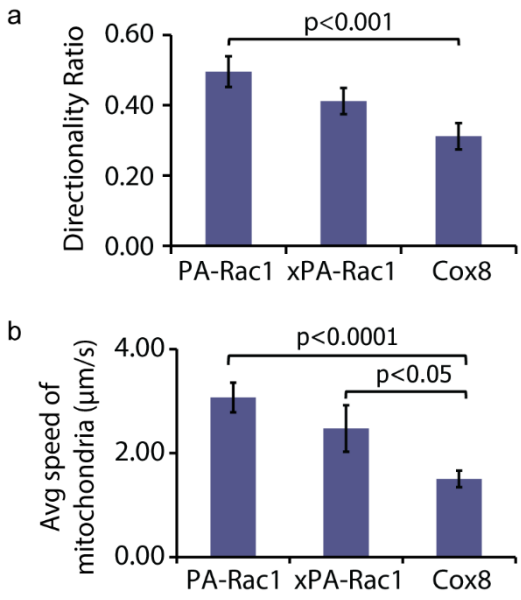

Figure 4.7 Quantification of mitochondria recruitment upon Rac1 activation. (a) Average directionality ratio and (b) average speed of PA-Rac1 (n=39), xPA-Rac1 (n=38) and Cox8 alone (n=36) cells were calculated using excel macros.[178] Error bars represent S.E.M.

4.4.4. MDA-MB231 tension and mitochondrial trafficking in 3D collagen

MDA-MB231 cells expressing VinTS were then grown within 3D collagen matrices of two different concentrations, 3.0 mg/mL and 1.2 mg/mL. These substrates were characterized in **Chapter 3,** where 3.0 mg/mL matrices were found to be denser. Increase density has been shown to increase cell contractility, actin polymerization, focal adhesion stabilization, and invasion.[48,179] Thus, MDA-MB231 cells should show increased tension at the focal adhesions when they are grown on the 3.0 mg/mL collagen substrates. This was confirmed with the VinTS protein, where we observed a

decrease in FRET efficiency when MDA-MB231 cells were grown on 3.0 mg/mL collagen matrices (**Figure 4.8**). We also measured the stability of the adhesion on the collagen substrates and on glass as a control.

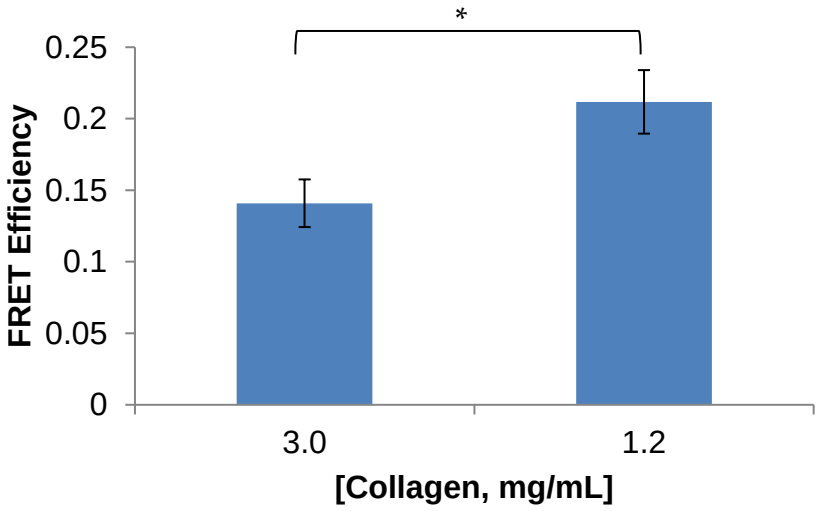

Figure 4.8: VinTS measurements of MDA-MB231 cells in 3D collagen matrices. Quantified FRET efficiencies of MDA-MB231 cells expressing VinTS in 3D collagen matrices. * $p<0.05$. Error bars are S.E.M.

In order to correlate our finding of substrate stiffness to the stability of focal adhesions dynamics in cells, we analyzed the diffusion of talin-GFP, a protein associated with integrin-mediated adhesions and the actin cytoskeleton, by using raster image correlation spectroscopy, or RICS. In **Chapter 2**, we demonstrated that increased spatiotemporal focal adhesion diffusion of proteins at the focal adhesions indicated active adhesion association and dissociation whereas stable adhesions had a steady state population.[24,95,180] By measuring the diffusion of talin at the FA, we can observe the motility and stability of the adhesions. We hypothesized that MDA-MB231 on stiffer

matrices would show a decreased diffusion of talin-GFP due to increased FA stability. We imaged MBA-MB231 cells transiently transfected with talin-GFP and observed an increase of diffusion with substrates stiffness (Error! Reference source not found.). This hows that the adhesions become less stable when collagen density was decreased. Cells on glass were treated with Y-27632, a specific inhibitor of kinase (ROCK) and cell contractility, to disrupt the mechanical tension.[134] These cells had an increased diffusion of talin-GFP compared to the untreated cells, further confirming that increased tension results in more stable adhesions. Since increased collagen density promotes invasion and metabolism shifts, as shown in our results in **Chapter 3**, we then attempted to capture these changes over time.

MDA-MB231 cells expressing Cox8-GFP were embedded in 3.0 mg/mL and 1.2 mg/mL 3D collagen substrates. Fluorescent lifetime images of NADH and second harmonic generation images of collagen were taken before and after protrusion extension (**Figure 4.9**a). This allowed us to quantify metabolism signatures and matrix remodeling. One hour time-lapse images were also used to observe mitochondria recruitment as the protrusion invaded the matrix. Since we have shown that membrane formation and actin polymerization stimulate mitochondria recruitment, it is possible that changes in metabolic signatures can be observed. We found that the protruding end of cells on 3.0 mg/mL collagen matrices showed a slight shift from OXPHOS to GLY

after one hour of invasion (**Figure 4.9d**). This shift was not as evident when the cells were grown in 1.2 mg/mL collagen matrices (**Figure 4.9c**). In addition, matrix remodeling was more striking on our denser substrates. Cancer cells are known to use aerobic glycolysis, or the Warburg effect, to carry out their metabolism. Thus, it is not surprising that these cancer cells would shift towards a more glycolytic form of metabolism in order to quickly produce ATP for processes such as invasion.

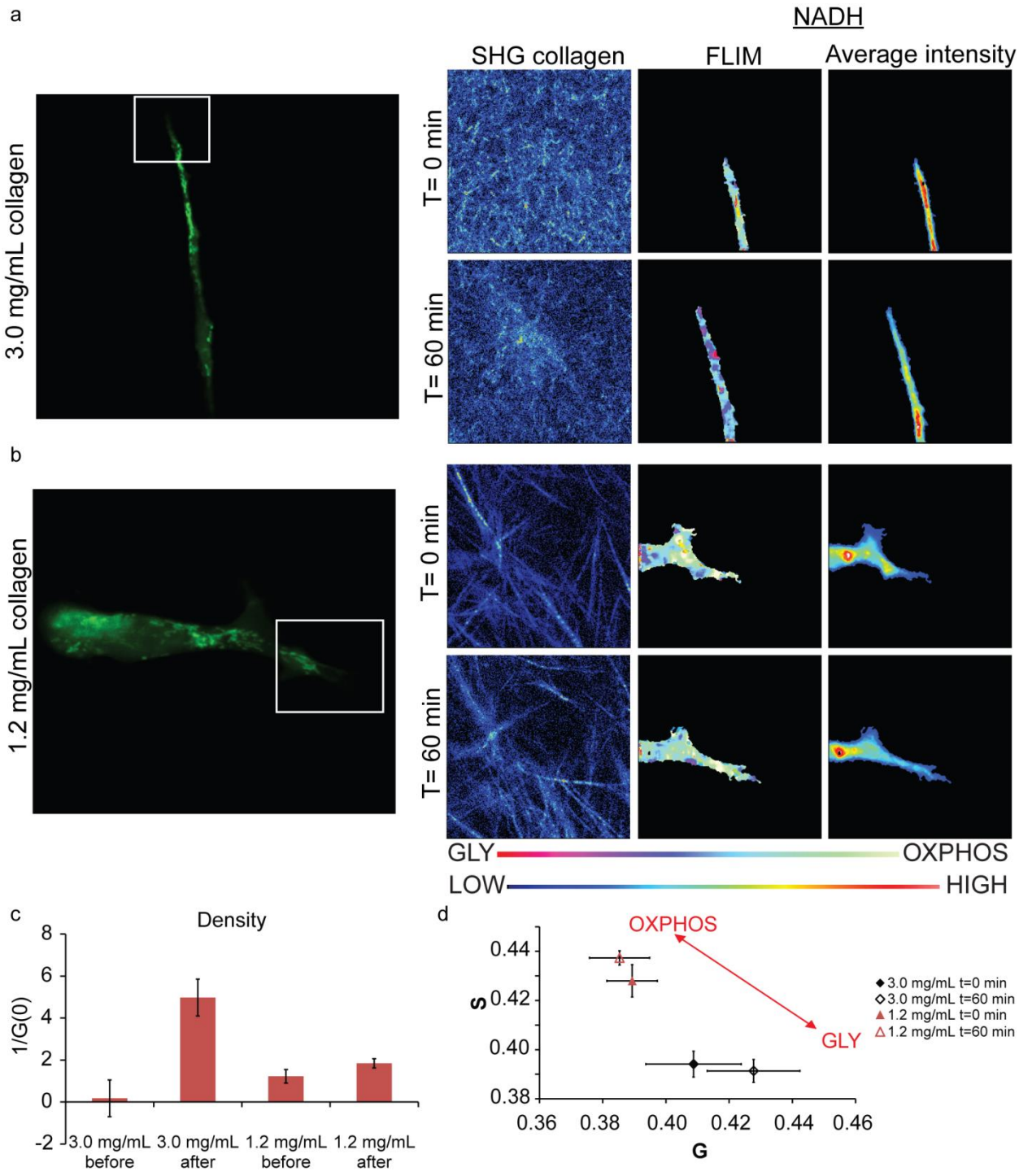

Figure 4.9: FLIM of NADH and SHG of collagen before and after MDA-MB231 protrusion extension. MDA-MB231 cells in (a) 3.0 mg/mL and (b) 1.2 mg/mL 3D collagen matrices. White boxes show zoomed

in areas in which SHG and FLIM NADH images were taken. (c) Quantification of changes in collagen density before and after protrusion extension. (d) Phasor plot of NADH FLIM signatures at the protrusions.

Mitochondria recruitment was also seen in MDA-MB231 cells when grown in both matrices but further studies will have to be conducted to see if the speed of the recruitment correlates with the metabolism changes. Altogether, these results show that increase collagen density causes metabolic changes within the protruding end of cancer cells which could result in mitochondria recruitment to the tips of the protrusions. This could also allow the cells to carry out processes such as matrix remodeling which requires energy in the form of ATP.

4.5. Materials and method

4.5.1. Cell culturing and transfections

Dulbecco's Modified Eagle's Medium (DMEM) with high glucose, L-glutamate, and sodium pyruvate (Genesee Scientific, San Diego, CA) supplemented with 10% heat-inactivated Fetal Bovine Serum (Thermofisher Scientific, USA) and 1% Penicillin-Streptomycin 100X Solution (Genesee Scientific, San Diego, CA) was used as the culturing media for MDA-MB231 and NIH3T3 cells. MCF10A cells were cultured in DMEM/F12 containing high glucose, sodium pyruvate and L-glutamine (Thermofisher

Scientific, USA). This was supplemented with 5% horse serum (Thermofisher Scientific, USA), 20 ng/mL epidermal growth factor (Thermofisher Scientific, USA), 0.5 mg/mL Hydrocortisone (Sigma-Aldrich, St. Louis, MO), 100 ng/mL cholera toxin (Sigma-Aldrich, St. Louis, MO), 10 μg/mL insulin (Sigma-Aldrich, St. Louis, MO), and 1% Penicillin-Streptomycin 100X Solution (Genesee Scientific, San Diego, CA).

A 35 mm glass imaging dish (MatTek, Ashland, MA) was coated with 1ug/mL rhodamine-fibronectin (Cytoskeleton, Denver, CO) and allowed to incubate for at least 1 hour at 37^0C. $0.5x10^6$ MDA-MB231 cells were then plated on the dishes and allowed for attachment overnight. Cells were then co-transfected with α5-integrin-YFP and paxillin-CFP with Lipofectamine 3000 (Life Technologies, Rockville, MD) following the manufacturer's protocol. Cells were then fixed with 4% paraformaldehyde (Sigma-Aldrich, Milwaukee, WI) for 30 minutes and washed thoroughly with 1X PBS before adding VECTASHIELD anti-fade mounting oil (Vector Laboratories, Burlingame, CA) before imaging.

MDA-MB231 cells stably expressing mTFP-N1 and cultured on a 35 mm glass imaging dish was used for collecting the fluorescent lifetime of the donor alone for FRET experiments. For transfections, $0.5x10^6$ MDA-MB231, NIH3T3 or MCF10A cells were seeded in a 6-well plate overnight at 37^oC, 5% CO_2. For flat and L860 experiments with MDA-MB231 VinTL, $1x10^6$ cells were transfected with 1μg VinTL (Addgene,

Cambridge, MA #26020) using a Lonza Nucleofector system (Lonza, Basel, Switzerland) following manufacturer's protocol. These cells were then divided across 2 samples so the final cell count is $0.5x10^6$ cell per sample. For flat and nanostructure experiments with MDA-MB231 VinTS, $0.5x10^6$ MDA-MB231 cells were seeded into a 6-well plate overnight and transfected with 1μg VinTS (Addgene, Cambridge, MA #26019) using Lipofectamine 3000. These cells were then transferred to their experimental substrates for imaging. MDA-MB231 VinTS cells were transfected the same way for 3D collagen experiments but then added to collagen as described in "Collagen preparation". PA-Rac1-mCherry (PA-Rac1) plasmid and Cox8-GFP were generously donated by Dr. Klaus Hahn and Dr. Susanna Rafelski. These plasmids were also transfected with Lipofectamine 3000 after $0.5x10^6$ cells were plated within a 6-well plate.

4.5.2. Fabrication of nanostructures

Glass slides (1.5, 22 x 22mm) coated with a poly(methyl methacrylate) (PMMA, Mw = 120 kDa, Sigma-Aldrich, Milwaukee, WI) film as previously described.[24] Briefly, slides were treated with UV-ozone for 5 minutes then coated with 3-aminopropyltriethoxysilane (APTES, Sigma-Aldrich, Milwaukee, WI) in deionized water (1% volume). PMMA was dissolved in toluene (5% w/v) overnight at 65 ^{0}C and added to the glass slides by spin-coating at 600 rpm for 45 seconds. Afterward, slides were placed on a hot plate at 100 °C for 5 minutes. Hard-polydimethylsiloxane negative

stamps were made from a silicon nanoline stamp (Lightsmyth, Eugene, OR) as previously described[181] and were denoted as L860 (periodicity = 860nm, depth 200nm, duty cycle=50%). Slides, denoted as flat surfaces, were created using the same methods without imprinting structures. The hPDMS L860 molds were used to thermal imprint L860 structures on the PMMA slides using a hydrolytic press (Tetrahedron, San Diego, CA). An imprinting temperature of 170 ^{0}C and pressure of 245N was applied for 15 minutes. The system was then cooled to room temperature to allow the PMMA to solidify to the shape of the features. Pressured was then released and the hPDMS stamp was demolded to reveal the L860 pattern.

4.5.3. Nanostructure dish preparation

Custom-made sample dishes were prepared for the experiments. A 15 mm cork borer was heated over an open flame and pressed into the center of a 35 mm culture dish (Corning, Midland, MI) and sanded down to create an open bottom dish. For either the L860 or PMMA glass slides, they were centered at the opening and attached with a silicone adhesive (Corning, Midland, MI) and allowed to dry overnight. Before adding cells, dishes were UV-sterilized for 5 minutes and coated overnight with 1 μg/ml fibronectin (Sigma-Aldrich, Milwaukee, WI) at 37 °C.

4.5.4. Collagen preparation for mitochondria and tension experiments

Rat tail collagen Collagen I (Corning, Corning, NY), microcentrifuge tubes, 0.5N NaOH, and 10X PBS with phenol red (Thermofisher Scientific, USA) were kept on ice for as long as possible while handling. Collagen I was added to the microcentrifuge tube such that the final concentration was either 1.2 mg/mL or 3.0 mg/mL for a 0.5 mL final volume. 50 μL of 10X phosphate buffer saline containing phenol red was added dropwise while vortexing as a pH indicator. 0.5N NaOH was then added dropwise to the mixture with periodic vortexing until the solution became a slight pink (pH~7). 10,000 MDA-MB231 cells transfected with VinTS or Cox8-GFP and PA-Rac1 was isolated and resuspended in DMEM at a volume calculated for a 1.2 mg/mL or 3.0 mg/mL collagen solution. The resuspended cells were then added to the collagen mixture and mixed with vortexing. The collagen was then added to an 8-well glass bottom plate (Thermofisher Scientific, USA) and allowed to incubate for 30 minutes at 37^{o}C, 5% CO_2. Culture media was then added to the wells and returned to the incubator for imaging the next day.

4.5.5. Imaging acquisition

MDA-MB231 cells expressing VinTS, VinTL, or mTFP on flat PMMA or L860 surfaces were imaged on the Olympus FV1000 with a 60X/1.2 N.A. water immersion

objective. For 3D collagen experiments with MDA-MB231 cells expressing VinTS imaging was on a Zeiss LSM 880 with a 40X/0.8 NA water immersion objective. MDA-MB231 cells expressing talin-GFP were also imaged with the same setup. 100 frames were taken at a 256x256 pixels where the pixel size was no more than 80 nm with a dwell time of 4.10 us/pixel. These images were analyzed with SimFCS using the raster image correlation spectroscopy to a region of interest (ROI) of 64x64 pixels of where the focal adhesions were located. The RICS routine as previously described.[95,180,182] A moving average subtraction of 10 frames was applied to analysis to account for any bulk cell motion. ω_o, or the waist of the point spread function, was estimated as 0.3 μm. After generation of the autocorrelation function, a fit was applied with the correct imaging parameters and the diffusion of the talin-GFP molecules within the ROI.

Cells were kept under incubation at 30 ^{0}C and 5% CO_2 for the duration of the imaging sessions. VinTS, VinTL, and mTFP excitation were done at 875 nm with a two-photon Ti: Sapphire laser (Spectra-Physics MaiTai, Mountain View, CA). Emission was collected at 690 nm two and bandpass filter at 470/22 nm and 542/27 nm with 509LP filter. The signal was collected with photomultiplier tubes (H7422P-40, Hamamatsu, Japan). FastFLIM FLIMbox (ISS, Champaign, IL) acquired the frequency domain of the lifetime of VinTS until enough statistics were obtained. Images of coumarin-6 in 100% ethanol were to calibration all FLIM measures.

Z-phasor experiments done with MDA-MB231 cells co-transfected with integrin-YFP and paxillin-CFP were imaged on the LSM 710 with a 40X/1.2 water immersion objective. Z-stacks of the focal adhesions were taken starting from the surfaced of the rhodamine fibronectin layer to just above the focal adhesion complex. The slice interval was 50 nm with pixel dwell time of 6.30 μs and frame size of 256x256 pixels. Paxillin-CFP and Fibronectin-Rhodamine where excited together at 405 nm and 561 nm, respectively. Emission of CFP and rhodamine were collected at 463-516 nm and 578-696 nm. A separate track was used to excite α5-integrin-YFP at 514 nm with emission collection at 503 – 552 nm.

MDA-MB231, NIH3T3 and MCF10A cells co-transfected with PA-Rac1 and Cox8-GFP were imaging on the LSM 880 or Zeiss LSM 710 with a 63X/1.4 N.A oil immersion objective. PA-Rac1 was activated at 458 nm by bleaching a 5 μm spot at the leading edge every 3 frames. PA-Rac1 and Cox8-GFP were excited at 561 nm and 900 nm (2-photon excitation), respectively. Emission of the PA-Rac1 was collected at 579-696 nm after passing through an MBS 488/561 beam-splitter. Emission of Cox8-GFP was collected at 483-546 nm after passing through an MBS 690+ beamsplitter. Time-lapse images were collected with a 256x256 frame size with a scan time of 943.72 ms. FLIM images of NADH were taken at 740 nm with the Ti:Sapphire laser and collected with the same setup as the FRET experiments except the emission was collected with

bandpass filter at 442/46 nm and 520/35 nm with a with a dichroic mirror 484 nm long-pass filter. Second harmonic generation of the collagen generated with 2-photon excitation at 900 nm and collected also with the bandpass filters at 460/80 nm. The objective used for these measurements was a 25X/0.8 N.A. oil immersion objective.

4.5.6. Image analysis

Z-phasors were also analyzed using SimFCS as previously described.[149] The z-position of the integrin-YFP channel and paxillin-CFP channel were recorded separately and the difference between the two position was taken to observe any changes in the organization of the proteins. Rhodamine-Fibronectin was used to correct for any tilting of the sample.

Mitochondria tracking was done with Fiji ImageJ using the Manual Tracking plugin.[97] Only mitochondria which were trafficked towards the leading edge of the cell were analyzed. These coordinates were then used to calculate the directionality ratio and speed using Microsoft Excel macros as previously described.[178]

Collagen SGH, FRET/FLIM, and NADH/FLIM images were analyzed as previously described using the Globals SimFCS software developed at the Laboratory for Fluorescence Dynamics at UC Irvine (www.lfd.edu).[100–102,105,119–121,123,144] All FLIM files were calibrated with coumarin-6 in ethanol with a known lifetime of 2.5 ns. For FRET

images of VinTS, masks were made of the focal adhesions to record the FRET efficiency of only the adhesions.

4.5.7. Statistical analysis

All error bars were calculated as the standard error of the mean (S.E.M.) and significance was determined by student t-test.

4.6. Chapter 4 summary

Cancer invasion requires a multitude of processes such as membrane extension, matrix remodeling, and cell contraction. All of these processes expend energy in the form of ATP. There has been recent speculation that mitochondria are trafficked towards these regions in order to locally supply ATP. In our results shown in this chapter, we showed that mitochondria trafficking occur when membrane formation and actin polymerization is stimulated through the activation of Rac1. We then translated this knowledge to 3D collagen systems of varying density. MDA-MB231 cells expressing a vinculin FRET tension sensor showed increased tension at the adhesions within denser collagen matrices, as indicated with a decrease in FRET efficiency. This increase in tension is known to have more actin branching which is also true within invasive protrusions in cancer cells. Since we see mitochondria recruitment to the regions of membrane formation and actin polymerization, it is possible that changes in

metabolism signatures can also be seen during invasion. We conducted FLIM experiments of NADH before and after one hour of invasion at the protruding ends of the cells. MDA-MB231 cells were shown to have a metabolic shift from OXPHOS to GLY at the protrusions on our denser collagen matrices. These results together show that increase of collagen density increases tension at the focal adhesions. In addition, recruitment of mitochondria at the protrusions of the cell could be the cause of the change of metabolic signatures. Thus, therapies should consider targeting substrate density, metabolism and mitochondria trafficking to decrease metastasis.

Chapter 5

5. Conclusions and future directions

Tissue properties have been well known to be linked to cancer prognosis. Understanding cell-to-substrate interactions allow a better understanding of how the mechanical properties of the ECM can affect cellular processes. In recent years, there has been evidence that the cell's mechanosensing pathway interact with the metabolism pathways of the cell. There is still much to be learned about the details of the connection of these two pathways, and the studies presented here provide more insight on this topic.

In **Chapter 1**, I described the study of cell-to-substrate interactions at the protein level by looking at the dynamics of a focal adhesion protein, paxillin, on nanotopography. Tissues *in vivo* contain many contours and textures, thus, it is important to see how these affect cell adhesion and migration behaviors. As a model surface, I looked at the binding and unbinding dynamics of paxillin on nanotopography and how this affected migration of NIH3T3 cells. I showed that surfaces with decreasing nanopillar size yield a larger population of smaller aggregates and lead to a

decrease in migration. When NIH3T3 cells are able to form larger adhesions, the disassembling units increase in size and aids the cell in migrating a greater distance. Together, this shows that nanotopography can affect migration of cells down to the protein level.

In Chapter 2 I described my findings that collagen density is able to shift the metabolic signature of breast carcinoma cells. I showed that metabolism changes from glycolysis (GLY) to oxidative phosphorylation (OXPHOS) state when collagen density is decreased. In addition, I used a non-invasive method to observe these changes through measuring the ratio of free and bound NADH with fluorescence lifetime imaging microscopy. I was also able to see the metabolic signature of MDA-MB231 cells revert from GLY to OXPHOS when treated with ROCK inhibitor Y-27632. This indicated that metabolism is able to modulate through the mechanosensing pathways of the cell. Thus, both matrix properties and metabolism of cancer cells need to be considered when developing cancer therapies.

The final chapter of my work further looked at the role of mitochondria in cell migration, specifically to the leading edge. Mitochondria are key players in harvesting energy in the form of ATP to fuel the biological processes in the cell, such as actin polymerization. There have been numerous studies that observe their recruitment to the leading edge to locally supply energy to this region. We hypothesized that an increase

in collagen density allows more stable adhesions to form, and as a result, these adhesions should increase in tension and stimulate actin branching. The work I presented in this thesis looked at mitochondria recruitment in response to actin polymerization and membrane formation through the activation of Rac1. I have shown that mitochondria are recruited to regions of Rac1 activation. During cell migration in 3D collagen matrices, cancer cells form actin-rich invasive protrusions that also recruit mitochondria to the tips. I furthered studied the changes in metabolic signatures before and after invasion and found a shift towards GLY after one hour of invasion in denser collage matrices. This shows that metabolism shifts towards GLY, a faster method of producing ATP, to support membrane formation and actin polymerization. In addition, the recruitment of mitochondria supplies ATP locally to the invading protrusions.

The work presented in these chapters have shown that cell behavior and metabolism can be controlled by their surround microenvironment. Mitochondria trafficking is shown to be a response to protrusion extension and migration. It would be interesting to further study this mechanism by perturbing mitochondria transport and observe how this affects metabolic signatures at the protruding edge. Another parameter that would be worth looking at is the change of tension overtime as cancer cells invade and if this would correlate with the mitochondria trafficking speeds. The studies on mitochondria trafficking in 3D collagen matrices were done with confocal

microscope systems on a single z-plane. Other microscopy techniques such as single plane illumination microscopy (SPIM) or z-stacks would be a more accurate method to track 3D movements in order to track mitochondria motion. With the results presented here, it is evident that the microenvironment, metabolism and mitochondria transport should all be considered when developing therapies to decrease cancer metastasis and improve prognosis.

References

1. Indra, I. & Beningo, K. A. An in vitro correlation of metastatic capacity, substrate rigidity, and ECM composition. *J. Cell. Biochem.* **112,** 3151–8 (2011).
2. Mrksich, M., Dike, L. E., Tien, J., Ingber, D. E. & Whitesides, G. M. Using microcontact printing to pattern the attachment of mammalian cells to self-assembled monolayers of alkanethiolates on transparent films of gold and silver. *Exp. Cell Res.* **235,** 305–313 (1997).
3. Rashidi, H., Yang, J. & Shakeshe, K. M. Surface engineering of synthetic polymer materials for tissue engineering and regenerative medicine applications. *Biomater. Sci.* **2,** 1318–1331 (2014).
4. Bettinger, C. J., Langer, R. & Borenstein, J. T. Engineering substrate topography at the micro- and nanoscale to control cell function. *Angew. Chem. Int. Ed. Engl.* **48,** 5406–15 (2009).
5. Shen, C. J. *et al.* Decreased cell adhesion promotes angiogenesis in a Pyk2-dependent manner. *Exp. Cell Res.* **317,** 1860–1871 (2011).
6. McWhorter, F. Y., Wang, T., Nguyen, P., Chung, T. & Liu, W. F. Modulation of macrophage phenotype by cell shape. *Proc. Natl. Acad. Sci. U. S. A.* **110,** 17253–8 (2013).
7. Siegel, R. L., Miller, K. D. & Jemal, A. Cancer Statistics, 2015. *CA Cancer J Clin* **65,** 5–29 (2015).
8. Kanchanawong, P. *et al.* Nanoscale architecture of integrin-based cell adhesions. *Nature* **468,** 580–4 (2010).
9. Lauffenburger, D. A. & Horwitz, A. F. Cell migration: A physically integrated molecular process. *Cell* **84,** 359–369 (1996).
10. Cavalcanti-Adam, E. A. *et al.* Cell spreading and focal adhesion dynamics are regulated by spacing of integrin ligands. *Biophys. J.* **92,** 2964–74 (2007).
11. Bettinger, C. J., Langer, R. & Borenstein, J. T. Engineering substrate topography at the micro- and nanoscale to control cell function. *Angew. Chem. Int. Ed. Engl.* **48,** 5406–15 (2009).
12. Yue, J., Zhang, K. & Chen, J. Role of Integrins in Regulating Proteases to Mediate Extracellular Matrix Remodeling. *Cancer Microenviron.* 1–9 (2012). doi:10.1007/s12307-012-0101-3
13. Emsley, J., Knight, C. G., Farndale, R. W., Barnes, M. J. & Liddington, R. C. Structural Basis of Collagen Recognition by Integrin $\alpha 2\beta 1$. *Cell* **101,** 47–56 (2000).
14. Vicente-Manzanares, M., Choi, C. K. & Horwitz, a. R. Integrins in cell migration -

the actin connection. *J. Cell Sci.* **122,** 1473–1473 (2009).
15. Pelham, R. J. & Wang, Y. -l. Cell locomotion and focal adhesions are regulated by substrate flexibility. *Proc. Natl. Acad. Sci.* **94,** 13661–13665 (1997).
16. Kim, D. H. & Wirtz, D. Focal adhesion size uniquely predicts cell migration. *FASEB J.* **27,** 1351–1361 (2013).
17. Gardel, M. L., Schneider, I. C., Aratyn-Schaus, Y. & Waterman, C. M. Mechanical integration of actin and adhesion dynamics in cell migration. *Annu. Rev. Cell Dev. Biol.* **26,** 315–33 (2010).
18. Bieling, P. *et al.* Force Feedback Controls Motor Activity and Mechanical Properties of Self-Assembling Branched Actin Networks. *Cell* **164,** 115–127 (2016).
19. Hirata, H., Tatsumi, H., Lim, C. T. & Sokabe, M. Force-dependent vinculin binding to talin in live cells: a crucial step in anchoring the actin cytoskeleton to focal adhesions. *Am. J. Physiol. Cell Physiol.* **306,** C607-20 (2014).
20. Dumbauld, D. W. *et al.* How vinculin regulates force transmission. *Proc. Natl. Acad. Sci. U. S. A.* **110,** 9788–93 (2013).
21. Liu, J. *et al.* Talin determines the nanoscale architecture of focal adhesions. *Proc. Natl. Acad. Sci.* 201512025 (2015). doi:10.1073/pnas.1512025112
22. del Rio, A. *et al.* Stretching single talin rod molecules activates vinculin binding. *Science (80-.).* **323,** 638–641 (2009).
23. Hoffman, B. D., Grashoff, C. & Schwartz, M. a. Dynamic molecular processes mediate cellular mechanotransduction. *Nature* **475,** 316–323 (2011).
24. Liang, E. I., Mah, E. J., Yee, A. F. & Digman, M. A. Correlation of focal adhesion assembly and disassembly with cell migration on nanotopography. *Integr. Biol.* **9,** 145–155 (2017).
25. Arnold, M. *et al.* Activation of integrin function by nanopatterned adhesive interfaces. *Chemphyschem* **5,** 383–8 (2004).
26. Li, J.-R., Shi, L., Deng, Z., Lo, S. H. & Liu, G. Nanostructures of designed geometry and functionality enable regulation of cellular signaling processes. *Biochemistry* **51,** 5876–93 (2012).
27. Nguyen, A. T., Sathe, S. R. & Yim, E. K. F. From nano to micro : topographical scale and its impact on cell adhesion , morphology and contact guidance. *J. Phys. Condens. Matter* **28,** 1–16 (2016).
28. Wyckoff, J. *et al.* A Paracrine Loop between Tumor Cells and Macrophages Is Required for Tumor Cell Migration in Mammary Tumors A Paracrine Loop between Tumor Cells and Macrophages Is Required for Tumor Cell Migration in Mammary Tumors. *Cancer Res.* **64,** 7022–7029 (2004).
29. Wyckoff, J. B. *et al.* Direct visualization of macrophage-assisted tumor cell intravasation in mammary tumors. *Cancer Res.* **67,** 2649–56 (2007).

30. Bravo-Cordero, J. J., Hodgson, L. & Condeelis, J. Directed cell invasion and migration during metastasis. *Curr. Opin. Cell Biol.* **24,** 277–283 (2012).
31. Lee, G. Y. H. & Lim, C. T. Biomechanics approaches to studying human diseases. *Trends Biotechnol.* **25,** 111–118 (2007).
32. Paszek, M. J. *et al.* Tensional homeostasis and the malignant phenotype. *Cancer Cell* **8,** 241–54 (2005).
33. Paszek, M. J. & Weaver, V. M. The tension mounts: Mechanics meets morphogenesis and malignancy. *J. Mammary Gland Biol. Neoplasia* **9,** 325–342 (2004).
34. Tung, J. C. *et al.* Tumor mechanics and metabolic dysfunction. *Free Radic. Biol. Med.* **79,** 269–280 (2015).
35. Provenzano, P. P. *et al.* Collagen reorganization at the tumor-stromal interface facilitates local invasion. *BMC Med.* **4,** 38 (2006).
36. Provenzano, P. P. *et al.* Collagen density promotes mammary tumor initiation and progression. *BMC Med.* **6,** 11 (2008).
37. Weaver, A. M. Invadopodia: specialized cell structures for cancer invasion. *Clin. Exp. Metastasis* **23,** 97–105 (2006).
38. Parekh, A. *et al.* Sensing and modulation of invadopodia across a wide range of rigidities. *Biophys. J.* **100,** 573–82 (2011).
39. Beaty, B. T. & Condeelis, J. Digging a little deeper: the stages of invadopodium formation and maturation. *Eur. J. Cell Biol.* **93,** 438–44 (2014).
40. Alexander, N. R. *et al.* Extracellular matrix rigidity promotes invadopodia activity. *Curr. Biol.* **18,** 1295–9 (2008).
41. Artym, V. V., Zhang, Y., Seillier-Moiseiwitsch, F., Yamada, K. M. & Mueller, S. C. Dynamic interactions of cortactin and membrane type 1 matrix metalloproteinase at invadopodia: Defining the stages of invadopodia formation and function. *Cancer Res.* **66,** 3034–3043 (2006).
42. Haage, A. & Schneider, I. C. Cellular contractility and extracellular matrix stiffness regulate matrix metalloproteinase activity in pancreatic cancer cells. *FASEB J.* **28,** 3589–99 (2014).
43. Beaty, B. T. *et al.* β1 integrin regulates Arg to promote invadopodial maturation and matrix degradation. *Mol. Biol. Cell* **24,** 1661–75, S1-11 (2013).
44. Brooks, P. C. *et al.* Localization of matrix metalloproteinase MMP-2 to the surface of invasive cells by interaction with integrin ??v??3. *Cell* **85,** 683–693 (1996).
45. White, D. E. & Muller, W. J. Multifaceted roles of integrins in breast cancer metastasis. *J. Mammary Gland Biol. Neoplasia* **12,** 135–142 (2007).
46. Morini, M. *et al.* The ??3??1 integrin is associated with mammary carcinoma cell metastasis, invasion, and gelatinase B (MMP-9) activity. *Int. J. Cancer* **87,** 336–342

(2000).
47. Branch, K. M., Hoshino, D. & Weaver, A. M. Adhesion rings surround invadopodia and promote maturation. *Biol. Open* **1,** 711–722 (2012).
48. Artym, V. V *et al.* Dense fibrillar collagen is a potent inducer of invadopodia via a specific signaling network. *J. Cell Biol.* **208,** 331–50 (2015).
49. Vander Heiden, M. G., Cantley, L. C. & Thompson, C. B. Understanding the Warburg effect: the metabolic requirements of cell proliferation. *Science* **324,** 1029–33 (2009).
50. Van Horssen, R. *et al.* Cancer cell metabolism regulates extracellular matrix degradation by invadopodia. *Eur. J. Cell Biol.* **92,** 113–121 (2013).
51. Warburg, O., Wind, F. & Negelein, E. THE METABOLISM OF TUMORS IN THE BODY. *J. Gen. Physiol.* **8,** 519–30 (1927).
52. Liberti, M. V. & Locasale, J. W. The Warburg Effect: How Does it Benefit Cancer Cells? *Trends Biochem. Sci.* **41,** 211–218 (2016).
53. Scott, K. E. N. *et al.* Metabolic regulation of invadopodia and invasion by acetyl-CoA carboxylase 1 and de novo lipogenesis. *PLoS One* **7,** e29761 (2012).
54. Cunniff, A. B., Mckenzie, A. J., Heintz, N. H. & Alan, K. AMPK activity regulates trafficking of mitochondria to the leading edge during cell migration and matrix invasion Department of Pathology Department of Pharmacology University of Vermont Cancer Center University of Vermont , Burlington , VT 05405 , USA Co. *Mol. Biol. Cell* **27,** 2662–2674 (2016).
55. Arismendi-Morillo, G., Hoa, N. T., Ge, L. & Jadus, M. R. Mitochondrial network in glioma's invadopodia displays an activated state both in situ and in vitro: potential functional implications. *Ultrastruct. Pathol.* **36,** 409–14 (2012).
56. Desai, S. P., Bhatia, S. N., Toner, M. & Irimia, D. Mitochondrial localization and the persistent migration of epithelial cancer cells. *Biophys. J.* **104,** 2077–2088 (2013).
57. Sheng, Z.-H. & Cai, Q. Mitochondrial transport in neurons: impact on synaptic homeostasis and neurodegeneration. *Nat. Rev. Neurosci.* **13,** 77–93 (2012).
58. Saxton, W. M. & Hollenbeck, P. J. The axonal transport of mitochondria. *J. Cell Sci.* **125,** 2095–104 (2012).
59. Lampidis, T. J. *et al.* Mitochondria-Targeted Drugs Synergize with 2-Deoxyglucose to Trigger Breast Cancer Cell Death Gang. *Cancer Res.* **43,** 716–20 (1983).
60. Fendt, S.-M. *et al.* Metformin decreases glucose oxidation and increases the dependency of prostate cancer cells on reductive glutamine metabolism. *Cancer Res.* **73,** 4429–38 (2013).
61. Liu, B. *et al.* Metformin induces unique biological and molecular responses in triple negative breast cancer cells. *Cell Cycle* **8,** 2031–2040 (2009).

62. Hillesheim, L. N. & Müller, J. D. The photon counting histogram in fluorescence fluctuation spectroscopy with non-ideal photodetectors. *Biophys. J.* **85,** 1948–1958 (2003).
63. Müller, J. D., Chen, Y. & Gratton, E. Resolving heterogeneity on the single molecular level with the photon-counting histogram. *Biophys. J.* **78,** 474–486 (2000).
64. Wiseman, P. W. *et al.* Spatial mapping of integrin interactions and dynamics during cell migration by image correlation microscopy. *J. Cell Sci.* **117,** 5521–34 (2004).
65. Chen, Y., Müller, J. D., Ruan, Q. & Gratton, E. Molecular brightness characterization of EGFP in vivo by fluorescence fluctuation spectroscopy. *Biophys. J.* **82,** 133–44 (2002).
66. Meyer, B. H. *et al.* FRET imaging reveals that functional neurokinin-1 receptors are monomeric and reside in membrane microdomains of live cells. *Proc. Natl. Acad. Sci. U. S. A.* **103,** 2138–43 (2006).
67. Ballestrem, C. & Geiger, B. Application of microscope-based FRET to study molecular interactions in focal adhesions of live cells. *Methods Mol. Biol.* **294,** 321–34 (2005).
68. Digman, M. A., Dalal, R., Horwitz, A. F. & Gratton, E. Mapping the number of molecules and brightness in the laser scanning microscope. *Biophys. J.* **94,** 2320–32 (2008).
69. Digman, M. A. *et al.* Measuring Fast Dynamics in Solutions and Cells with a Laser Scanning Microscope. *Biophys. J.* **89,** 1317–1327 (2005).
70. Digman, M. A., Brown, C. M., Horwitz, A. R., Mantulin, W. W. & Gratton, E. Paxillin dynamics measured during adhesion assembly and disassembly by correlation spectroscopy. *Biophys. J.* **94,** 2819–31 (2008).
71. Petit, V. & Thiery, J. P. Focal adhesions: structure and dynamics. *Biol. Cell* **92,** 477–94 (2000).
72. Kulangara, K., Yang, Y., Yang, J. & Leong, K. W. Nanotopography as modulator of human mesenchymal stem cell function. *Biomaterials* **33,** 4998–5003 (2012).
73. Ruoslahti, E. RGD and other recognition sequences for integrins. *Annu. Rev. Cell Dev. Biol.* **12,** 697–715 (1996).
74. Chen, C. S., Mrksich, M., Huang, S., Whitesides, G. M. & Ingber, D. E. Geometric Control of Cell Life and Death. *Science (80-.).* **276,** 1425–1428 (1997).
75. Alom Ruiz, S. & Chen, C. S. Microcontact printing: A tool to pattern. *Soft Matter* **3,** 168 (2007).
76. von Philipsborn, A. C. *et al.* Microcontact printing of axon guidance molecules for generation of graded patterns. *Nat. Protoc.* **1,** 1322–1328 (2006).

77. Chien, F.-C., Kuo, C. W., Yang, Z.-H., Chueh, D.-Y. & Chen, P. Exploring the formation of focal adhesions on patterned surfaces using super-resolution imaging. *Small* **7,** 2906–13 (2011).
78. Sriraghavan, V., Desai, R. a., Kwon, Y., Mrksich, M. & Chen, C. S. Micropatterned dynamically adhesive substrates for cell migration. *Langmuir* **26,** 17733–17738 (2010).
79. Kong, Y. P., Tu, C. H., Donovan, P. J. & Yee, A. F. Expression of Oct4 in human embryonic stem cells is dependent on nanotopographical configuration. *Acta Biomater.* **9,** 6369–80 (2013).
80. Dickson, M. N., Liang, E. I., Rodriguez, L. a., Vollereaux, N. & Yee, A. F. Nanopatterned polymer surfaces with bactericidal properties. *Biointerphases* **10,** 021010 (2015).
81. Ferrari, A., Cecchini, M., Degl Innocenti, R. & Beltram, F. Directional PC12 cell migration along plastic nanotracks. *IEEE Trans. Biomed. Eng.* **56,** 2692–2696 (2009).
82. Zhang, G., Zhang, J., Xie, G., Liu, Z. & Shao, H. Cicada wings: A stamp from nature for nanoimprint lithography. *Small* **2,** 1440–1443 (2006).
83. Teixeira, A. I., Abrams, G. a, Bertics, P. J., Murphy, C. J. & Nealey, P. F. Epithelial contact guidance on well-defined micro- and nanostructured substrates. *J. Cell Sci.* **116,** 1881–92 (2003).
84. Shi, L., Li, J.-R., Shih, Y.-P., Lo, S. H. & Liu, G. Nanogratings of fibronectin provide an effective biochemical cue for regulating focal adhesion and cellular structure. *Nano Res.* **5,** 565–575 (2012).
85. Yim, E. K. F., Pang, S. W. & Leong, K. W. Synthetic nanostructures inducing differentiation of human mesenchymal stem cells into neuronal lineage. *Exp. Cell Res.* **313,** 1820–1829 (2007).
86. Kulangara, K. & Leong, K. W. Substrate topography shapes cell function. *Soft Matter* **5,** 4072 (2009).
87. Yim, E. K. F., Darling, E. M., Kulangara, K., Guilak, F. & Leong, K. W. Nanotopography-induced changes in focal adhesions, cytoskeletal organization, and mechanical properties of human mesenchymal stem cells. *Biomaterials* **31,** 1299–306 (2010).
88. Coyer, S. R. *et al.* Nanopatterning reveals an ECM area threshold for focal adhesion assembly and force transmission that is regulated by integrin activation and cytoskeleton tension. *J. Cell Sci.* **125,** 5110–23 (2012).
89. Berland, K. M., So, P. T. & Gratton, E. Two-photon fluorescence correlation spectroscopy: method and application to the intracellular environment. *Biophys. J.* **68,** 694–701 (1995).
90. Tang, Q. Y. *et al.* Control of cell migration direction by inducing cell shape

asymmetry with patterned topography. *J. Biomed. Mater. Res. Part A* **103A,** 2383–2393 (2014).
91. Huang, J. *et al.* Impact of order and disorder in RGD nanopatterns on cell adhesion. *Nano Lett.* **9,** 1111–1116 (2009).
92. Coussen, F., Choquet, D., Sheetz, M. P. & Erickson, H. P. Trimers of the fibronectin cell adhesion domain localize to actin filament bundles and undergo rearward translocation. *J. Cell Sci.* **115,** 2581–2590 (2002).
93. Digman, M. A., Wiseman, P. W., Choi, C., Horwitz, A. R. & Gratton, E. Stoichiometry of molecular complexes at adhesions in living cells. *Proc. Natl. Acad. Sci. U. S. A.* **106,** 2170–5 (2009).
94. Digman, M. A., Wiseman, P. W., Horwitz, A. R. & Gratton, E. Detecting Protein Complexes in Living Cells from Laser Scanning Confocal Image Sequences by the Cross Correlation Raster Image Spectroscopy Method. *Biophys. J.* **96,** 707–716 (2009).
95. Digman, M. A. & Gratton, E. Analysis of diffusion and binding in cells using the RICS approach. *Microsc. Res. Tech.* **72,** 323–332 (2009).
96. Bate, N. *et al.* Talin contains a C-terminal calpain2 cleavage site important in focal adhesion dynamics. *PLoS One* **7,** (2012).
97. Schindelin, J. *et al.* Fiji: an open-source platform for biological-image analysis. *Nat. Methods* **9,** 676–682 (2012).
98. Kadler, K. E., Holmes, D. F., Trotter, J. A. & Chapman, J. A. Collagen fibril formation. *Biochem. J.* **316 (Pt 1),** 1–11 (1996).
99. Fratzl, P. in *Collagen* 1–13 (Springer US, 2008). doi:10.1007/978-0-387-73906-9_1
100. Digman, M. A., Caiolfa, V. R., Zamai, M. & Gratton, E. The phasor approach to fluorescence lifetime imaging analysis. *Biophys. J.* **94,** L14-6 (2008).
101. Ma, N., Digman, M. A., Malacrida, L. & Gratton, E. Measurements of absolute concentrations of NADH in cells using the phasor FLIM method. *Biomed. Opt. Express* **7,** 2441–52 (2016).
102. Datta, R., Alfonso-García, A., Cinco, R. & Gratton, E. Fluorescence lifetime imaging of endogenous biomarker of oxidative stress. *Sci. Rep.* **5,** 9848 (2015).
103. Wright, B. K. *et al.* Phasor-FLIM analysis of NADH distribution and localization in the nucleus of live progenitor myoblast cells. *Microsc. Res. Tech.* **75,** 1717–22 (2012).
104. Stringari, C. *et al.* Metabolic trajectory of cellular differentiation in small intestine by Phasor Fluorescence Lifetime Microscopy of NADH. *Sci. Rep.* **2,** (2012).
105. Sameni, S., Syed, A., Marsh, J. L. & Digman, M. A. The phasor-FLIM fingerprints reveal shifts from OXPHOS to enhanced glycolysis in Huntington Disease. *Sci. Rep.* **6,** 34755 (2016).

106. Lakowicz, J. R., Szmacinski, H., Nowaczyk, K. & Johnson, M. L. Fluorescence lifetime imaging of free and protein-bound NADH. *Proc. Natl. Acad. Sci. U. S. A.* **89,** 1271–5 (1992).
107. Caino, M. C. *et al.* PI3K therapy reprograms mitochondrial trafficking to fuel tumor cell invasion. *Proc. Natl. Acad. Sci. U. S. A.* **112,** 8638–8643 (2015).
108. Zhao, J. *et al.* Mitochondrial dynamics regulates migration and invasion of breast cancer cells. *Oncogene* **32,** 4814–24 (2013).
109. Estrella, V. *et al.* Acidity generated by the tumor microenvironment drives local invasion. *Cancer Res.* **73,** 1524–35 (2013).
110. Seewaldt, V. ECM stiffness paves the way for tumor cells. *Nat. Med.* **20,** 332–333 (2014).
111. Wells, R. G. The role of matrix stiffness in regulating cell behavior. *Hepatology* **47,** 1394–1400 (2008).
112. Bugyi, B. & Carlier, M.-F. Control of actin filament treadmilling in cell motility. *Annu. Rev. Biophys.* **39,** 449–70 (2010).
113. Ponti, A., Machacek, M., Gupton, S. L., Waterman-Storer, C. M. & Danuser, G. Two distinct actin networks drive the protrusion of migrating cells. *Science* **305,** 1782–6 (2004).
114. Yang, L. *et al.* Twist promotes reprogramming of glucose metabolism in breast cancer cells through PI3K/AKT and p53 signaling pathways. *Oncotarget* **6,** 25755–25769 (2015).
115. Ata, R. & Antonescu, C. N. Integrins and Cell Metabolism: An Intimate Relationship Impacting Cancer. *Int. J. Mol. Sci.* **18,** (2017).
116. Levental, K. R. *et al.* Matrix crosslinking forces tumor progression by enhancing integrin signaling. *Cell* **139,** 891–906 (2009).
117. Provenzano, P. P., Eliceiri, K. W. & Keely, P. J. Multiphoton microscopy and fluorescence lifetime imaging microscopy (FLIM) to monitor metastasis and the tumor microenvironment. *Clin. Exp. Metastasis* **26,** 357–70 (2009).
118. Bird, D. K. *et al.* Metabolic mapping of MCF10A human breast cells via multiphoton fluorescence lifetime imaging of the coenzyme NADH. *Cancer Res.* **65,** 8766–73 (2005).
119. Cinco, R., Digman, M. A., Gratton, E. & Luderer, U. Spatial Characterization of Bioenergetics and Metabolism of Primordial to Preovulatory Follicles in Whole Ex Vivo Murine Ovary. *Biol. Reprod.* **95,** 129–129 (2016).
120. Stringari, C., Nourse, J. L., Flanagan, L. A. & Gratton, E. Phasor Fluorescence Lifetime Microscopy of Free and Protein-Bound NADH Reveals Neural Stem Cell Differentiation Potential. *PLoS One* **7,** e48014 (2012).
121. Raub, C. B. *et al.* Image correlation spectroscopy of multiphoton images correlates

with collagen mechanical properties. *Biophys. J.* **94,** 2361–73 (2008).
122. Tilghman, R. W. *et al.* Matrix Rigidity Regulates Cancer Cell Growth by Modulating Cellular Metabolism and Protein Synthesis. *PLoS One* **7,** e37231 (2012).
123. Chiu, C.-L., Digman, M. A. & Gratton, E. Cell matrix remodeling ability shown by image spatial correlation. *J. Biophys.* **2013,** 532030 (2013).
124. Skala, M. C. *et al.* In vivo multiphoton fluorescence lifetime imaging of protein-bound and free nicotinamide adenine dinucleotide in normal and precancerous epithelia. *J. Biomed. Opt.* **12,** 024014 (2007).
125. Jameson, D. M., Thomas, V. & Zhou, D. M. Time-resolved fluorescence studies on NADH bound to mitochondrial malate dehydrogenase. *Biochim. Biophys. Acta* **994,** 187–90 (1989).
126. Morris, B. A. *et al.* Collagen Matrix Density Drives the Metabolic Shift in Breast Cancer Cells. *EBioMedicine* **13,** 146–156 (2016).
127. Caino, M. C. *et al.* PI3K therapy reprograms mitochondrial trafficking to fuel tumor cell invasion. *Proc. Natl. Acad. Sci. U. S. A.* **112,** 8638–43 (2015).
128. Ward, P. S. & Thompson, C. B. Metabolic reprogramming: a cancer hallmark even warburg did not anticipate. *Cancer Cell* **21,** 297–308 (2012).
129. Gould, C. M. & Courtneidge, S. a. Regulation of invadopodia by the tumor microenvironment. *Cell Adh. Migr.* **8,** 1–10 (2014).
130. Ciobanasu, C., Faivre, B. & Le Clainche, C. Integrating actin dynamics, mechanotransduction and integrin activation: the multiple functions of actin binding proteins in focal adhesions. *Eur. J. Cell Biol.* **92,** 339–48 (2013).
131. Lien, E. C., Lyssiotis, C. A. & Cantley, L. C. in *Recent results in cancer research. Fortschritte der Krebsforschung. Progres dans les recherches sur le cancer* **207,** 39–72 (Springer, Cham, 2016).
132. Bays, J. L., Campbell, H. K., Heidema, C., Sebbagh, M. & DeMali, K. A. Linking E-cadherin mechanotransduction to cell metabolism through force-mediated activation of AMPK. *Nat. Cell Biol.* **19,** 724–731 (2017).
133. Hayashi, T., Hirshman, M. F., Kurth, E. J., Winder, W. W. & Goodyear, L. J. Evidence for 5[prime] AMP-activated protein kinase mediation of the effect of muscle contraction on glucose transport. *Diabetes* **47,** 1369–1373 (1998).
134. Martin, K. *et al.* Spatio-temporal co-ordination of RhoA, Rac1 and Cdc42 activation during prototypical edge protrusion and retraction dynamics. *Sci. Rep.* **6,** 21901 (2016).
135. Palorini, R., Simonetto, T., Cirulli, C. & Chiaradonna, F. Mitochondrial complex I inhibitors and forced oxidative phosphorylation synergize in inducing cancer cell death. *Int. J. Cell Biol.* **2013,** 243876 (2013).

136. Cavalcanti-Adam, E. A. *et al.* Cell spreading and focal adhesion dynamics are regulated by spacing of integrin ligands. *Biophys. J.* **92,** 2964–74 (2007).
137. Massia, S. P. & Hubbell, J. a. Human endothelial cell interactions with surface-coupled adhesion peptides on a nonadhesive glass substrate and two polymeric biomaterials. *J. Biomed. Mater. Res.* **25,** 223–242 (1991).
138. Calderwood, D. a, Campbell, I. D. & Critchley, D. R. Talins and kindlins: partners in integrin-mediated adhesion. *Nat. Rev. Mol. Cell Biol.* **14,** 503–17 (2013).
139. Ochsner, M., Textor, M., Vogel, V. & Smith, M. L. Dimensionality Controls Cytoskeleton Assembly and Metabolism of Fibroblast Cells in Response to Rigidity and Shape. *PLoS One* **5,** e9445 (2010).
140. DeBerardinis, R. J., Lum, J. J., Hatzivassiliou, G. & Thompson, C. B. The Biology of Cancer: Metabolic Reprogramming Fuels Cell Growth and Proliferation. *Cell Metab.* **7,** 11–20 (2008).
141. Aguilar-Arnal, L. *et al.* Spatial dynamics of SIRT1 and the subnuclear distribution of NADH species. *Proc. Natl. Acad. Sci. U. S. A.* **113,** 12715–12720 (2016).
142. Raub, C. B. *et al.* Noninvasive assessment of collagen gel microstructure and mechanics using multiphoton microscopy. *Biophys. J.* **92,** 2212–22 (2007).
143. Berezin, M. Y. & Achilefu, S. Fluorescence lifetime measurements and biological imaging. *Chem. Rev.* **110,** 2641–84 (2010).
144. Hinde, E., Digman, M. a, Welch, C., Hahn, K. M. & Gratton, E. Biosensor Förster resonance energy transfer detection by the phasor approach to fluorescence lifetime imaging microscopy. *Microsc. Res. Tech.* **75,** 271–81 (2012).
145. van Horssen, R. *et al.* Modulation of cell motility by spatial repositioning of enzymatic ATP/ADP exchange capacity. *J. Biol. Chem.* **284,** 1620–7 (2009).
146. Dalby, M. J., Gadegaard, N. & Oreffo, R. O. C. Harnessing nanotopography and integrin-matrix interactions to influence stem cell fate. *Nat. Mater.* **13,** 558–69 (2014).
147. Lo, C. M., Wang, H. B., Dembo, M. & Wang, Y. L. Cell movement is guided by the rigidity of the substrate. *Biophys. J.* **79,** 144–52 (2000).
148. Chen, C. S., Alonso, J. L., Ostuni, E., Whitesides, G. M. & Ingber, D. E. Cell shape provides global control of focal adhesion assembly. *Biochem. Biophys. Res. Commun.* **307,** 355–361 (2003).
149. Chiu, C.-L. & Gratton, E. Axial super resolution topography of focal adhesion by confocal microscopy. *Microsc. Res. Tech.* **76,** 1070–8 (2013).
150. Huveneers, S. & Danen, E. H. J. Adhesion signaling - crosstalk between integrins, Src and Rho. *J. Cell Sci.* **122,** 1059–1069 (2009).
151. Murphy, D. A. & Courtneidge, S. A. The 'ins' and 'outs' of podosomes and invadopodia: characteristics, formation and function. *Nat. Rev. Mol. Cell Biol.* **12,**

413–426 (2011).
152. Weaver, A. M. Invadopodia: Specialized cell structures for cancer invasion. *Clin. Exp. Metastasis* **23,** 97–105 (2006).
153. Oser, M. *et al.* Cortactin regulates cofilin and N-WASp activities to control the stages of invadopodium assembly and maturation. *J. Cell Biol.* **186,** 571–87 (2009).
154. Yin, M. *et al.* Cortactin in cancer cell migration and invasion. *Oncotarget* **8,** 88232–88243 (2017).
155. Schoumacher, M., Goldman, R. D., Louvard, D. & Vignjevic, D. M. Actin, microtubules, and vimentin intermediate filaments cooperate for elongation of invadopodia. *J. Cell Biol.* **189,** 541–556 (2010).
156. Condeelis, J. & Pollard, J. W. Macrophages: obligate partners for tumor cell migration, invasion, and metastasis. *Cell* **124,** 263–6 (2006).
157. Zanotelli, M. R. *et al.* Regulation of ATP utilization during metastatic cell migration by collagen architecture. *Mol. Biol. Cell* **29,** 1–9 (2018).
158. Grashoff, C. *et al.* Measuring mechanical tension across vinculin reveals regulation of focal adhesion dynamics. *Nature* **466,** 263–266 (2010).
159. Sun, Z., Guo, S. S. & Fässler, R. Integrin-mediated mechanotransduction. *J. Cell Biol.* **215,** 445–456 (2016).
160. Boettiger, D. Mechanical control of integrin-mediated adhesion and signaling. *Curr. Opin. Cell Biol.* **24,** 592–9 (2012).
161. Weitzman, M. & Hahn, K. M. Optogenetic approaches to cell migration and beyond. *Curr. Opin. Cell Biol.* **30,** 112–20 (2014).
162. Wu, Y. I. *et al.* A genetically encoded photoactivatable Rac controls the motility of living cells. *Nature* **461,** 104–8 (2009).
163. Ridley, A. J. *et al.* Cell migration: integrating signals from front to back. *Science* **302,** 1704–9 (2003).
164. Faix, J. & Weber, I. A dual role model for active Rac1 in cell migration. *Small GTPases* **4,** 110–115 (2013).
165. Price, L. S., Leng, J., Schwartz, M. A. & Bokoch, G. M. Activation of Rac and Cdc42 by integrins mediates cell spreading. *Mol. Biol. Cell* **9,** 1863–71 (1998).
166. Burkel, B. *et al.* Preparation of 3D Collagen Gels and Microchannels for the Study of 3D Interactions In Vivo. *J. Vis. Exp.* (2016). doi:10.3791/53989
167. Pollard, J. W. Macrophages define the invasive microenvironment in breast cancer. *J. Leukoc. Biol.* **84,** 623–30 (2008).
168. Braber, E. T. Den, Ruijter, J. E. De, Ginsel, L. A., Recum, A. F. Von & Jansen, J. A. Orientation of ECM protein deposition , fibroblast cytoskeleton , and attachment complex components on silicone microgrooved surfaces. *J Biomed Mater Res.* (1997).

169. Chung, C. Y., Lee, S., Briscoe, C., Ellsworth, C. & Firtel, R. A. Role of Rac in controlling the actin cytoskeleton and chemotaxis in motile cells. *Proc. Natl. Acad. Sci. U. S. A.* **97,** 5225–30 (2000).
170. Albiges-Rizo, C., Destaing, O., Fourcade, B., Planus, E. & Block, M. R. Actin machinery and mechanosensitivity in invadopodia, podosomes and focal adhesions. *J. Cell Sci.* **122,** 3037–3049 (2009).
171. Yamaguchi, H. *et al.* Molecular mechanisms of invadopodium formation: the role of the N-WASP-Arp2/3 complex pathway and cofilin. *J. Cell Biol.* **168,** 441–52 (2005).
172. Frey, M. T., Tsai, I. Y., Russell, T. P., Hanks, S. K. & Wang, Y.-L. Cellular responses to substrate topography: role of myosin II and focal adhesion kinase. *Biophys. J.* **90,** 3774–82 (2006).
173. Gupta, M. *et al.* Adaptive rheology and ordering of cell cytoskeleton govern matrix rigidity sensing. *Nat. Commun.* **6,** 7525 (2015).
174. Kovar, D. R., Harris, E. S., Mahaffy, R., Higgs, H. N. & Pollard, T. D. Control of the assembly of ATP- and ADP-actin by formins and profilin. *Cell* **124,** 423–35 (2006).
175. Pollard, T. D. Rate constants for the reactions of ATP- and ADP-actin with the ends of actin filaments. *J. Cell Biol.* **103,** 2747–2754 (1986).
176. Kuhn, J. R. & Pollard, T. D. Real-time measurements of actin filament polymerization by total internal reflection fluorescence microscopy. *Biophys. J.* **88,** 1387–402 (2005).
177. Partikian, A., Ölveczky, B., Swaminathan, R., Li, Y. & Verkman, A. S. Rapid Diffusion of Green Fluorescent Protein in the Mitochondrial Matrix. *J. Cell Biol.* **140,** 821–829 (1998).
178. Gorelik, R. & Gautreau, A. Quantitative and unbiased analysis of directional persistence in cell migration. *Nat. Protoc.* **9,** 1931–1943 (2014).
179. Plant, A. L., Bhadriraju, K., Spurlin, T. A. & Elliott, J. T. Cell response to matrix mechanics: Focus on collagen. *Biochim. Biophys. Acta - Mol. Cell Res.* **1793,** 893–902 (2009).
180. Digman, M. A., Brown, C. M., Horwitz, A. R., Mantulin, W. W. & Gratton, E. Paxillin dynamics measured during adhesion assembly and disassembly by correlation spectroscopy. *Biophys. J.* **94,** 2819–31 (2008).
181. Teri W. Odom, J. Christopher Love, Daniel B. Wolfe, Kateri E. Paul, and & Whitesides*, G. M. Improved Pattern Transfer in Soft Lithography Using Composite Stamps. (2002). doi:10.1021/LA020169L
182. Rossow, M. J., Sasaki, J. M., Digman, M. A. & Gratton, E. Raster image correlation spectroscopy in live cells. *Nat. Protoc.* **5,** 1761–1774 (2010).